

# **Short-Wavelength Reactor Neutrino Oscillations**

---

A Dissertation  
Submitted to  
the Temple University Graduate Board

---

In Partial Fulfillment  
of the Requirements for the Degree  
**DOCTOR OF PHILOSOPHY**

---

by  
Danielle E. Landschoot  
December 2019

## Examining Committee Members:

Jim Napolitano, Department of Physics, Advisory Chair  
Maria Iavarone, Department of Physics  
C. Jeff Martoff, Department of Physics  
Don Jones, Department of Physics  
Michelle Dolinski, External Reader, Department of Physics, Drexel University

# ABSTRACT

The Precision Reactor Oscillation and SPECTrum Experiment (PROSPECT) is designed to probe short baseline oscillations of electron antineutrinos in search of eV-scale sterile neutrinos and precisely measure the  $^{235}\text{U}$  reactor antineutrino spectrum from the High Flux Isotope Reactor (HFIR) at Oak Ridge National Laboratory. The PROSPECT antineutrino detector (AD) provides excellent background rejection and position resolution due to its segmented design and use of  $^6\text{Li}$ -loaded liquid scintillator. In order to understand relative volume variation effects, which could affect an oscillation measurement,  $^{227}\text{Ac}$  was added as a calibration source that was dissolved isotropically throughout the liquid scintillator. Using the correlated production of alphas from  $^{219}\text{Rn} \rightarrow ^{215}\text{Po} \rightarrow ^{211}\text{Pb}$  in the  $^{227}\text{Ac}$  decay chain I measured the rate of  $^{227}\text{Ac}$  in each segment of the detector as well as the decay rate of  $^{227}\text{Ac}$  events over the lifetime of the detector. The measured  $^{227}\text{Ac}$  half-life suggests a rate of events falling  $1.56 \pm 0.21\%$  faster than expectation. The results of these studies were then applied as corrections to the measurement of antineutrino event rates as a function of distance from the reactor. This thesis will present the testing of  $^{227}\text{Ac}$  as a calibration source before its addition to the AD, analysis methods, results of  $^{227}\text{Ac}$  in the AD, and its application to the oscillation analysis.

# **ACKNOWLEDGEMENTS**

These are the acknowledgements, where you express your appreciation to those who were influential and important to your success.

# TABLE OF CONTENTS

<b>ABSTRACT</b>	i
<b>ACKNOWLEDGEMENTS</b>	ii
<b>LIST OF FIGURES</b>	xiii
<b>LIST OF TABLES</b>	xv
CHAPTER	
<b>1 NEUTRINOS</b>	1
1.1 Discovery of the Neutrino . . . . .	1
1.2 Neutrinos in the Standard Model and Beyond . . . . .	3
1.3 Discovery of Neutrino Oscillation . . . . .	6
<b>2 REACTOR NEUTRINOS</b>	11
2.1 Production of Reactor Neutrinos . . . . .	11
2.2 Measuring the Reactor Antineutrino Flux and Spectrum . . . . .	12
2.3 Detection of Reactor Neutrinos . . . . .	15
2.4 The Reactor Antineutrino Anomaly . . . . .	16
<b>3 THE PROSPECT EXPERIMENT</b>	21
3.1 Experimental Site . . . . .	21
3.1.1 HFIR . . . . .	21
3.1.2 Backgrounds at HFIR . . . . .	22
3.2 Design . . . . .	23
3.2.1 Active Detector . . . . .	24

3.2.1.1	PMT Housings . . . . .	24
3.2.1.2	Optical Grid . . . . .	25
3.2.1.3	Segment Supports . . . . .	27
3.2.1.4	Radioactive Calibration System . . . . .	27
3.2.1.5	Liquid Scintillator . . . . .	28
3.2.2	Containment Vessels and Shielding . . . . .	30
3.3	Data Acquisition System . . . . .	31
<b>4</b>	<b>PROSPECT ANALYSIS FRAMEWORK AND CALIBRATION</b>	<b>33</b>
4.1	Pulse Shape Discrimination . . . . .	33
4.2	Data Processing and Calibration . . . . .	34
4.2.1	Timing to Position Curves . . . . .	35
4.2.2	Energy Calibration . . . . .	37
4.3	Monte Carlo Simulation . . . . .	38
4.3.1	Nonlinearity . . . . .	38
4.3.2	Energy Response . . . . .	39
4.3.3	Energy Resolution . . . . .	39
<b>5</b>	<b><math>^{227}\text{AC}</math> AS A CALIBRATION SOURCE</b>	<b>43</b>
5.1	Motivation . . . . .	43
5.2	Material Compatibility . . . . .	45
5.2.1	Material and Scintillator Preparation . . . . .	45
5.2.2	Detector . . . . .	47
5.2.3	Data Analysis . . . . .	48
5.2.4	Results . . . . .	50
5.2.4.1	Viton . . . . .	54
5.3	$^{227}\text{Ac}$ in the PROSPECT AD . . . . .	56
5.3.1	Spiking the LiLS . . . . .	56
5.3.2	Data Set . . . . .	59
5.3.3	Event Selection . . . . .	60
5.3.4	Rate Calculation . . . . .	62
5.3.5	Detector Performance as Tracked with $^{227}\text{Ac}$ . . . . .	66
5.3.6	$^{227}\text{Ac}$ Rate versus Time . . . . .	70
5.3.7	$^{227}\text{Ac}$ Rate in Individual Segments . . . . .	73
5.3.8	Systematic Errors . . . . .	74

5.3.8.1	Energy, PSD, and $\Delta z$ Cuts . . . . .	75
5.3.8.2	Other Coincident Alphas . . . . .	78
5.3.9	$^{227}\text{Ac}$ Rates per Baseline . . . . .	79
<b>6</b>	<b>NEUTRINO OSCILLATION IN THE PROSPECT AD</b>	<b>82</b>
6.1	Detecting Antineutrinos . . . . .	82
6.2	IBD Event Selection . . . . .	83
6.2.1	Cuts . . . . .	83
6.2.2	Backgrounds . . . . .	85
6.2.3	Atmospheric Correction . . . . .	86
6.2.4	Background Subtraction . . . . .	87
6.3	Data Set . . . . .	87
6.4	IBD Rates versus Baseline . . . . .	88
6.5	Oscillation Search . . . . .	90
6.5.1	Uncertainties . . . . .	92
6.5.2	Confidence Interval Assignment . . . . .	95
6.5.3	Results . . . . .	96
6.6	Measured Antineutrino Spectrum . . . . .	98
<b>7</b>	<b>CONCLUSIONS</b>	<b>100</b>
<b>BIBLIOGRAPHY</b>		<b>101</b>
<b>APPENDICES</b>		

# LIST OF FIGURES

1.1	Spectrum of solar neutrino fluxes . . . . .	7
2.1	Fission of $^{235}\text{U}$ . . . . .	12
2.2	The $\bar{\nu}_e$ spectrum. . . . .	13
2.3	The IBD spectrum. . . . .	16
2.4	Daya Bay $\bar{\nu}_e$ flux. . . . .	17
2.5	World average of reactor $\bar{\nu}_e$ flux. . . . .	18
2.7	Spectrums. . . . .	20
3.1	The HFIR core and flux distribution . . . . .	22
3.2	Layout of PROSPECT at HFIR . . . . .	23
3.3	Schematic of the PROSPECT detector . . . . .	24
3.4	Cross-section of inner detector . . . . .	25
3.5	PMT housing module . . . . .	25

3.6	Pinwheels . . . . .	26
3.7	Schematic of a segment . . . . .	26
3.8	Construction of a row . . . . .	26
3.9	Completed inner detector . . . . .	27
3.10	Source tube positions . . . . .	29
3.11	Source capsule on timing belt . . . . .	29
3.12	LiLS UV-Vis absorption spectra . . . . .	30
3.13	DAQ schematic . . . . .	32
4.1	Typical waveform . . . . .	34
4.2	PSD vs. psuedo-energy for neutron coincident events . . . . .	35
4.3	Muon $dt$ versus signal amplitude . . . . .	36
4.4	Muon $dt$ for a single segment . . . . .	36
4.5	$z(dt)$ curves for all cells . . . . .	36
4.6	Energy position dependence . . . . .	37
4.7	MC-data comparison of reconstructed energy . . . . .	41
4.8	MC-data reconstructed energy peak ratio for $\gamma$ sources . . . . .	42
5.1	Monte Carlo neutrino spectrum as a function of L/E . . . . .	43

5.2	$^{227}\text{Ac}$ decay chain . . . . .	44
5.3	Material sample vials . . . . .	47
5.4	Detector used for material adsorption studies . . . . .	47
5.5	Typical RnPo energy and PSD distributions . . . . .	49
5.6	Typical RnPo $\Delta t$ distribution . . . . .	50
5.7	$^{227}\text{Ac}$ rate for each material sample . . . . .	50
5.8	$^{215}\text{Po}$ energy distribution for reference sample with two Gaussian fit .	51
5.9	$^{215}\text{Po}$ mean versus time for the reference sample . . . . .	52
5.10	$^{215}\text{Po}$ $1\sigma$ width versus time for the reference sample . . . . .	52
5.11	$^{227}\text{Ac}$ rate for each material sample relative to the reference sample .	53
5.12	RnPo energy spectra for viton and PEEK at the first and last time bins	55
5.13	The $1\sigma$ width of two Gaussians fit to the $^{219}\text{Rn}$ energy spectrum versus time for the viton o-ring material sample. Black (circle): higher energy Gaussian, Magenta (square): lower energy Gaussian. . . . .	55
5.14	A graphic of the procedure used to spike the drum of LiLS with $^{227}\text{Ac}$ for filling of the AD. . . . .	57
5.15	Measured $^{227}\text{Ac}$ rates of vials used in the procedure performed to add $^{227}\text{Ac}$ to the LiLS of the PROSPECT AD. Top: intermediate vials V1 and V2. Bottom: V3, filled in the same method as the vial that was added to the drum of LiLS. All rates were fit with a constant, the results drawn as solid lines with hashed lines representing the error. .	59

5.16 Graphic of 154 segments of the PROSPECT AD. Grayed out segments are those that ‘turned off’ during the data period and are excluded in this analysis. . . . .	60
5.17 RnPo distributions for all cells integrated over all time. . . . .	61
5.18 Coincidental (black), accidental (magenta), and background subtracted (blue) $\Delta t$ distributions for a typical segment integrated over all time. A fit of Equation 5.9 to the background subtraction distribution is shown in red along with its results. . . . .	62
5.19 The value of $\tau$ obtained from the exponential fit to the $\Delta t$ distribution for each individual segment integrated over all time (a) and for all segments versus time (b). The currently accepted value for $\tau$ , $2.569 \pm 0.007$ ms, is marked by the shaded green area. A constant fit to the data is shown as the dashed red line. . . . .	63
5.20 The dead time, as a fraction of livetime, due to the pileup veto versus time. Shaded areas are reactor on periods. . . . .	64
5.21 Energy (a), PSD (b), and $\Delta z$ (c) distributions for RnPo events in a typical segment integrated over all time. Also shown are the results of fitting each distribution with a Gaussian for the purpose of calculating the cut efficiencies. . . . .	65
5.22 Cut efficiencies calculated for RnPo events in individual segments integrated over all time. . . . .	65
5.23 Cut efficiencies calculated for RnPo events versus time integrated over all segments. Shaded areas are reactor on periods. . . . .	66

5.24 Mean (a) and $1\sigma$ width (b) of the $^{215}\text{Po}$ energy distribution versus time integrated over all segments. Both before applied a correction (E) and after correction (ESmear) are shown. Shaded areas are reactor on periods. . . . .	67
5.25 Mean (a) and $1\sigma$ width (b) of the $^{215}\text{Po}$ PSD distribution versus time integrated over all segments. Shaded areas are reactor on periods. . . . .	68
5.26 $1\sigma$ width of the $\Delta z$ distribution versus time. Shaded areas are reactor on periods. . . . .	69
5.27 Segment-to-segment stability of the $^{215}\text{Po}$ energy (a), energy resolution (b), position reconstruction (c), and position resolution (d). Distributions are shown separately for Hamamatsu and ET segments. . . . .	69
5.28 $^{227}\text{Ac}$ rate as measured versus time integrated over all segments. Fit with two exponentials, one in which the half-life of $^{227}\text{Ac}$ is allowed to vary (red) and one in which it is fixed (black). Errors are statistical. Shaded areas are reactor on periods. . . . .	70
5.29 The PROSPECT detector divided into five sections of two rows each. Segments shaded in red are excluded from this analysis. . . . .	71
5.30 The measured $^{227}\text{Ac}$ rate versus time for each section of two rows, fit with an exponential in which the half-life is allowed to vary. . . . .	72
5.31 The half-life results from fitting the $^{227}\text{Ac}$ rate versus time for five sections of two rows. . . . .	72
5.32 The $^{227}\text{Ac}$ per individual segment integrated over all time. Dashed line represents the average over all segments. Dotted lines are $\pm 1\%$ and $\pm 2\%$ from the average. Blue: Hamamatsu segments, red: ET segments. Errors are statistical. . . . .	73

5.33 The $^{227}\text{Ac}$ per individual segment integrated over all time. Dashed line represents the average over only Hamamatsu segments. Dotted lines are $\pm 1\%$ and $\pm 2\%$ from the average. Blue: Hamamatsu segments, red: ET segments. Errors are statistical. [remove ETs from plot] . . .	74
5.34 Histogram of the individual segment $^{227}\text{Ac}$ rates. Blue (solid): Hamamatsu and ET segments, StdDev = 0.031 mHz. Black (dashed): only Hamamatsu segments, StdDev = 0.026 mHz. . . . .	74
5.35 $^{227}\text{Ac}$ rate per segment for different $\sigma$ -based cuts on the delayed energy.	75
5.36 Pictured here are distributions created by calculating for each cell the difference between the rate using a given $\sigma$ cut and the rate using a $4\sigma$ cut normalized by the rate using a $4\sigma$ cut for data. . . . .	77
5.37 The mean of the distributions shown in Figure 5.36. Solid lines: data. Dashed lines: simulation. Connecting lines are not fits; only meant to help guide the eye of the reader. . . . .	78
5.38 The PROSPECT AD divided into 10 baselines, where baseline 1 is closest to the reactor. Segments in white are either fiducial segments or were turned off. . . . .	80
5.39 The $^{227}\text{Ac}$ rate for fiducial $z$ volume averaged over each of the 10 defined baselines and relative to the first baseline. Error bars are statistical, systematic errors are shown as the shaded region. . . . .	81
6.1 Schematic of the IBD interaction in the PROSPECT AD. . . . .	83
6.2 PSD versus energy distribution for prompt events correlated with a delayed neutron capture on $^6\text{Li}$ . The cuts used for identifying $n\text{Li}$ events is represented by the blue rectangle. The upper limit of the cut used for identifying electron-like signals is shown as the pink curve. . .	84

6.3	The prompt energy spectra, after background subtraction, of IBD events for 24 hours of both reactor on and off data. Prominent peaks at 2.2 MeV and 4.4 MeV are due to neutron captures on Hydrogen and inelastic neutron scatters on $^{12}\text{C}$ respectively. . . . .	85
6.5	Accidentals-subtracted IBD candidate event rate per day (black) and measured accidental rate (red) as a function of time. IBD candidate rates are corrected for dead time and exposure time. The shaded regions (green) are reactor on periods. Errors are statistical. The gap in data corresponds to a detector maintenance period. . . . .	88
6.6	The PROSPECT AD divided into 14 baselines, where baseline 1 is closest to the reactor. Segments in white are either fiducial segments or were turned off. . . . .	89
6.7	Background subtracted IBD event rate as a function of distance from the reactor center binned into 14 unique baselines. Data is fit with $C/r^2$ (dashed, magenta) and produces a $\chi^2/NDF = 10.89/13$ . Errors are statistical. . . . .	89
6.8	The $^{227}\text{Ac}$ rate (for fiducial $z$ ) averaged over each of the 14 defined baselines, plotted relative to the first baseline. Error bars are statistical, systematic errors are shown as the shaded region. . . . .	90
6.9	Background subtracted IBD event rate as a function of distance from the reactor center binned into 14 unique baselines, corrected for the measured $^{227}\text{Ac}$ rates in Figure 6.8. . . . .	91
6.12	The normalized $\bar{\nu}_e$ as predicted by Huber+Vogel-Beacom with and without the aluminum + non-equilibrium corrections (1.3%). . . . .	94

- 6.14 Ratio of the measured IBD prompt energy spectra to the predicted baseline-integrated spectrum, for 6 baseline bins. Error bars include statistical and systematic uncertainties. Also shown are the no-oscillation expectation (gray, dashed) and an oscillated expectation based on the best fit Reactor Antineutrino Anomaly parameters (teal, dashed). [1] 97
- 6.16 Reconstructed visible prompt energy of IBD events (black), along with correlated IBD candidates in reactor on (blue, solid) and reactor off (red, dashed) periods. Errors are statistical. The reactor off spectrum has been scaled by the relative exposure time between on and off. [2] 99

# LIST OF TABLES

1.1	The Standard Model of Particle Physics . . . . .	3
1.2	Neutrino Oscillation Parameters . . . . .	10
3.1	Calibration sources . . . . .	28
5.1	$\alpha$ and $\gamma$ energies of $^{219}\text{Rn}$ and $^{215}\text{Po}$ decays . . . . .	45
5.2	Samples used to test if $^{227}\text{Ac}$ or its daughters would adsorb onto detector materials. . . . .	46
5.3	The weight of $^{227}\text{Ac}$ spiked LiLS that was added to each sample vial.	46
5.4	Energy, PSD, and time cuts used to find RnPo events where $\tau_{\text{Po}} = 2.57$ ms. Energy and PSD cuts are applied to both prompt and delay events.	48
5.5	The results of fitting the relative rate for each material sample with a constant. . . . .	53
5.6	The results of fitting the relative rate for each material with a straight line. . . . .	53
5.7	The weight of all solutions added and removed from the four vials for spiking of the LiLS with $^{227}\text{Ac}$ for filling of the AD. . . . .	58

5.8	Expected and measured $^{227}\text{Ac}$ activity in vials prepared for spiking the LiLS.	58
5.9	Broad cuts used to find RnPo events, where $\tau$ is the lifetime of $^{215}\text{Po}$ , 2.57 ms.	61
5.10	Dominant $\alpha$ energies for coincident $\alpha$ event chains that could contaminate the $^{227}\text{Ac}$ RnPo signal. Also given are the quenched energies (QE) and $1\sigma$ widths based on a 5% energy resolution.	79
5.11	Energy and time cut efficiencies and resulting rates (assuming an $^{227}\text{Ac}$ rate of 240 mHz) for both coincident $\alpha$ event chains that could contribute to contamination of the $^{227}\text{Ac}$ RnPo signal selection.	79
6.1	The total number of correlated and accidental events in the prompt energy region (0.8, 7.2) MeV for reactor on and off periods. Time refers to exposure time.	88
6.2	Summary of systematic uncertainties that were used to generate the covariance matrices used in the oscillation analysis. Uncertainties are correlated unless otherwise noted.	95

# CHAPTER 1

## NEUTRINOS

### 1.1 Discovery of the Neutrino

The study of radioactive decay in the early 20th century exposed discrepancies that would lead to the postulation and eventual discovery of the neutrino. An experiment performed by Lise Meitner and Otto Hahn in 1911 offered some of the first evidence that the energy spectrum of electrons emitted by beta decay is continuous [3]. This was in stark contrast to the expected discrete spectra that had been observed in gamma and alpha emission, and suggested that three laws of conservation (energy, linear momentum, and angular momentum) were broken during beta decay. Their findings were later confirmed by experiments performed by Chadwick in 1914 [4] and Ellis and Wooster in 1927 [5].

At the time, beta decay was thought to be a two-particle decay, a process that yields a product nucleus and an electron. In 1930, Wolfgang Pauli postulated a particle he called the ‘neutron’, which would be ejected with the electron, thereby conserving energy and momentum. Describing his idea as a “desperate remedy”, this new particle would have to be neutral and almost non-interacting, therefore making it almost impossible to detect. In 1934, Enrico Fermi further developed the theory of beta decay, including Pauli’s particle but renaming it the neutrino, meaning “little neutral one” [6]. Due to the nature of the weakly interacting neutrino, experimental discovery would take another 20 years.

In 1956 Clyde Cowan and Frederick Reines discovered this elusive particle experimentally by taking advantage of the inverse beta decay (IBD) process [7]:

$$\bar{\nu} + p \rightarrow n + e^+ \quad (1.1)$$

Their idea was to place a detector near an intense source of neutrinos, fill it with an ample number of protons, and observe the resulting positrons. However, any source that generates a large enough flux of neutrinos will create large backgrounds for the experiment. As would become the challenge for every neutrino detector thereafter, Cowan and Reines had to devise a way to reliably remove the background. Their original idea was to place a detector underground about 40 meters away from a fission bomb. This would create a large instantaneous flux of neutrinos providing a sufficient signal to background ratio.

After some thought, though, they realized that by detecting both the neutron *and* the positron they could discriminate the IBD signal from the background with much higher success. This would allow the use of a nuclear reactor instead of a fission bomb as a neutrino source, giving them the opportunity to patiently watch for neutrinos rather than be restricted to one chance with a bomb. The final detector that would facilitate the discovery of the electron anti-neutrino,  $\bar{\nu}_e$ , contained 1400 liters of liquid scintillator viewed by 110 photomultiplier tubes and 200 liters of water with dissolved cadmium chloride, and was placed near the fission reactor at the Savannah River Plant in South Carolina [7].

The mechanisms behind the detector developed by Cowan and Reines worked as follows. Neutrinos from the reactor enter the detector and interact with protons in the water. The positron resulting from this reaction loses its kinetic energy via ionization and then annihilates with an electron. This creates two gamma rays which Compton scatter and initiate a cascade of electrons that causes the liquid to scintillate. Simultaneously, the neutron from the initial reaction thermalizes via collisions with protons until, eventually, it captures on a cadmium nucleus and releases about a 9 MeV gamma ray, also causing the liquid to scintillate. The time between the flash of light from the positron annihilation and that of the neutron capture is on the order of microseconds. It was by looking for this delayed-coincidence signature that Cowan and Reines were the first to successfully detect the neutrino, and thus pave the way for future neutrino experiments.

Only 6 years after the discovery by Cowan and Reines, Lederman, Schwartz, and Steinberger discovered the muon neutrino,  $\nu_\mu$  [8], but the discovery of the tau

	Fermions			Bosons	
	spin = 1/2			spin = 1	spin = 0
Generation	I	II	III	Gauge Bosons	Scalar Bosons
Quarks	u	c	t	g	H
	d	s	b	$\gamma$	
Leptons	e	$\mu$	$\tau$	Z	
	$\nu_e$	$\nu_\mu$	$\nu_\tau$	W	

**Table 1.1:** The Standard Model of particle physics, composed of fermions and their corresponding antiparticles, the force carries (gauge bosons), and the Higgs boson. The quarks and leptons are listed as fundamental representations of  $SU(2)_L$ .

neutrino,  $\nu_\tau$ , by the DONUT (Direct Observation of the Nu Tau) experiment would not occur until 44 years later [9, 10].

## 1.2 Neutrinos in the Standard Model and Beyond

The Standard Model (SM) of particle physics is the result of several decades of work by many scientists. It is a field theory that describes three of the four fundamental forces (electromagnetic, strong and weak), and classifies all known elementary particles as outlined in Table 1.1.

Classified in three generations of leptons, neutrinos exist in corresponding flavors, electron neutrinos ( $\nu_e$ ), muon neutrinos ( $\nu_\mu$ ), and tau neutrinos ( $\nu_\tau$ ), to the electron (e), muon ( $\mu$ ), and tau ( $\tau$ ) leptons, respectively. For each of these flavors a corresponding antiparticle also exists,  $\bar{\nu}_e, \bar{\nu}_\mu, \bar{\nu}_\tau$ .

If neutrinos have exactly zero mass and travel at the speed of light, then by definition their helicity, or handedness, is a conserved property. This means that there is no boosted frame in which the helicity is reversed. Since experiments only measured left-handed neutrinos [11], it was assumed that all neutrinos in the SM were massless. As will be discussed in greater depth in Section 1.3, it was later experimentally discovered that neutrinos oscillate, or change flavors, indicating that at least two of the three neutrinos must have mass.

Their ability to oscillate arises from the fact that neutrinos exist as flavor eigenstates of the weak interaction,  $\nu_\alpha$ :  $\alpha = e, \mu, \tau$ , that are not identical to their mass states,  $\nu_i$ :  $i = 1, 2, 3$ , which are eigenstates of the Hamilton describing the propagation of the free neutrino. This means that a neutrino produced at a source has a

known flavor, but its mass is described as a superposition of the mass eigenstates, creating two possible scenarios: (i) The mass states are the same as the flavor states, therefore, a neutrino produced as a  $\nu_x$  will remain  $\nu_x$  forever. (ii) The mass states and flavor states are different and at least two of the mass states are not the same, therefore, the phase between mass states will change as the neutrino propagates through time and space causing a change of flavor state. Experimental discoveries of neutrino oscillation require that the third scenario is correct.

Given this we can define the probability that a neutrino oscillates by first describing the flavor eigenstates as:

$$|\nu_\alpha\rangle = \sum_i U_{\alpha i} |\nu_i\rangle \quad (1.2)$$

where  $U_{\alpha i}$  is the unitary Pontecorvo-Maki-Nakagawa-Sakata (PMNS) mixing matrix [12]. The PMNS matrix relates flavor to mass eigenstates and can be written in factorized form as:

$$U = \begin{pmatrix} 1 & & \\ c_{23} & s_{23} & \\ -s_{23} & c_{23} \end{pmatrix} \begin{pmatrix} c_{13} & s_{13}e^{-i\delta} \\ -s_{13}e^{i\delta} & c_{13} \end{pmatrix} \begin{pmatrix} c_{12} & s_{12} \\ -s_{12} & c_{12} \end{pmatrix} \begin{pmatrix} 1 & & \\ e^{i\alpha} & e^{i\beta} & \end{pmatrix} \quad (1.3)$$

where  $s_{ij} = \sin \theta_{ij}$  and  $c_{ij} = \cos \theta_{ij}$ ,  $0 \leq \theta_{ij} \leq \pi/2$ ,  $0 \leq \delta \leq 2\pi$  is the Dirac charge parity (CP) violation phase, and  $\alpha$  and  $\beta$  are two real Majorana CP violation phases.

As a neutrino,  $\nu_\alpha$ , propagates in time the mass eigenstates evolve differently (assuming that  $m_1 \neq m_2 \neq m_3$ ), resulting in a new flavor state,  $\nu_\beta$ . Massive neutrinos move through time and space as

$$|\nu_i(x, t)\rangle = e^{-\frac{i}{\hbar}(E_i t - \vec{p}_i \cdot \vec{x})} |\nu_i(0, 0)\rangle = e^{-i\phi} |\nu_i(0, 0)\rangle \quad (1.4)$$

The flavor state  $\alpha$  at some point in time and space can then be defined as:

$$|\nu_\alpha(x, t)\rangle = \sum_i U_{\alpha i} |\nu_i(x, t)\rangle = \sum_i U_{\alpha i} e^{-i\phi_i} |\nu_i(0, 0)\rangle \quad (1.5)$$

Therefore, the oscillation probability that a neutrino produced as flavor  $\nu_\alpha$  will be

detected as flavor  $\nu_\beta$  after traveling for a period of time is given by

$$\begin{aligned}
P(\nu_\alpha \rightarrow \nu_\beta) &= |\langle \nu_\alpha(0,0) | \nu_\beta(x,t) \rangle|^2 \\
&= \left| \sum_i U_{\alpha i}^* e^{-i\phi_i} U_{\beta i} \right|^2 \\
&= \sum_i \sum_k U_{\alpha i}^* U_{\beta i} U_{\alpha k} U_{\beta k}^* e^{-i(\phi_i - \phi_k)}
\end{aligned} \tag{1.6}$$

This is true for any number of neutrino generations, but for the sake of simplicity, consider the case of two neutrino oscillation. In this scenario the mixing matrix can be written as

$$U = \begin{pmatrix} U_{\alpha 1} & U_{\alpha 2} \\ U_{\beta 1} & U_{\beta 2} \end{pmatrix} = \begin{pmatrix} \cos \theta_{12} & \sin \theta_{12} \\ -\sin \theta_{12} & \cos \theta_{12} \end{pmatrix} \tag{1.7}$$

Therefore, the probability of oscillation is given by

$$\begin{aligned}
P^{2\nu}(\nu_\alpha \rightarrow \nu_\beta) &= |U_{\alpha 1}|^2 |U_{\beta 1}|^2 + |U_{\alpha 2}|^2 |U_{\beta 2}|^2 + U_{\alpha 1}^* U_{\beta 1} U_{\alpha 2} U_{\beta 2}^* (e^{i(\phi_2 - \phi_1)} + e^{-i(\phi_2 - \phi_1)}) \\
&= \sin^2 2\theta_{12} \sin^2 \left( \frac{\phi_2 - \phi_1}{2} \right)
\end{aligned} \tag{1.8}$$

Now, recall that

$$\phi_i = \frac{1}{\hbar} (E_i t - \vec{p}_i \cdot \vec{x}) \tag{1.9}$$

The mass of the neutrino is very small compared to its energy ( $m_\nu \ll E_\nu$ ) so the momentum can be approximated as

$$p_i = \frac{1}{c} \sqrt{E_i^2 - m_i^2 c^4} \approx \frac{1}{c} \left( E_i - \frac{m_i^2 c^4}{2E_i} \right) \tag{1.10}$$

If it is reasonably assumed that neutrinos move at the speed of light,  $c$ , then the phase difference,  $\phi_2 - \phi_1$ , can be approximated as

$$\begin{aligned}
\phi_2 - \phi_1 &\approx \frac{1}{\hbar} \left( (E_2 - E_1) \frac{L}{c} - (p_2 - p_1)L \right) \\
&\approx \frac{1}{\hbar} \frac{L}{c} \left( \frac{m_2^2 c^4}{2E_2} - \frac{m_1^2 c^4}{2E_1} \right) \\
&\approx \frac{L}{\hbar c} \frac{\Delta m_{21}^2 c^4}{2E}
\end{aligned} \tag{1.11}$$

where  $t = \frac{L}{c}$ ,  $\Delta m_{21}^2 = m_2^2 - m_1^2$  and  $E_1 = E_2 = E$ .

It can now be shown that the oscillation probability of a neutrino  $\nu_\alpha$ , being detected as flavor  $\nu_\beta$  at a distance  $L$  from a source in the two neutrino mixing case is

$$\begin{aligned} P^{2\nu}(\nu_\alpha \rightarrow \nu_\beta) &= \sin^2(2\theta_{12}) \sin^2\left(\frac{(\Delta m_{12}c^2)^2}{4\hbar c} \frac{L}{E}\right) \\ &= \sin^2(2\theta_{12}) \sin^2\left(1.27\Delta m_{12}^2 \frac{L}{E}\right) \end{aligned} \quad (1.12)$$

for  $\Delta m_{12}^2$  in eV<sup>2</sup> and  $L/E$  in m/MeV. The corresponding survival probability, the chance that a neutrino  $\nu_\alpha$  is detected as  $\nu_\alpha$ , can be described by  $P^{2\nu}(\nu_\alpha \rightarrow \nu_\alpha) = 1 - P^{2\nu}(\nu_\alpha \rightarrow \nu_\beta)$ .

There are several aspects of note about this probability. It can be seen that the amplitude of the oscillation probability,  $\sin^2(2\theta_{12})$ , depends on the mixing angle  $\theta_{12}$ , while the mass splitting,  $\Delta m_{12}^2$ , and the energy of the neutrino,  $E$ , determine the frequency of oscillation. The probability is non-zero only when  $\Delta m_{12}^2$  is non-zero, indicating that if an experiment observes neutrino oscillation, then at least one of the neutrinos must have mass. Finally, the dependence of oscillation on the factor  $\frac{L}{E}$  allows experiments to decide the placement of neutrino detectors based on what features of neutrinos they would like to study. Theoretical models alone do not prove neutrino oscillation, however.

### 1.3 Discovery of Neutrino Oscillation

In the late 1960's, about a decade after Cowan and Reines discovered the first neutrino, astrophysicist John Bahcall and physical chemist Raymond Davis designed an experiment to collect and count solar neutrinos, neutrinos emitted by nuclear fusion taking place in the Sun. Davis placed a 380 cubic meter tank filled with perchloroethylene (dry-cleaning fluid) 1,478 meters underground in the Homestake Gold Mine in South Dakota. Perchloroethylene was chosen because it is rich in chlorine and the tank was placed deep underground to shield the experiment from cosmic rays.

Davis was looking for the reaction



in which a neutrino would enter the tank and transform chlorine into argon. Argon

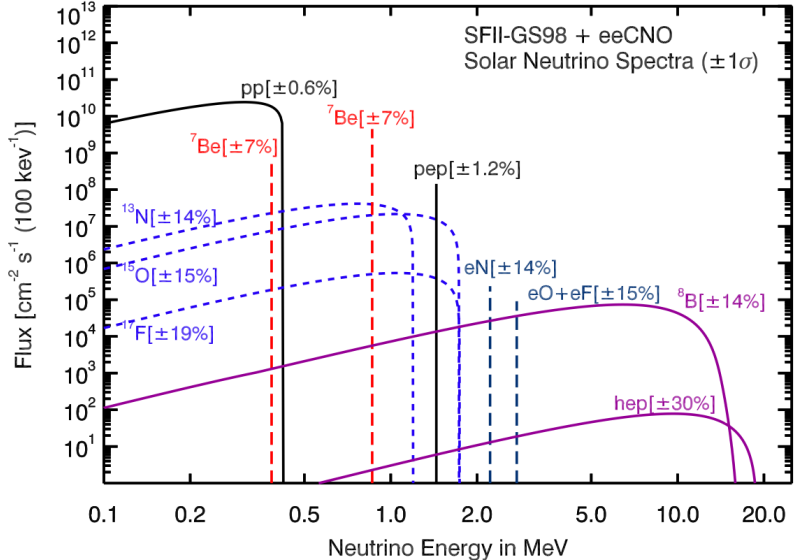


**Figure 1.1:** Spectrum of solar neutrino fluxes corresponding to the SFII-GS98 standard solar model. Electron capture CNO neutrinos (ecCNO) have been added in addition to standard fluxes. Electron capture fluxes are given in  $\text{cm}^{-2}\text{s}^{-1}$ . Figure from Ref. [13].

is a noble gas, making it easy to chemically separate from a large amount of chlorine-rich solvent, and has a half-life of 35.011 days [14]. This allowed Davis to extract the argon gas and count the number of decays, essentially counting the number of neutrinos that had been captured. The chlorine reaction has a threshold of 814 keV, which, according to standard solar models (see Figure 1.1), allowed the Homestake experiment to detect neutrinos created by  ${}^8\text{B}$  in the sun (and  ${}^7\text{Be}$ ,  $pep$ ,  ${}^{13}\text{N}$ , and  ${}^{15}\text{O}$  at lower rates).

In the end, with the Homestake experiment Davis measured a rate of solar neutrinos that was one third of the rate predicted by calculations made by Bahcall using the Standard Model [15]. This discrepancy became known as the solar neutrino problem, and in the following years Bruno Pontecorvo wrote several theoretical papers proposing neutrino oscillation as a solution [16, 17].

Several experiments designed to measure the flux of solar neutrinos followed the Homestake Experiment including SAGE [18], GALLEX [19], and GNO [20, 21]. All three experiments built detectors based on the reaction  ${}^{71}\text{Ga}(\nu, e^-){}^{71}\text{Ge}$  which has a threshold of 233 keV. This made them sensitive to neutrinos created by  $pp$  reactions in the Sun, neutrinos that the Homestake experiment was unable to measure. Even

with the different energy threshold, though, all three experiments showed a deficit in neutrino flux compared to Standard Model calculations and the solar neutrino problem persisted.

Further experimental evidence for neutrino oscillation came with results from the Super-Kamiokande Experiment. Unlike previous experiments that were only sensitive to electron neutrinos, Super-K detected neutrinos through elastic scattering of electrons - a process sensitive to all neutrino flavors. Operating at a high threshold of 4 MeV they observed pure  ${}^8\text{Be}$  solar neutrinos, a different selection than previous solar neutrino experiments. With their large mass, good energy resolution, and ability to determine neutrino directionality, Super-K was able to show an increased neutrino rate in the direction of the sun, confirming the solar neutrino problem effect with high statistics and place limits on the parameters of oscillation [22].

The first clear evidence for solar neutrino flavor change came from the Sudbury Neutrino Observatory (SNO) in 2001 [23, 24]. The SNO detector was an imaging Cherenkov detector using heavy water. They were able to observe neutrino flavor change through three different processes:

- (i)  $\nu_x + e^- \rightarrow \nu_x + e^-$ , elastic scattering of electrons
- (ii)  $\nu_e + d \rightarrow e^- + p + p$ , charged current reaction (CC)
- (iii)  $\nu_x + d \rightarrow \nu_x + p + n$ , neutral current reaction (NC)

The CC reaction has a threshold of 1.4 MeV, allowing SNO to accurately measure the shape of the  ${}^8\text{B}$  neutrino spectrum. The CC is also only sensitive to  $\nu_e$ , whereas the NC reaction is sensitive to all three active neutrino flavors, allowing SNO to compare measured fluxes from each reaction, knowing that the full neutrino flux from the Sun was accounted for and ultimately confirm the theory of neutrino oscillation. See Figure 1.2 for a comparison of the measured solar neutrino flux from SNO to previously mentioned solar neutrino experiments and theoretical predictions.

Nearly a century after the initial postulation of the neutrino the scientific community has in hand experimental evidence of three neutrino flavors, mathematical models that include these neutrinos in the Standard Model of Particle Physics, theoretical and experimental proof that neutrinos oscillate and therefore have mass, and measurements of all known mixing angles. These findings, along with developments in technology and techniques, set the stage for current, and future, neutrino experiments

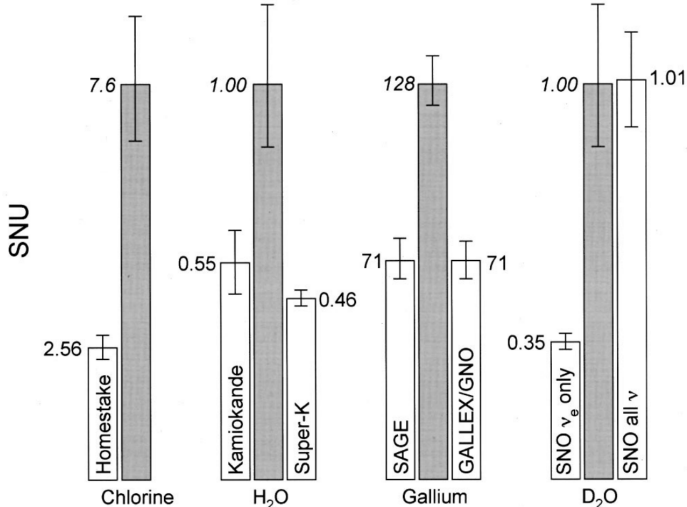


**Figure 1.2:** A comparison of the measured solar neutrino flux from six experiments along with theoretical predictions of Bahcall *et al.* [25] (shaded gray). The height of the bars for predictions have been made the same for visual comparison. [26]

to transform their goals from observing anomalies to making precise measurements of the physics behind the anomalies. The current best-fit values of the 3-neutrino oscillation parameters as found experimentally are shown in Table 1.2.

In the search for measuring these parameters hints have arisen at the existence of additional neutrino states with masses at the eV scale, implying the possibility of sterile neutrinos which mix with the active neutrinos. The Liquid Scintillator Neutrino Detector at the Los Alamos Neutron Science Center found an excess of events over background while measuring  $\bar{\nu}_\mu \rightarrow \bar{\nu}_e$  oscillations which suggest a neutrino with mass greater than  $0.4 \text{ eV}^2/c$  [27]. The MiniBooNE experiment also observed an excess of events consistent with antineutrino oscillations in the  $0.01 < \Delta m^2 < 1.0 \text{ eV}^2$  range [28, 29, 30]. The GALLEX [31, 32] and SAGE [33, 34, 35] experiments measured a number of events  $2.8\sigma$  lower than prediction, the “Gallium anomaly” [36, 37], suggesting the possibility of short-baseline neutrino oscillations. Further information on light sterile neutrinos can be found in [38].

Parameter	Best-fit	$3\sigma$
$\Delta m_{21}^2$ [10 <sup>-5</sup> eV <sup>2</sup> ]	7.37	6.93 - 7.96
$\Delta m_{31(23)}^2$ [10 <sup>-3</sup> eV <sup>2</sup> ]	2.56 (2.54)	2.45 - 2.69 (2.42 - 2.66)
$\sin^2 \theta_{12}$	0.297	0.250 - 0.354
$\sin^2 \theta_{23}$	0.425 (0.589)	0.381 - 0.615 (0.384 - 0.636)
$\sin^2 \theta_{13}$	0.0215 (0.0216)	0.0190 - 0.0240 (0.0190 - 0.0242)
$\delta/\pi$	1.38 (1.31)	2 $\sigma$ : 1.0 - 1.9 (2 $\sigma$ : 0.92 - 1.88)

**Table 1.2:** The current best-fit values and  $3\sigma$  allowed ranges of the 3-neutrino oscillation parameters as determined experimentally [12]. The values (values in brackets) correspond to  $m_1 < m_2 < m_3$  ( $m_3 < m_1 < m_2$ ).

# CHAPTER 2

## REACTOR NEUTRINOS

Fission of isotopes used in reactor fuel cause a chain reaction that results in several  $\beta$  decays, creating electron antineutrinos,  $\bar{\nu}_e$ . For this reason, nuclear reactors are a powerful and pure source of  $\bar{\nu}_e$ , meaning that there are no reactions taking place in the reactor that create the other active neutrino flavors. The first neutrino was discovered using the nuclear reactor at the Savannah River Plant due to its continuous flux of  $\bar{\nu}_e$  and the ability to get close to the core. A host of current neutrino experiments are located at reactors, making it important to understand the reactor neutrino flux and spectrum.

### 2.1 Production of Reactor Neutrinos

Nuclear reactors are powered by the fission of uranium and plutonium isotopes in their cores. Specifically, in a power reactor, 99.9% of the power comes from the fission of  $^{235}\text{U}$ ,  $^{239}\text{Pu}$ ,  $^{241}\text{Pu}$ , and  $^{238}\text{U}$  isotopes and the subsequent beta decays. The reaction begins with a neutron colliding with a nucleus of one of the isotopes. This causes the nucleus to split into two neutron-rich fragments, usually of unequal mass, creating an unstable system. In order to reach stability neutrons have to transform into protons, a process accomplished through  $\beta$  decay, see Figure 2.1. On average each daughter  $\beta$  decays three times to reach stability. Each beta decay produces an electron and corresponding electron antineutrino. In general a nuclear reactor will produce  $\sim 6 \times 10^{20} \bar{\nu}_e$  per GW of thermal energy power [39].

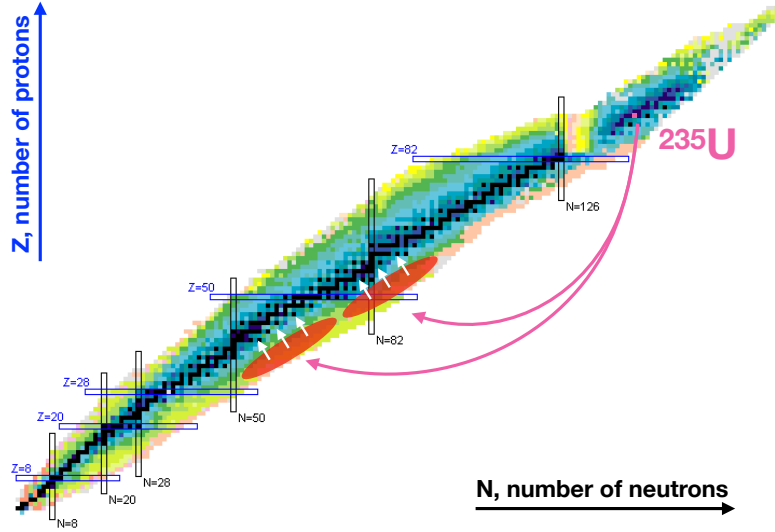


**Figure 2.1:** A schematic of the fission of  $^{235}\text{U}$  [40]. After collision with a neutron  $^{235}\text{U}$  will split into two unstable, neutron-rich nuclei (arrows, pink) which will then  $\beta$  decay (arrows, white) until stable.

## 2.2 Measuring the Reactor Antineutrino Flux and Spectrum

The total  $\bar{\nu}_e$  flux,  $S(E_\nu)$ , produced by a nuclear reactor can be expressed as the sum over the spectra of the dominant fissioning isotopes,

$$S(E_\nu) = \frac{W_{th}}{\sum_i(f_i/F)e_i} \sum_i \frac{f_i}{F} \left( \frac{dN_i}{dE_\nu} \right), \quad (2.1)$$

where  $f_i/F$  is the fission fraction for each given isotope  $i$ ,  $W_{th}$  is the reactor thermal energy,  $e_i$  is the average energy released per fission by each isotope, and  $dN_i/dE_\nu$  is the cumulative  $\bar{\nu}_e$  spectrum of  $i$  normalized per fission [39].

There are two methods used to determine the  $\bar{\nu}_e$  spectrum, *ab initio* summation and electron spectrum conversion. In the *ab initio* approach the spectrum is determined by summing the contributions of all  $\beta$ -decay branches of all fission fragments,

$$\frac{dN_i}{dE_{\bar{\nu}}} = \sum_n Y_n(Z, A, t) \sum_i b_{n,i}(E_0^i) P_{\bar{\nu}}(E_{\bar{\nu}}, E_0^i, Z), \quad (2.2)$$

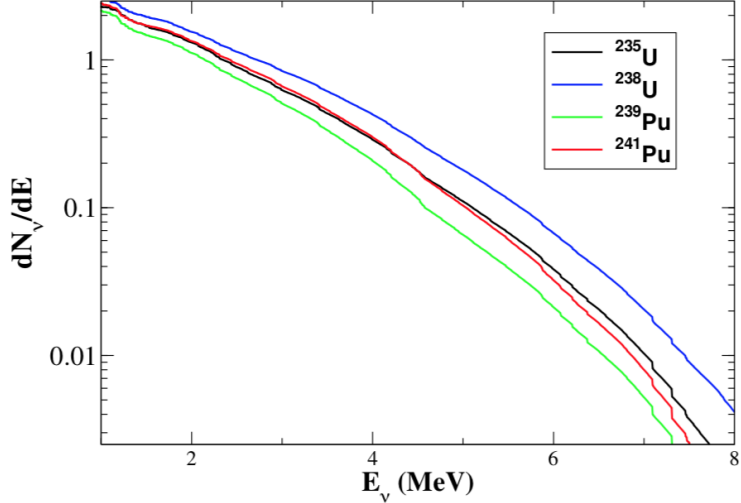


**Figure 2.2:** The  $\bar{\nu}_e$  spectrum predicted by the summation method using the JEFF-3.1.1 database fission fragment yields and the ENDF/B-VII.1 decay library [39].

where  $Y_n(Z, A, t)$  is the number of  $\beta$  decays of the fission fragment  $Z, A$  at time  $t$ ,  $b_{n,i}(E_0^i)$  are the branching ratios with endpoint energies  $E_0^i$ , and  $P_{\bar{\nu}}(E_{\bar{\nu}}, E_0^i, Z)$  is the normalized  $\bar{\nu}_e$  spectrum for the branch  $n, i$  [39]. This method relies on nuclear databases, such as the Evaluated Nuclear Data File (ENDF) [41] and Joint Evaluated Fission and Fusion Data Library (JEFF) [42] for fission yields of daughter products, and the Evaluated Nuclear Structure Data File (ENSDF) [82] for spectra, branching ratios and endpoint energies. The antineutrino spectrum for the four main reactor isotopes calculated using *ab initio* summation was done in Ref. [39] and the result can be seen in Figure 2.2.

Though seemingly straightforward, this approach comes with some caveats. The sheer number of daughter isotopes ( $>1000$ ) and individual  $\beta$  decay branches ( $>6000$ ) make the summation non-trivial. This, along with the fact that not all branching ratios are known, and that the fission yields have been determined by several different database groups but don't always agree and have large uncertainties bring into question the validity of using only this method.

The other approach to determining the  $\bar{\nu}_e$  spectrum, sometimes called the conversion method, relies on converting a measured electron spectrum into an antineutrino spectrum. This involves fitting an experimentally defined total beta spectrum with

individual beta spectra according to their amplitudes,  $a_i$ ,

$$\frac{dN_i}{dE_e} = \sum_i a_i P(E, E_0^i, Z) \quad (2.3)$$

The conversion to the antineutrino spectrum is then accomplished by replacing the energy  $E_e$  in each branch by  $E_0 - E_{\bar{\nu}}$ , because the electron and the  $\bar{\nu}_e$  share the total energy of each  $\beta$ -decay branch. The flux per fission is then given as the sum of  $\bar{\nu}_e$  spectrum converted from each virtual  $\beta$  branch,

$$\frac{dN_i}{dE_{\bar{\nu}}} = \sum_i a_i P(E_0^i - E, E_0^i) \quad (2.4)$$

The electron spectra for  $^{235}\text{U}$ ,  $^{239}\text{Pu}$ , and  $^{241}\text{Pu}$  were measured at the Institut Laue-Langevin (ILL) reactor in Grenoble, France in the 1980s [43, 44, 45], while the spectrum of  $^{238}\text{U}$  was more recently (2014) measured at the neutron source FRMII in Garching, Germany [46]. The ILL measurements, along with a prediction of the  $^{238}\text{U}$   $\bar{\nu}_e$  spectrum using the summation method by Vogel [47], became known as the “ILL-Vogel” flux model and was the main model used until 2011.

In 2011 Mueller *et al.* improved the prediction of the reactor antineutrino spectra by employing a method that combined information from the nuclear databases and the measured electron spectra from ILL [48]. This was followed by a further improvement by Huber who applied higher order corrections making use of the conversion method and minimizing the use of the databases as much as possible [49].

Though much work has been done to accurately model the reactor antineutrino spectra both methods are subject to uncertainties in the subdominant corrections to beta-decay. This includes radiative, weak magnetism, and finite size corrections along with uncertainties in the spectrum shape of forbidden transitions which are summarized in [39].

Besides the model uncertainties there are also experimental uncertainties that arise from knowing the thermal power of the reactor, its time-dependent fuel composition, and the fission energies of the dominant isotopes. All of these uncertainties result in a 10-20% relative uncertainty on the reactor antineutrino spectra using the *ab initio* method and  $\sim 5\%$  uncertainty on the conversion approach [50].

## 2.3 Detection of Reactor Neutrinos

Though there are several methods that can be used to detect reactor neutrinos, including charge-current ( $\bar{\nu}_e + d \rightarrow n + n + e^+$ ), neutral-current ( $\bar{\nu}_e + d \rightarrow n + p + \bar{\nu}_e$ ), and antineutrino-electron elastic scattering ( $\bar{\nu}_e + e^- \rightarrow \bar{\nu}_e + e^-$ ) [22, 23], the one employed by most experiments is IBD ( $\bar{\nu}_e + p \rightarrow e^+ + n$ ). The IBD reaction threshold, in the frame in which the proton is at rest, is given by

$$E_{\text{thresh}} = \frac{(M_n + m_e)^2 - M_p^2}{2M_p} \approx 1.806 \text{ MeV} \quad (2.5)$$

where  $M_n$ ,  $m_e$ , and  $M_p$  are the mass of the neutron, electron, and proton respectively and the mass of the antineutrino is neglected.

The cross section of this reaction, to zeroth order in  $1/M$  (where  $M$  is the nucleon mass) can be written as

$$\sigma^{(0)} = \frac{2\pi^2/m_e^2}{f^R \tau_n} E_e^{(0)} p_e^{(0)} \approx 9.52 \times \left( \frac{E_e^{(0)} p_e^{(0)}}{\text{MeV}^2} \right) \times 10^{-44} \text{ cm}^2 \quad (2.6)$$

where  $\tau_n$  is the neutron decay lifetime,  $f^R = 1.7152$  is the neutron decay phase-space factor that includes the Coulomb, weak magnetism, recoil, and outer radiative corrections, and  $E_e$  and  $p_e$  are the energy momentum of the final-state positron [39]. At reactor energies, though, first order corrections in  $1/M$  should be included [51] and the resulting IBD cross section as a function of neutrino energy can be seen in Figure 2.3.

An IBD event is selected by a pair of coincident signals consisting of a positron ionization and annihilation as the prompt signal and a time delayed neutron capture on a proton or nucleus as the delay signal. The positron, carrying most of the  $\bar{\nu}_e$  energy, will produce two 511 keV gammas as a result of the pair annihilation, which means that the minimum energy of the prompt signal is 1.022 MeV. These two gammas will Compton scatter initiating a release of more electrons which will scintillate. The positron ionization, annihilation, and Compton scattering are detected as one signal, giving the prompt energy,  $E_{\text{prompt}}$ .

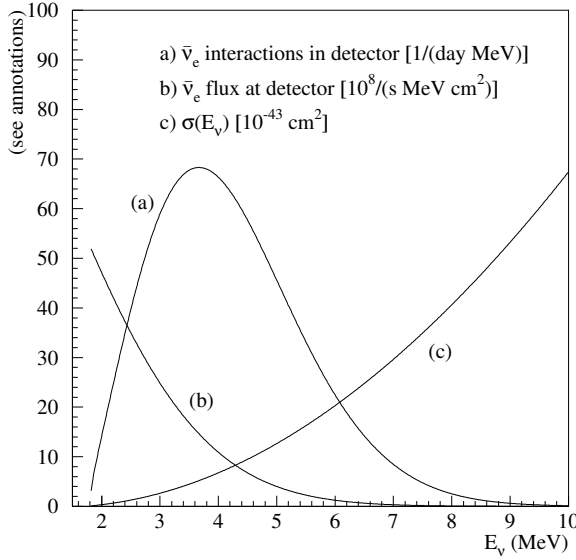


**Figure 2.3:** The IBD spectrum (curve (a)) measured by a 12-ton fiducial mass detector located 0.8 km from a 12-GW<sub>th</sub> power reactor along with the reactor flux (curve (b)) and IBD cross section (curve (c)) as a function of energy [12].

The neutrino energy,  $E_{\bar{\nu}_e}$ , can then be backtracked from this prompt signal as

$$\begin{aligned} E_{\bar{\nu}_e} &= E_{\text{prompt}} + (1.8 \text{ MeV} - 1.022 \text{ MeV}) + T_n \\ &\approx E_{\text{prompt}} + 0.78 \text{ MeV} \end{aligned} \quad (2.7)$$

where  $T_n$  is the kinetic energy of the recoil neutron which is much smaller than the energy of the neutrino and can therefore be ignored in most cases. The IBD cross-section increases with energy, whereas the  $\bar{\nu}_e$  spectrum decreases with energy creating a detected antineutrino energy spectrum that peaks around 3.8 MeV and decreases to zero above  $\sim 8$  MeV, as seen in Figure 2.3. In addition to great background rejection and good reconstruction of the neutrino energy, the IBD method of detecting neutrinos also allows the use of liquid scintillators and water as detection mediums.

## 2.4 The Reactor Antineutrino Anomaly

Several experiments have, and continue to use reactor antineutrinos as a probe of neutrino oscillation. A reactor neutrino disappearance  $P(\bar{\nu}_e \rightarrow \bar{\nu}_e)$  experiment can measure the mixing angle  $\theta_{13}$  by placing their detector near the first maximum

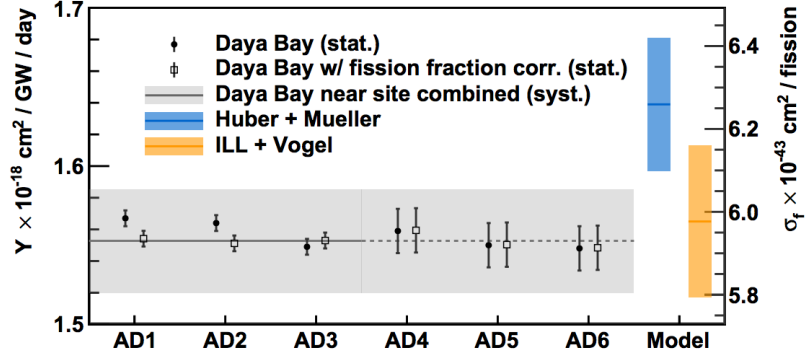


**Figure 2.4:** Rate of reactor antineutrino candidate events in Daya Bay’s six detectors [58]. The average of the three near detectors is shown as the gray line, extended though the far detectors as a dotted gray line. Also shown are the rates predicted using the Huber+Mueller (blue) and ILL+Vogel (orange) models.

of  $\sin^2 \left( \frac{\Delta m_{31}^2 L}{4E} \right)$ , for which the amplitude of the oscillation gives  $\sin^2 2\theta_{13}$  (recall Eq. 1.12). In the late 1990’s the CHOOZ [52, 53] and Palo Verde [54] experiments attempted to do this by placing their detectors at a baseline of  $\sim 1$  km from a nuclear reactor, but neither observed oscillations.

Though unsuccessful in making a measurement of  $\theta_{13}$ , the work of these collaborations helped to inform the decisions of successor experiments, Daya Bay in China, RENO in Korea, and Double Chooz in France. It should also be noted here that the Kamioka Liquid scintillator Anti-Neutrino Detector (KamLAND) experiment was successful in making measurements of  $\theta_{12}$  and  $\Delta m_{12}^2$  by placing their detectors at a long baseline of, on average, 180 km [55, 56].

The Daya Bay Reactor Neutrino Experiment was located at the Daya Bay nuclear reactor power plant in southern China that consists of six 2.9 GW<sub>th</sub> reactors. They employed antineutrino detectors (AD) near and far from the reactors so that they could make a relative comparison of rates in order to suppress the reactor flux uncertainties [57, 58]. The IBD yield measured for each AD is shown in Figure 2.4 and it can be seen that, after correcting for small variations of fission fractions among the different sites, all rates are consistent with each other. Though results between detectors agree, the disagreement between the experimental results and most recent model calculations (Huber+Mueller) is significant.

In order to obtain a wider picture, the Daya Bay average IBD yield at the flux-weighted baseline (573 m) of the two near detector sites was compared to measure-

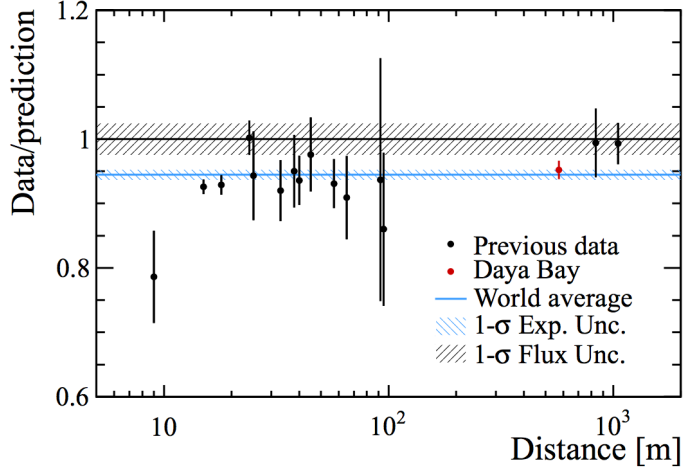


**Figure 2.5:** The measured reactor  $\bar{\nu}_e$  rate, normalized to the Huber+Mueller model prediction, as a function of distance from the reactor [59]. The rate is corrected for 3-flavor neutrino oscillations at each baseline. The blue shaded region represents the global average and its  $1\sigma$  uncertainty. The  $2.7\sigma$  model uncertainty is shown as a band around unity.

ments from nineteen other short-baseline ( $<1000$  m) experiments as shown in Figure 2.5. The global average, including the most recent Daya Bay calculation, results in a ratio of measured to expected yield of  $0.945 \pm 0.007$  (exp.)  $\pm 0.023$  (model) with respect to the Huber+Mueller model, a  $\sim 6\%$  deficit [59]. If the model uncertainty is to be trusted this ratio suggests reactor  $\bar{\nu}_e$  disappearance as close as  $L < 10$  m, a phenomenon not covered in the standard 3-flavor neutrino mixing model [39]. This discrepancy has been labeled the “Reactor Antineutrino Anomaly” (RAA).

One hypothesis for explaining the reactor anomaly is that reactor neutrinos are oscillating into a new type of neutrino, a sterile neutrino. A sterile neutrino does not take part in weak interactions except those induced by mixing with active neutrinos [38]. Anomalous results that might be explained by sterile neutrinos are also not confined to reactor experiments. Specifically, the Liquid Scintillation Neutrino Detector (LSND) measured an excess of  $\bar{\nu}_e$  ( $>3\sigma$ ) events [27] along with excesses measured by the Mini Booster Neutrino Experiment (MiniBooNE) of  $\nu_e$  ( $3.4\sigma$ ) and  $\bar{\nu}_e$  ( $2.8\sigma$ ) [60]. Two solar neutrino detectors, the SovietAmerican Gallium Experiment (SAGE) and Gallium Experiment (GALLEX), have observed a deficit in electron neutrinos produced by intense artificial  $^{51}\text{Cr}$  and  $^{37}\text{Ar}$  radioactive sources at a significance of  $3\sigma$  [61].

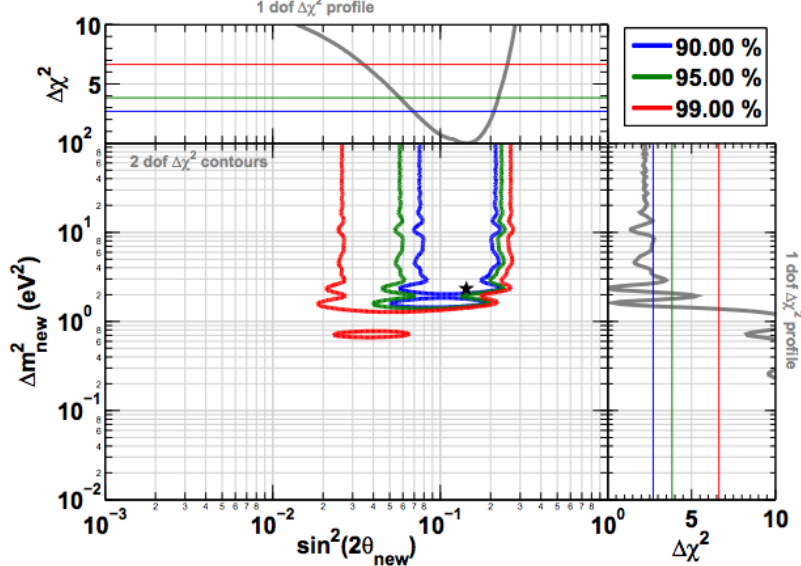


**Figure 2.6:** Allowed regions in the  $\sin^2(2\theta_{14}) - \Delta m_{14}^2$  plane resulting from a fit of the 3+1 neutrino model to results from reactor neutrino experiments, SAGE and GALLEX, MiniBooNE, and spectrum measurements from ILL. This global fit results in the constraints  $\Delta m_{14}^2 > 1.5 \text{ eV}^2$  and  $\sin^2(2\theta_{14}) = 0.14 \pm 0.08$  [62].

If these anomalies are taken as evidence of short-baseline oscillations of electron neutrinos, the simplest way to explain these discrepancies is to add onto the standard model using the 3+1 oscillation model in which there are three active neutrinos and one sterile. This would introduce three new mixing angles,  $\theta_{14}$  being the one of interest in reactor neutrino experiments. A global fit of this model to neutrino data, including results from reactor experiments, SAGE and GALLEX, MiniBooNE, and spectrum measurements from ILL, results in oscillation constraints  $\Delta m_{14}^2 > 1.5 \text{ eV}^2$  and  $\sin^2(2\theta_{14}) = 0.14 \pm 0.08$ , as shown in Figure 2.6 [62].

An alternative explanation is that the flux predictions are incorrect and have larger uncertainties than those currently applied. The idea that the calculated reactor antineutrino flux is not well understood is bolstered by results from Daya Bay [58], RENO [63], and Double Chooz [64] in which a “bump” was observed in the experimentally measured antineutrino energy spectrum relative to the model spectrum, shown in Figure 2.7.

In an effort to better understand what aspect of the reactor  $\bar{\nu}_e$  model is causing the disagreement from data, Data Bay measured changes in the reactor antineutrino flux and spectrum as a function of reactor fuel evolution [65]. As a reactor burns

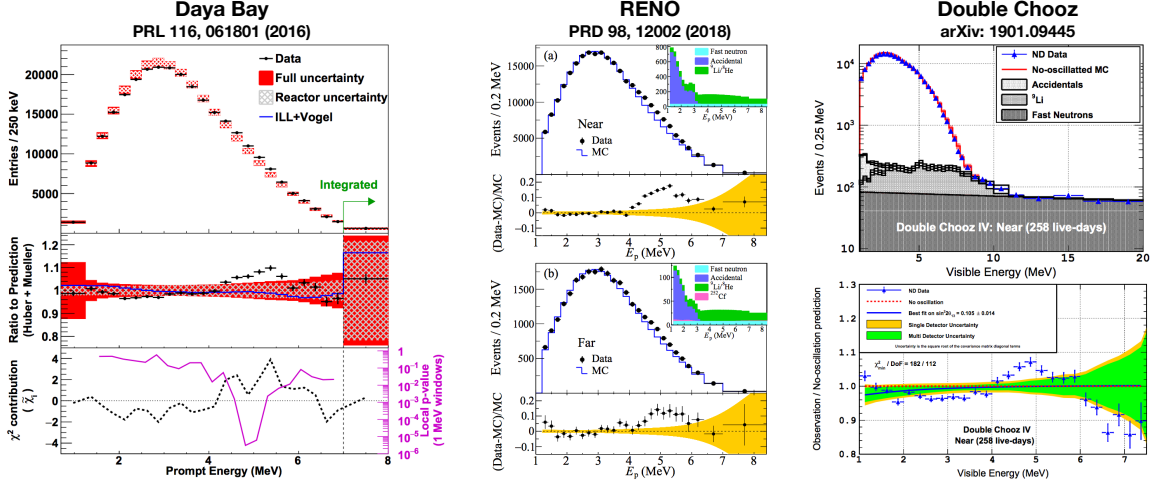


**Figure 2.7:** A comparison between the predicted and measured prompt energy spectra of IBD events in Daya Bay [58], RENO [63], and Double Chooz [64]. All experiments observe an excess of events above uncertainty in the model spectrum in the 4-6 MeV region.

fuel the relative fraction of fission isotopes  $^{235}\text{U}$ ,  $^{238}\text{U}$ ,  $^{239}\text{Pu}$ , and  $^{241}\text{Pu}$  in the core changes. Antineutrino fluxes and spectra differ depending on the fission isotope that is producing the antineutrinos, so, as the reactor runs the  $\bar{\nu}_e$  spectrum is changing.

By measuring the evolution of the IBD energy spectrum Daya Bay concluded that incorrect predictions of the  $^{235}\text{U}$  flux may be the primary contributer to the reactor antineutrino anomaly. They disfavored a model in which there is an equal deficit from all reactor fission isotopes, implying the existence of a sterile neutrino, at  $2.6\sigma$ . These results were also confirmed by a similar study completed by RENO [66]. Whether the reactor antineutrino anomaly can be solved by the addition of a sterile neutrino, more accurate reactor flux models, or a combination of both is a topic of great interest in the neutrino community and several experiments have been designed to address this matter.

# CHAPTER 3

## THE PROSPECT EXPERIMENT

The scientific community’s understanding of neutrinos has come a long way from Pauli’s initial proposition of its existence in 1930. Though three active neutrino flavors and their behaviors are understood and well included in the Standard Model of particle physics, recent anomalies in reactor neutrino experiment results hint at the possibility of new physics. The discovery of an eV-scale sterile neutrino would have wide ranging impacts on the field of neutrino physics and future experiments.

The Precision Reactor Oscillation and Spectrum Experiment (PROSPECT) is designed to address the reactor antineutrino anomaly by performing a reactor-model independent search for short-baseline  $\bar{\nu}_e$  oscillations and making a precise measurement of the  $^{235}\text{U}$   $\bar{\nu}_e$  energy spectrum at a highly-enriched uranium (HEU) research reactor [67]. Located at the High Flux Isotope Reactor (HFIR) at Oak Ridge National Laboratory (ORNL) in Tennessee PROSPECT also demonstrates successful application of techniques for antineutrino detection at the surface with little overburden. PROSPECT collected data from May to December of 2018 and the first oscillation and spectrum results, with 33 and 40.3 live-days of reactor on and off time respectively, can be found in [1, 2].

### 3.1 Experimental Site

#### 3.1.1 HFIR

HFIR is a compact research reactor that burns highly enriched uranium fuel ( $^{235}\text{U}$ ), meaning that  $> 99\%$  of fissions during a reactor cycle will be from  $^{235}\text{U}$ . The HFIR

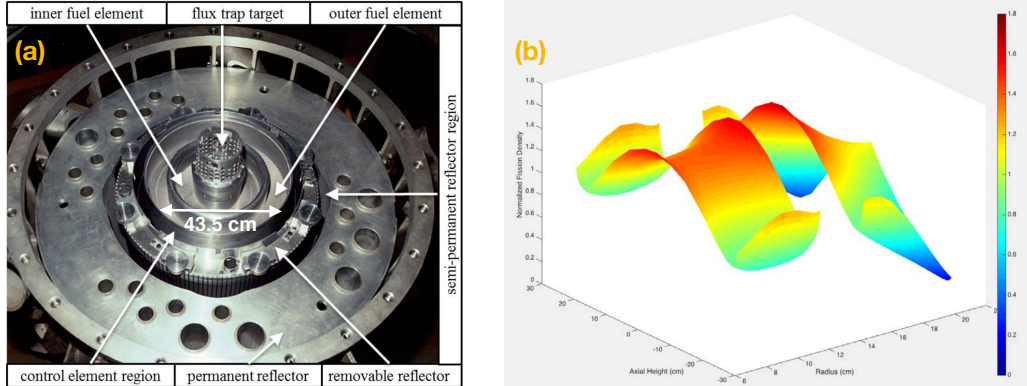


**Figure 3.1:** (a) The HFIR core, showing the inner and outer fuel elements and the flux trap region, as well as the control elements and Beryllium reflectors. (b) The relative fission density distribution at the start of a cycle. [68]

core consists of two concentric fuel elements with an outer diameter of 0.435 m and a height of 0.508 m, surrounded by control elements and Beryllium reflectors as shown in Figure 3.1. The reactor typically operates at 85 MW for seven 24-day cycles per year for a duty cycle of  $\sim 46\%$ .

### 3.1.2 Backgrounds at HFIR

The PROSPECT detector is located at ground level  $\sim 7$  m from the HFIR core and separated from the reactor water pool by a 1 m thick concrete wall, shown in Figure 3.2. The proximity to the reactor, reactor-related research activities (neutron beam lines) that happen below the detector site, and lack of overburden introduces a significant level of background events from the reactor and cosmogenic sources. These events can be classified into two categories, (i) random uncorrelated events, or singles, due to gammas from reactor related activities, charged particles from cosmogenic radiation, and backgrounds from natural radiation and (ii) correlated or “coincident” events that mimic an IBD signature. Extensive studies on the types and rate of background events at the detector site can be found in [69, 70, 71].

The largest source of gamma backgrounds was discovered to originate in the reactor pool wall, specifically an unused beam line that lies directly in front of the detector. In order to lower these backgrounds a lead shield wall (3.0 m wide, 2.1 m tall, and on average 0.10 m thick), along with shorter flanking walls on each side and a mini-wall placed at the opening of the beam line, was installed between the pool

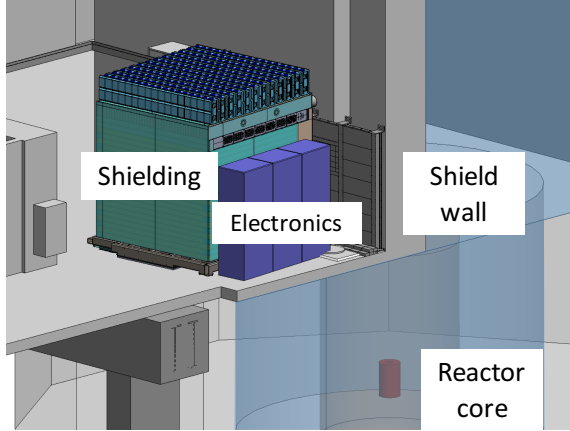


**Figure 3.2:** Layout of the PROSPECT experiment. The detector is installed in the HFIR Experiment Room next to the water pool and 5 m above the HFIR reactor core (red). The floor below contains multiple neutron beam-lines and scattering experiments.

wall and the detector. Other background events were shown to come from neutron beam-lines and scattering experiments existing below the detector site, but most of these are suppressed by a concrete monolith that the detector sits on.

The thermal neutron rate was measured to be  $\sim 2/\text{cm}^2/\text{s}$  during reactor operation [69], so layers of shielding containing  $^{10}\text{B}$ , which has a large thermal neutron cross-section and minimal gamma emission, were used in the passive shielding that surrounds the detector (see Section 3.2.2). The locally installed shield wall, along with the addition of passive shielding, resulted in a sufficient suppression of background such that a better than one-to-one signal to background ratio for antineutrino IBD events was achieved.

## 3.2 Design

The PROSPECT antineutrino detector (AD) consists of a segmented inner detector filled with  $^6\text{Li}$  doped liquid scintillator (LiLS), contained in an acrylic and aluminum tank, and surrounded by layers of passive shielding. The active detector is made up of a 14 horizontal  $\times$  11 vertical array of optically separated segments, viewed on each end by a photomultiplier tube (PMT) enclosed in an acrylic housing. Each segment is 1.176 m in length and has a 0.145 m  $\times$  0.145 m square cross-sectional area. The AD is placed with the segments parallel to the reactor pool wall,  $\sim 7$  m from the reactor

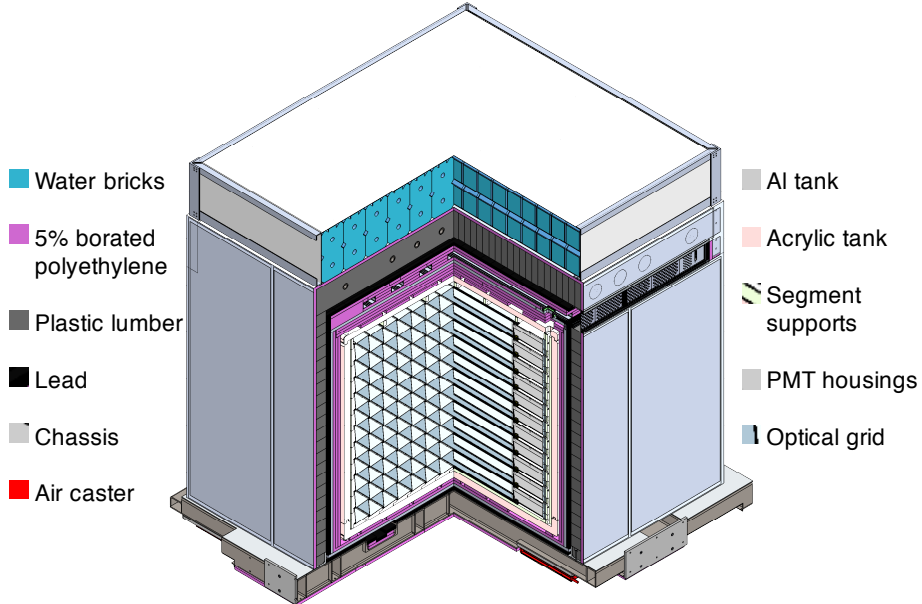


**Figure 3.3:** A cutaway view of the PROSPECT detector, including the inner detector, outer containment vessels, and passive shielding.

core, and measures  $\sim 3$  m tall including all shielding. See Figure 3.3 for a schematic of the detector.

### 3.2.1 Active Detector

#### 3.2.1.1 PMT Housings

A total of 308 PMTs are installed in the AD; 240 Hamamatsu R6594 SEL PMTs used in the inner segments (fiducial volume) and 68 ADIT Electron Tubes 9372KB PMTs used in the outer segments as shown in Figure 3.4. Each PMT is mounted inside a rectangular acrylic housing facing a clear 144-mm-square front window constructed from ultraviolet transmitting (UVT) acrylic, allowing them to exist inside of the LiLS. Conical reflectors were installed at the face of the housing to improve light collection efficiency in the corners. The housing is filled with optical grade mineral oil and sealed with an O-ring and a 32-mm-thick back plug. For a detailed drawing of the PMT housing module see Figure 3.5. For more information on the PMT housing design and construction see [67].

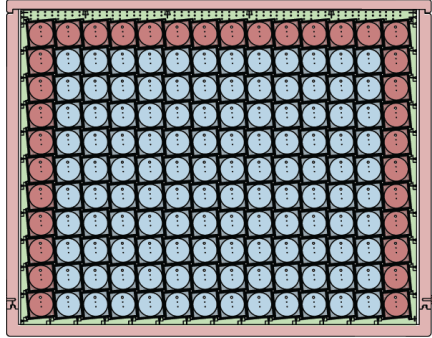


**Figure 3.4:** A cross-section of the inner AD showing 68 ET PMTs (red) in the outer columns and top row and 240 Hamamatsu PMTs (blue) in the remaining segments.

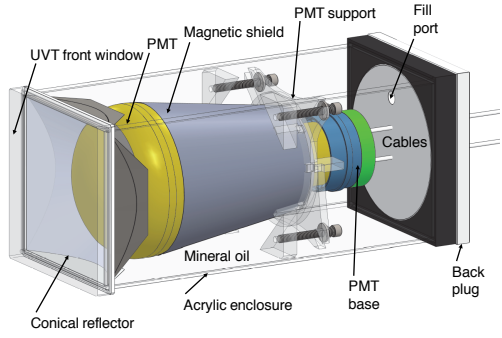


**Figure 3.5:** A PMT housing module.

### 3.2.1.2 Optical Grid

The active volume of the detector, measuring  $2.045\text{ m wide} \times 1.607\text{ m high} \times 1.176\text{ m long}$ , is separated into 154 optically separated long segments with a  $0.145\text{ m} \times 0.145\text{ m}$  square cross-sectional area. The optical grid that creates the individual segments consists of low-mass, highly specularly reflective optical separators held in position by white 3D-printed support rods. The optical separators (reflectors) are composed of a carbon fiber backbone covered on both sides with adhesive-backed DF2000MA specularly reflecting film, an optically clear adhesive film, and a thin surface layer of fluorinated ethylene propylene (FEP) film. Two types of pinwheel shaped support rods were produced and strung on acrylic rods to grip the reflectors and hold them in place and separate the PMT housings from each other. The pinwheels were 3D printed using white-dyed 100-micron polylactic acid (PLA) filament and are pictured in Figure 3.6. For more details on the fabrication of the optical grid see [72].

Each segment contains a PMT housing at each end and four reflectors held in place by pinwheel rods that extend from one PMT to the other, as shown in Figure 3.7. The front windows of the PMT housings protrude  $\sim 1\text{ cm}$  into the optical grid, minimizing cross-talk between segments. Figure 3.8 shows the assembly of the top row of the detector, demonstrating the placement of the housings and optical grid.

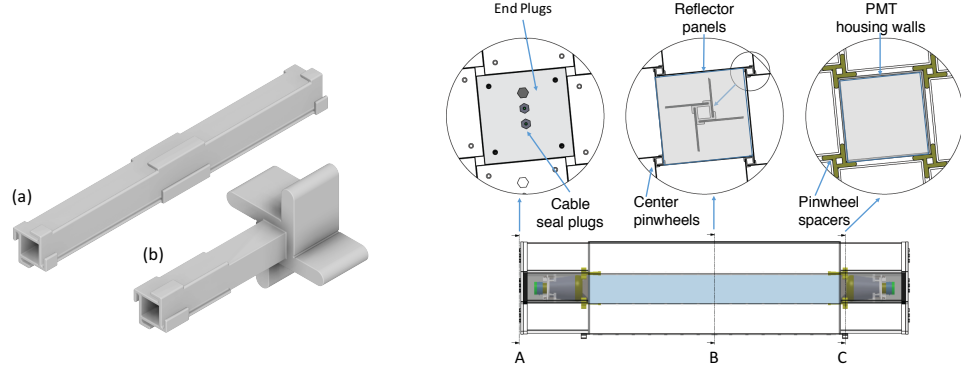


**Figure 3.6:** Representative pinwheel types. (a) Central pinwheel - Three tabs per side hold the optical separator in place. (b) End pinwheel - spacer arms separate the PMT housing bodies and support the pinwheel string.

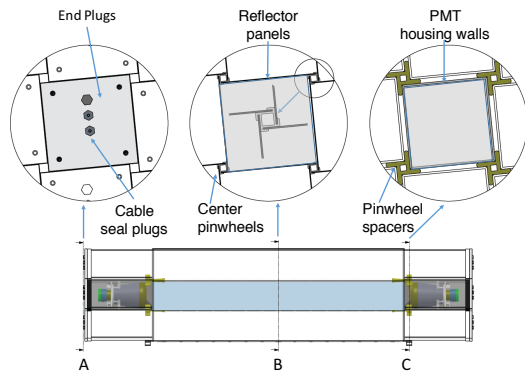


**Figure 3.7:** Three complete segments, including PMT housings at each end with reflectors kept in place between segments by pinwheel rods.



**Figure 3.8:** Assembly of the top row of the PROSPECT AD, demonstrating the placement of the PMT housings and optical grid.

### 3.2.1.3 Segment Supports

While the optical grid creates the inner volume segmentation, acrylic segment supports hold the total volume in place and determine the size of the active volume. A slab of ship-lap style acrylic underneath the bottom row of segments position them at a  $5.5^\circ$  tilt with a 0.146 m pitch. Horizontal planks are screwed onto the backs of the PMT housings and attach together along the sides of the volume, while side walls constrain the outer pinwheel rows. Baffles at the top of the detector tie the four surrounding walls together and keep the top reflector layer in place. The construction of the inner detector, including all segment supports, allows the liquid scintillator to flow around all objects and therefore fill the whole space. For a photograph of the constructed inner detector see Figure 3.9.



**Figure 3.9:** A photograph of the constructed inner detector.

### 3.2.1.4 Radioactive Calibration System

The radioactive calibration system is designed to measure and calibrate the energy and position response of the detector as well as to study topological effects. It does this by moving radioactive sources through a system of tubes routed throughout the active detector, the positions of which are pictured in Figure 3.10. PROSPECT

Source	Decay	$\gamma$ Energy [MeV]	Purpose	Rate
$^{137}\text{Cs}$	$\beta^-$	0.662	segment comparison	$0.1 \mu\text{C}$
$^{22}\text{Na}$	$\beta^+$	$2 \times 0.511, 1.275$	positron, edge effects	$0.1 \mu\text{C}$
$^{60}\text{Co}$	$\beta^-$	1.173, 1.332	energy scale	$0.1 \mu\text{C}$
$^{252}\text{Cf}$	n (fission)	2.223 (n-H capture)	neutron response	866 n/s
AmBe	n	4.4	neutron response	70 n/s

**Table 3.1:** Calibration sources and their properties.

deploys  $^{137}\text{Cs}$ ,  $^{22}\text{Na}$ ,  $^{60}\text{Co}$ ,  $^{252}\text{Cf}$ , and an AmBe source, the features of which are listed in Table 3.1.

Each source is encapsulated in a small aluminum cylinder, about 12 mm long, and then connected to a timing belt as pictured in Figure 3.11. The timing belts are placed in source tubes that run along the length of the segments and are controlled by motors mounted outside of the detector volume. For more information on the construction of the calibration system see Ref.[73].

PROSPECT also makes use of intrinsic radioactive sources for calibration and monitoring of detector characteristics. Two of these are colloquially known as “BiPo” decays, and they arise from the  $^{212}\text{Bi} \rightarrow ^{212}\text{Po} + \beta \rightarrow ^{208}\text{Pb} + \alpha$  and  $^{214}\text{Bi} \rightarrow ^{214}\text{Po} + \beta \rightarrow ^{210}\text{Pb} + \alpha$  decay chains which stem from naturally occurring  $^{232}\text{Th}$  ( $t_{1/2} = 14$  Gyr) and  $^{238}\text{U}$  ( $t_{1/2} = 4.5$  Gyr), respectively. Along with these, a chloride solution of  $^{227}\text{Ac}$  was dissolved in the liquid scintillator to provide a source of “RnPo” decays from the chain  $^{219}\text{Rn} \rightarrow ^{215}\text{Po} + \alpha \rightarrow ^{211}\text{Pb} + \alpha$ . Further details on the motivation and results from adding actinium will be discussed in Chapter 5.

### 3.2.1.5 Liquid Scintillator

The liquid scintillator (LS) used in PROSPECT needed to accomplish two goals: (i) provide very good pulse shape discrimination (PSD) for sufficient background rejection of fast neutrons and ambient gammas and (ii) have high light yield in order to obtain good energy and timing resolution. The LS also needed to remain stable over time and was required to be non-flammable according to facility requirements. In order to accomplish these tasks PROSPECT developed a novel lithium-doped liquid scintillator (LiLS).  $^6\text{Li}$  was chosen as the doping agent due to its high neutron capture cross section, which produces an  $\alpha$  and a  $^3\text{H}$  a Q-value of 4.78 MeV, quenched to  $\sim 540$

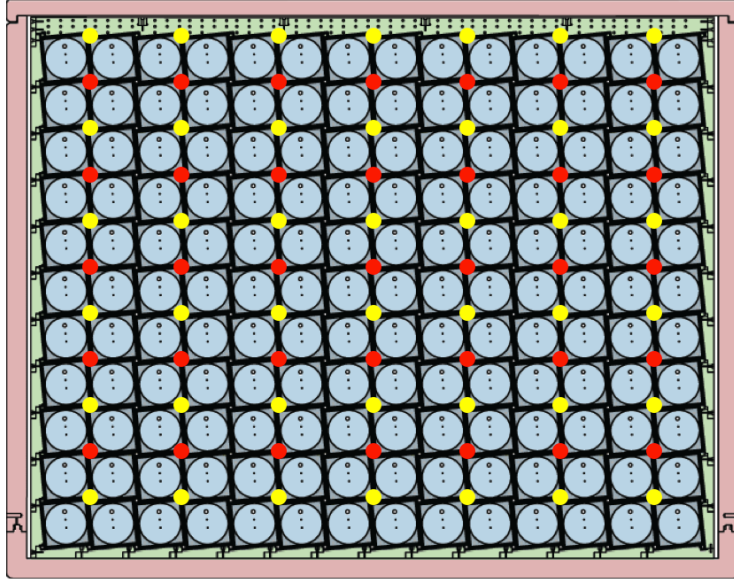


**Figure 3.10:** Location of the source tubes (red) routed through the active detector volume.

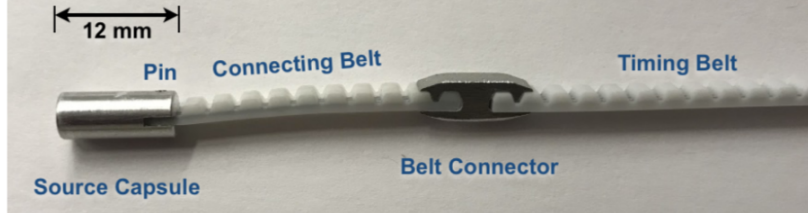


**Figure 3.11:** An example of a source capsule attached to the timing belt.

keV of visible energy in the scintillator. These particles are also spatially localized, which is necessary for the compact detector size of PROSPECT.

The LiLS was created by adding a surfactant to the base LS which allowed the addition of a  $^{6}\text{LiCl}$  solution to obtain a final doping of  $(0.082\pm 0.001)\%$  by mass. The combination of the surfactant and chloride solution forms a thermodynamically stable micro emulsion, ensuring material uniformity and allowing the addition of an actinide chloride solution ( $^{227}\text{Ac}$ ). A total of 5,040 liters were produced and stored in 28 separate drums. One drum was doped with a  $^{227}\text{Ac}$  chloride solution. For more information on the fabrication of the LiLS see Ref.[74].

Prior to filling the detector, all drums of LiLS were pumped into an ISO tank storage container. Nitrogen was then bubbled through the liquid for ten days to

sufficiently mix together the solution. Samples were taken from each barrel and from the mixed solution in the ISO tank with a Shimadzu UV-Vis spectrometer, the results of which can be seen in Figure 3.12. 4841 kg of LiLS was pumped into the ISO tank and a total of 4340 kg was then added to the detector. For more information on the process of filling the detector with the LiLS see Ref.[67].

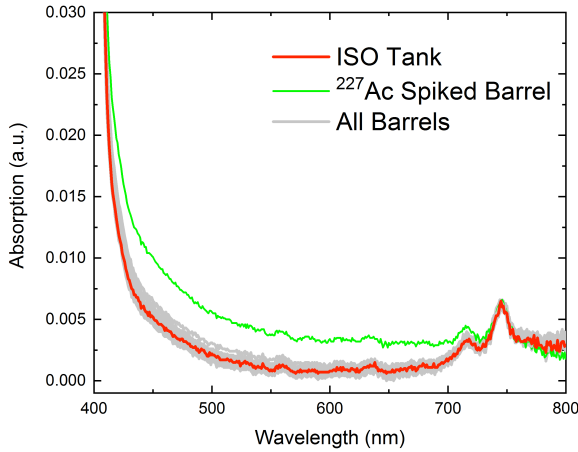


**Figure 3.12:** UV-Vis absorption spectra of the 28 drums of LiLS (gray+green) added to the ISO tank. The only outlier is the  $^{227}\text{Ac}$  spiked barrel (green). The mixed sample (red) falls within the average of all individual barrels. [67]

### 3.2.2 Containment Vessels and Shielding

The inner primary containment vessel is made of acrylic and holds all active detector components described in Section 3.2.1. The acrylic tank was built as three separate parts, the base, vertical walls, and lid. The inner detector was assembled on the acrylic base. After its construction the vertical walls were lowered onto the base and secured with a Viton seal at the base.

The secondary containment vessel was made of aluminum and the top was sealed in order to control the gas environment around the detector. The space between the aluminum and acrylic tanks was filled with sheets of borated polyethylene and demineralized water for absorption of thermal neutrons.

A lead layer of  $0.025\text{ m} \times 0.10\text{ m} \times 0.30\text{ m}$  interlocking bricks was stacked around the perimeter of the aluminum tank. Rows of  $0.10\text{ m} \times 0.10\text{ m}$  recycled polyethylene

lumber were stacked on each other log cabin style around the lead layer. Polyethylene lumber was also used to create roof beams on top of the log cabin walls. The entire surface was then covered with a 0.025 m thick layer of borated polyethylene and thin aluminum sheets. To complete the passive shielding an array of water bricks was added to the top of the assembly. For a schematic of the entire construction see Figure 3.3.

### 3.3 Data Acquisition System

In order to perform pulse discrimination analysis of LiLS signals PROSPECT uses commercial Waveform Digitizer Modules (WFDs). A total of twenty-one CAEN V1725 WFD modules, operated in two Weiner 6023VME crates, are used to readout the 308 PMTs. Readout and control of the WFD modules is performed by two individual PCs, which are run by a control PC. A single Phillips Scientific 757D NIM Fan-In/Fan-Out module operated in a NIM bin is used for trigger signal distribution. A diagram of this system can be seen in Figure 3.13.

Acquisition of waveforms 148 samples long by all WFD channels is triggered if both PMTs in any segment exceed a signal level of 50 ADC counts above baseline ( $\sim 100$  keV) within a 64 ns coincidence window. Acquired samples from each WFD are only recorded to disk if they exceed a threshold limit of 20 ADC counts above baseline ( $\sim 40$  keV). These are labeled the segment and Zero Length Encoding (ZLE) thresholds and allow the acceptance of low energy events while maintaining a manageable data volume. For more information of the data acquisition system and data rates see [67].

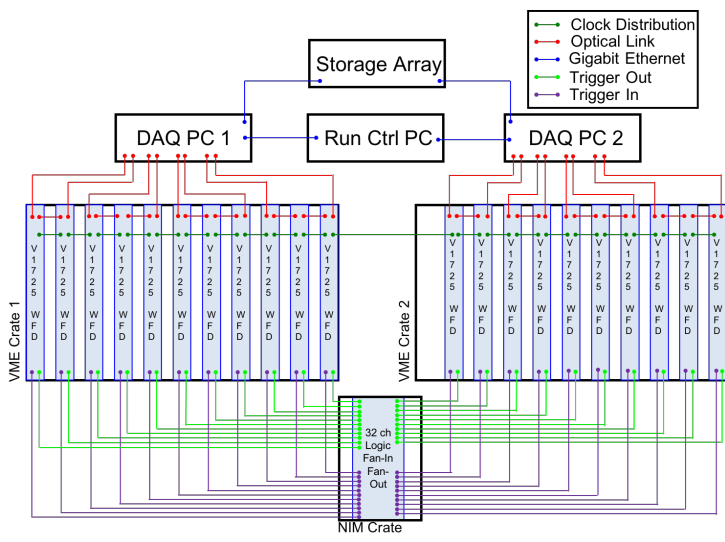


**Figure 3.13:** Diagram of the data acquisition system.

# CHAPTER 4

## PROSPECT ANALYSIS FRAMEWORK AND CALIBRATION

Events in the PROSPECT detector begin as bursts of scintillation in the liquid scintillator. In order to transform these events of light into physics data several steps have to be taken, including position reconstruction and energy calibration. This chapter will outline how these processes are performed, but before that is done a key component of the PROSPECT analysis, pulse shape discrimination, must be presented.

### 4.1 Pulse Shape Discrimination

Physics events in the PROSPECT detector, such as neutron captures on  ${}^6\text{Li}$ , produce scintillation light through ionization that is transported by way of the reflecting panels to individual PMTs. As described in Section 3.3, these signals are processed by CAEN waveform digitizers and are only accepted if they pass the segment and ZLE thresholds. Due to the nature of the liquid scintillator the shape of the digitized waveforms is defined by the ionization density of a given event. Lower ionization density events, such as electrons, have a faster scintillator decay time causing less light in the “tail” of the waveform compared to higher density events like proton recoils, as seen in Figure 4.1.

This allows the definition of a pulse shape discrimination (PSD) factor as the ratio

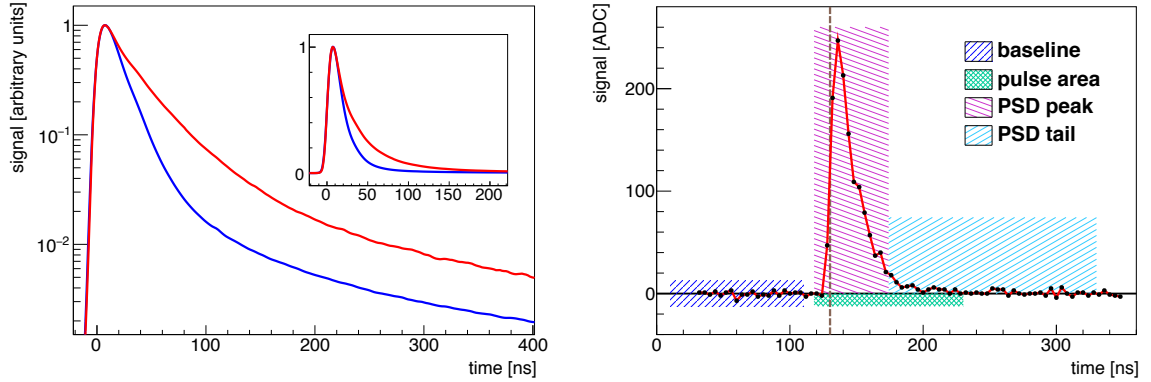


**Figure 4.1:** (Left) Averaged waveforms from electrons (lower, blue) and proton recoils (upper, red) [75]. The inset panel shows the same waveforms on a linear y axis. (Right) Example analysis of a typical pulse [76]. The half-height leading edge timing (dashed vertical) determines windows for baseline subtraction, pulse area, and PSD.

of the signal in the tail versus the total waveform,

$$PSD = \frac{\int_{tail:start}^{tail:end} Qdt}{\int_{-\infty}^{\infty} Qdt} \quad (4.1)$$

The tail area of a given waveform is defined as the window 44 - 100 ns after the time of the half-height leading edge. The total area is defined as the window -12 - 100 ns relative to the same leading edge time. An example of these windows on a typical pulse can be seen in Figure 4.1. Use of the PSD parameter, along with energy, provides clear separation between neutron captures on <sup>6</sup>Li and other event classes such as electron recoils. An example of this for a single segment can be seen in Figure 4.2, where a pseudo-energy is calculated using the integrated pulse area of each PMT, S<sub>0</sub> and S<sub>1</sub>.

## 4.2 Data Processing and Calibration

For simplicity consider one event contained in one segment. Both PMTs in the segment will collect photons from this event that are saved as individual waveforms. These are analyzed and information such as pulse area and height in analog-to-digital converter (ADC) units, PSD, and arrival time are saved. The next step involves combining information from both PMTs, calibrating the energy, and reconstructing the position.

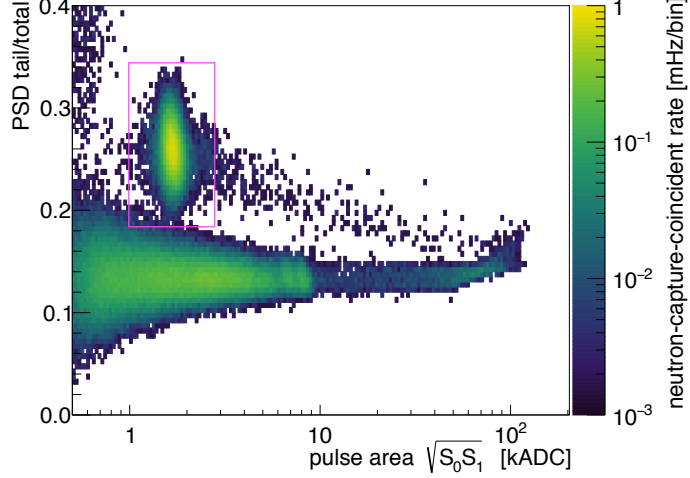


**Figure 4.2:** PSD vs. pseudo-energy for neutron capture coincident events in a single segment [77]. The neutron captures, outlined by the magenta rectangle, are clearly separated in PSD from electron-like events in the lower band.

#### 4.2.1 Timing to Position Curves

Through-going muons provide a large and consistent data set which can be used to reconstruct positions based on timing. As muons travel through the pinwheel rod tabs the light transport is distorted in timing and magnitude. This creates a striping effect in the timing between the two PMTs,  $dt$ , versus the signal amplitude ( $S_0 + S_1$ ) distribution as shown in Figure 4.3.

The striping becomes even clearer when plotting  $dt$  for events with signal amplitudes in the range  $1e4 - 2e4$  ADC for a single segment as shown in Figure 4.4. For each segment this distribution is first fit with an “M”-shaped curve,  $M(dt)$ . Then, the residual structure is fit to a sinusoidal curve with a slowly varying phase shift term,

$$n(dt) = M(dt) \left[ 1 + k \cos \left( \frac{2\pi}{\delta} (a dt + b dt^3) \right) \right] \quad (4.2)$$

where  $\delta = 78.5$  mm is the average spacing between pinwheel tabs, and  $k, a, b$  are fit parameters. The inner phase term provides the position calibration  $z(dt) = a dt + b dt^3$ , whose resulting curves are shown in Figure 4.5.

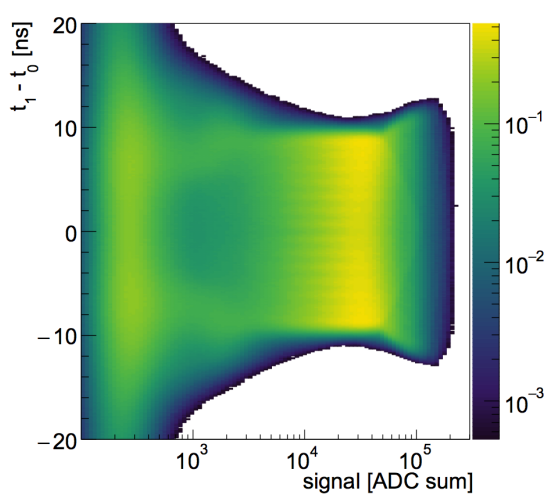


**Figure 4.3:**  $dt$  versus signal amplitude for through-going cosmogenic muons [78]. Striping is visible at time intervals corresponding to pinwheel placement.

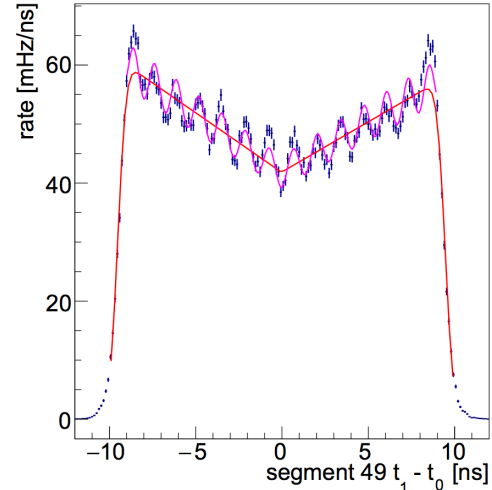


**Figure 4.4:**  $dt$  of through-going muons in a single segment for events with signal amplitudes in the range  $1e4 - 2e4$  ADC [78]. Data (blue points) are fit with an “M”-shaped curve (red) and a sinusoidal curve (magenta).

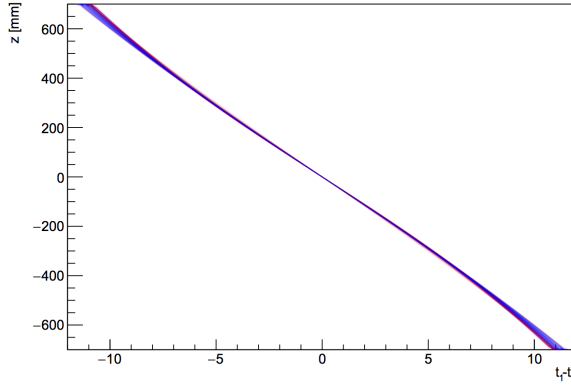


**Figure 4.5:**  $z(dt)$  curves for all cells, extracted from fitting muon  $dt$  distributions [78].  
Blue: Hamamatsu segments, red: ET segments.

### 4.2.2 Energy Calibration

The energy of an event is first defined as the sum of the integral of the waveforms from both segment PMTs in ADC units. The next step involves converting to energy units of MeV and correcting for longitudinal light collection variation. These procedures are performed using neutron captures on  ${}^6\text{Li}$  ( $n\text{Li}$ ) because they are well understood and always peak at a quenched energy of around 0.53 MeV electron equivalent (MeVee).

After combining the waveforms for all events, the neutron captures at the center of the segment are calibrated to 0.526 MeVee, defining the energy scale for all segments and all classes of events. Constraining the energy scale in this way creates a quadratic dependence of energy on position, as seen in the left panel of Figure 4.6. This is corrected for by calibrating a gain factor for each PMT using two metrics. The first is the neutron capture signal at cell center,  $S = \sqrt{S_0 S_1}$ , which is found by fitting the distribution in the left panel of Figure 4.6 with a quadratic polynomial. The second is the light ratio,  $R = S_1/S_0$ , at cell center which is found by fitting the distribution in the right panel of Figure 4.6 with a cubic polynomial. The gain factors for both PMTs are then defined as,

$$g_0 = \frac{S}{\sqrt{R} E_n} \quad g_1 = \frac{S \sqrt{R}}{E_n} \quad (4.3)$$

where  $E_n$  is the energy of the neutron capture peak.

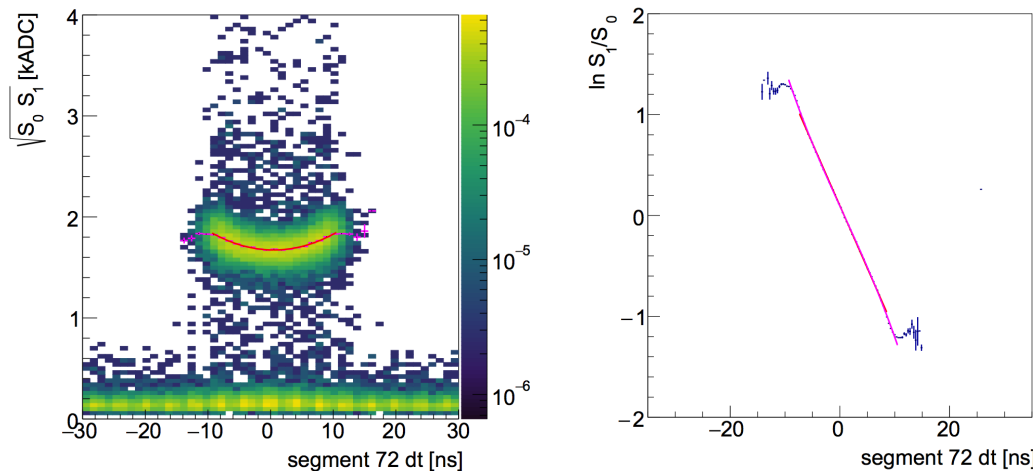


**Figure 4.6:** (Left) Neutron capture events in one segment versus  $dt$ , with a quadratic fit in red. (Right) The  $\ln$  signal ratio versus  $dt$  for muon events in one segment, with a cubic polynomial fit in magenta.

## 4.3 Monte Carlo Simulation

Due to the geometry of the PROSPECT detector and properties of the scintillator, reconstructed events are highly position and energy dependent. In order to perform an oscillation analysis it is important to understand the detector response to incoming antineutrino events. This is done by modeling the detector, including all material and scintillator properties, in a GEANT-4 based simulation package hereto referred to as PROSPECT-G4 (PG4). Monte Carlo (MC) simulations with PG4 generate a position-dependent energy response that is used to interpret real physics data. This can only be done if PG4 behaves the same way that the PROSPECT detector does. This is ensured by tuning values in PG4 to reproduce distributions measured by a variety of radioactive calibration sources and intrinsic background energy depositions.

### 4.3.1 Nonlinearity

The nonlinearity of the scintillator response at low energies is parameterized in PG4 using a combination of Birks' quenching model [79] and a Cherenkov radiation model. Birks' law defines the light yield per path length as a function of the energy loss per path length for a particle traveling through scintillator and at each simulation step  $i$  is applied using

$$\frac{dE_{scint}}{dx} = \frac{\frac{dE}{dx}}{1 + k_{B1} \frac{dE}{dx} + k_{B2} \left( \frac{dE}{dx} \right)^2} \quad (4.4)$$

where  $k_{B1}$  and  $k_{B2}$  are the Birks' constants which depend on the material and  $dE/dx$  is the true deposited energy.

Particles traveling faster than the speed of light in the scintillator can emit Cherenkov radiation, therefore, the number of Cherenkov photons,  $N$ , generated at each simulation step is calculated as

$$\frac{d^2N}{dxd\lambda} = \frac{2\pi\alpha z^2}{\lambda} \left( 1 - \frac{1}{\beta^2 n^2(\lambda)} \right) \quad (4.5)$$

where  $\alpha$  is the fine structure constant,  $z$  is the particle's electric charge,  $\beta$  is the speed of the particle, and  $n(\lambda)$  is the index of refraction. The energy emitted from the Cherenkov radiation is then calculated as the summed energy of detected Cherenkov

photons,

$$E_c = k_c \sum_{\lambda} N_{\lambda} E_{\lambda} \quad (4.6)$$

where  $k_c$  is the efficiency of detecting Cherenkov light. Comparison between data and MC allows the tuning of both Birks' constants,  $k_{B1}$  and  $k_{B2}$ , and  $k_c$ .

### 4.3.2 Energy Response

Reconstructed energy distributions,  $E_{rec}$ , are measured using a variety of calibration sources placed at z-center positions in the detector. Similar distributions can also be created through MC simulations by setting values for  $k_{B1}$  and  $k_{B2}$ , and  $k_c$  as well as an absolute energy scale factor,  $A$ . A comparison between the data and MC allows for the tuning of these values until good agreement is shown between the two sets of distributions.

For these studies three  $\gamma$ -ray sources were used,  $^{60}\text{Co}$ ,  $^{137}\text{Cs}$ , and  $^{22}\text{Na}$ , along with  $\gamma$ 's resulting from neutron-Hydrogen captures using  $^{252}\text{Cf}$  as the neutron source ( $\gamma$  energies listed in Table 3.1). The spectrum of  $^{12}\text{B}$  was also measured because its  $\beta$  dominated energy distribution (3 MeV to 13.6 MeV) covers a similar energy range as IBD events. As well as comparing the energy spectra,  $^{137}\text{Cs}$  and  $^{22}\text{Na}$  are used to compare event multiplicity between MC and data. The results of these comparisons can be seen in Figure 4.7, where good agreement is seen between MC and data. The best-fit parameters determined by these studies are  $(A, k_{B1}, k_{B2}, k_c) = (1.0026 \pm 0.004, 0.132 \pm 0.004 \text{ MeV/cm}, 0.023 \pm 0.004 \text{ MeV/cm}, 37 \pm 2\%)$ , with a  $\chi^2/\text{ndf}$  of 581.5/420.

Further agreement can be seen when comparing the peak locations for all  $\gamma$ -ray sources as seen in Figure 4.8. The ratio between data and MC is shown to be within  $\pm 1\%$  for all sources for three different time periods.

### 4.3.3 Energy Resolution

A comparison of MC and data energy distributions of the  $\gamma$ -ray sources can also be used to define an energy resolution function. MC simulated energy distributions are smeared according to Gaussian distributions until they match data. The resolution of the smeared distributions is then compared to the true deposited energy and fit

with the function

$$\frac{\sigma_E}{E_{rec}} = \sqrt{a^2 + \frac{b^2}{E_{rec}} + \frac{c^2}{E_{rec}^2}} \quad (4.7)$$

where  $a$ ,  $b$ , and  $c$  are dependent on detector geometry, photostatistics (PE/MeV), and PMT quantum efficiency respectively. The results of this can be seen in Figure 4.9, where the parameters are found to be  $(a, b, c) = (1.15\% \pm 0.47\%, 4.61\% \pm 0.24\%, 0 \pm 1.3\%)$ , resulting in an energy resolution at 1 MeV of  $4.76\% \pm 0.2\%$ .

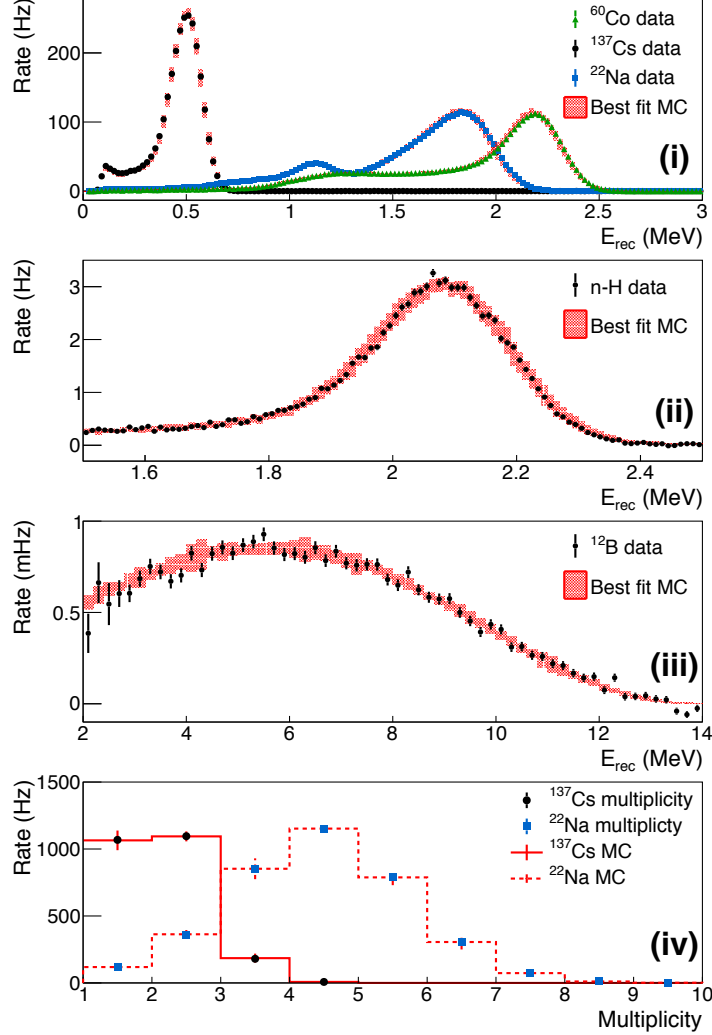


**Figure 4.7:** Reconstructed energy distributions for calibration data and PG4 Monte Carlo simulations [80]. (i):  $E_{rec}$  for  $\gamma$ -ray source deployments; (ii):  $E_{rec}$  for n-H captures from a  $^{252}\text{Cf}$  source deployment; (iii):  $E_{rec}$  for cosmogenically produced  $^{12}\text{B}$ ; (iv): pulse multiplicity for  $^{137}\text{Cs}$  and  $^{22}\text{Na}$  source deployments. Error bands indicate statistical (data) and systematic (PG4) uncertainties.

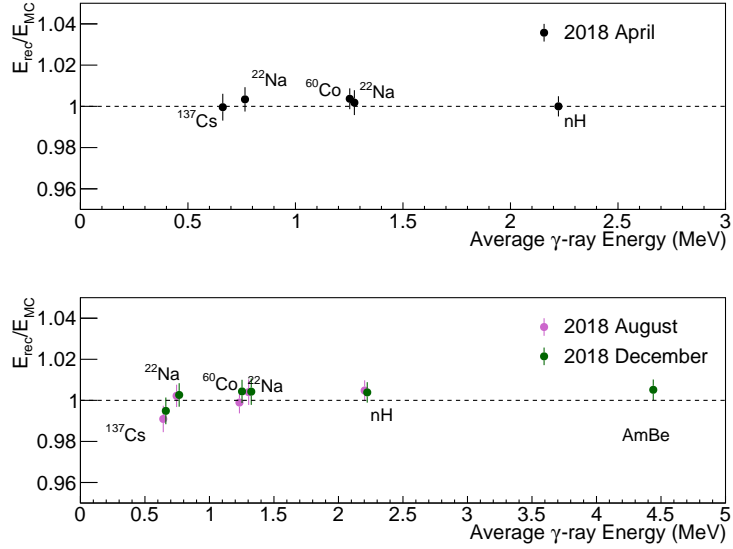


**Figure 4.8:** Ratio of data versus PG4 Monte Carlo simulation energy peak locations of the given  $\gamma$  sources, plotted versus true gamma energy for three different time periods [80]. Error bands indicate statistical and systematic uncertainties. Ratios for all datasets are within  $\sim 1\%$  of unity, indicating accurate energy response modeling in PG4 for a wide energy range.

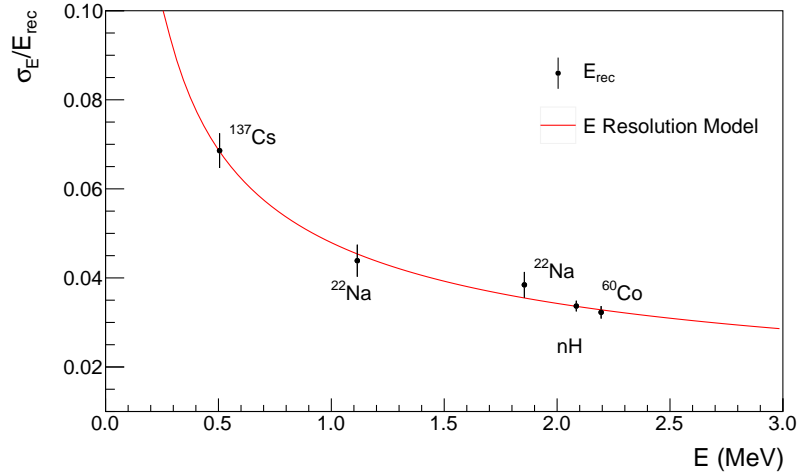


**Figure 4.9:** Energy resolution of PG4 Monte Carlo simulation distributions matched to data versus true gamma energy for the given calibration sources fit with the function in Eq. 4.7 [80]. Error bands indicate statistical and systematic uncertainties.

# CHAPTER 5

## $^{227}\text{AC}$ AS A CALIBRATION SOURCE

### 5.1 Motivation

In the absence of an eV-scale sterile neutrino PROSPECT should measure IBD rates that fall like one over distance from the reactor squared. If sterile neutrino oscillation was detected, after one year PROSPECT would measure the spectrum seen in Figure 5.1, given a mass splitting of  $1.78 \text{ eV}^2$ , . However, a situation could occur in which a sterile neutrino did not exist, or could not be measured with PROSPECT, and an oscillation is still measured. This could happen if there are segment to segment volume variations throughout the detector, mimicking an oscillation signal. Therefore, it becomes important that the product of efficiency  $\times$  volume for all segments is well known.

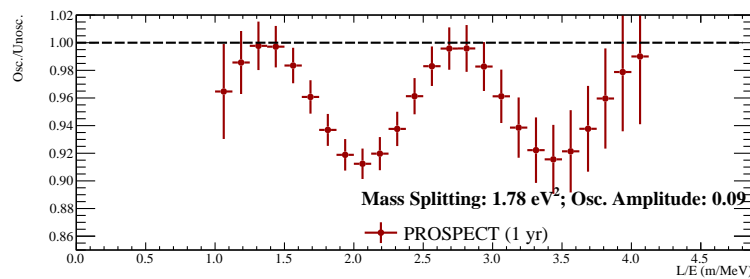


**Figure 5.1:** The ratio of the oscillated to un-oscillated neutrino spectrum as a function of  $L/E$  that would be observed by PROSPECT after 1 year if a sterile neutrino signal was detected [81].

This measurement can be accomplished if an event source is uniformly distributed throughout the active volume of the detector. By measuring the rate of this source in each segment the relative volumes can be compared and tracked through time.  $^{227}\text{Ac}$  was chosen as the source and a chloride solution was prepared and dissolved in the liquid scintillator to ensure uniform distribution.

$^{227}\text{Ac}$  was chosen for several reasons. First, because an  $\alpha$ ,  $\alpha$  coincidence occurs in its decay chain, specifically  $^{219}\text{Rn} \rightarrow ^{215}\text{Po} + \alpha \rightarrow ^{211}\text{Pb} + \alpha$ , as highlighted in Figure 5.2.  $^{219}\text{Rn}$  has a half-life of  $3.96 \pm 0.01$  s and  $\alpha$ -decays 100% of the time, while  $^{215}\text{Po}$  has a half-life of  $1.781 \pm 0.005$  ms and  $\alpha$ -decays 99.99977(2)% of the time [82], so the  $\alpha$ ,  $\alpha$  coincidences happen frequently. The  $\alpha$  decay of  $^{215}\text{Po}$  is mono-energetic at 7.39 MeV which results in a  $\sim 0.78$  MeV signal after quenching, well removed from nLi captures that occur around 0.5 MeVee. In addition, there are no corresponding gammas with the  $^{215}\text{Po}$  decay, making this a very clean and well defined signal. The  $^{219}\text{Rn}$   $\alpha$  decays are not so nice, as there are four dominant alpha energies and three dominant gamma energies for these decays, as listed in Table 5.1, but the use of time, energy, and PSD cuts make them easy to pair with corresponding  $^{215}\text{Po}$  decays.

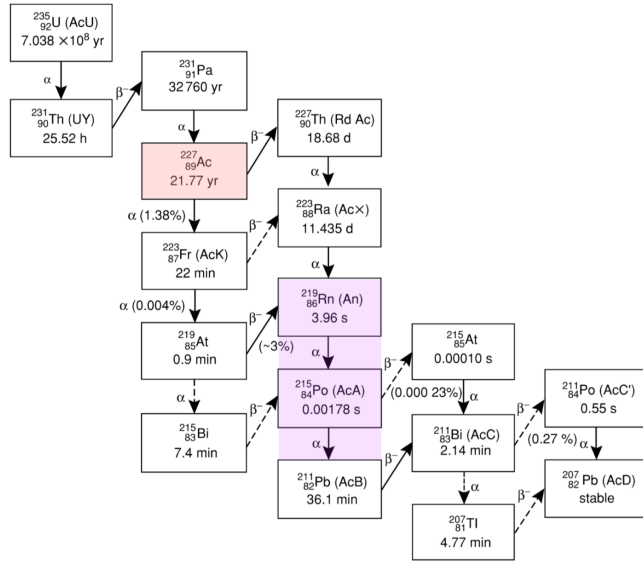


**Figure 5.2:** The full decay chain of  $^{227}\text{Ac}$  (a daughter of  $^{235}\text{U}$ ), in which the  $\alpha$ ,  $\alpha$  coincidence of interest is highlighted [83].

	$E_\alpha$ [keV]	$I_\alpha$ %	$E_\gamma$ [keV]	$I_\gamma$ %
$^{219}\text{Rn}$	6425.0(10)	7.5(6)	271.23(1)	10.8(6)
	6530(2)	0.110(10)	401.81(1)	6.6(4)
	6552.6(10)	12.9(6)	130.60(3)	0.13(9)
	6819.1(3)	79.4(10)		
$^{215}\text{Po}$	7386.1(8)	99.999770(20)		

**Table 5.1:** Energy and absolute intensity of dominant  $\alpha$  and  $\gamma$  decay radiation for  $^{219}\text{Rn}$  and  $^{215}\text{Po}$ . Decay energies not listed here have an intensity of  $<0.05\%$ .

## 5.2 Material Compatibility

Before  $^{227}\text{Ac}$  could be added to the PROSPECT detector, it had to be determined that  $^{227}\text{Ac}$  and its daughters would not adsorb onto detector materials. If it was adsorbed then it would not be a uniform source in the detector, nullifying its use as a method to track relative efficiency  $\times$  volume throughout the detector. To test this six material samples were placed in vials of  $^6\text{Li-LS}$  spiked with  $^{227}\text{Ac}$ . The rate of  $^{227}\text{Ac}$  in each sample vial and one reference vial with no material was measured and tracked over a period of 6 months. An observation of a significant decrease in rate, relative to the half-life of  $^{227}\text{Ac}$ , would indicate that  $^{227}\text{Ac}$  was adsorbing onto the material.

### 5.2.1 Material and Scintillator Preparation

The materials tested were: ultraviolet transmitting (UVT) acrylic, flourinated ethylene propylene (FEP), polylactide (PLA), polyether ether ketone (PEEK), a RG 188 cable, and viton o-rings. See Table 5.2 for a list of their uses in the detector and sample sizes. To prepare the materials they were all placed in a single beaker with ultra-pure water and cleaned ultrasonically for 30 minutes. They were then transferred to a watch glass and placed in a 50 C oven for two hours. After drying they were placed in empty 12 mL vials.

The  $^{227}\text{Ac}$  used to spike the scintillator was obtained from Eckert and Ziegler as a solution of  $3.711 \times 10^4$  Bq  $\pm 1.32\%$  of  $^{227}\text{Ac}$  in 10.22710 g of 1 M HCl, measured on September 6, 2016. 0.503 g of this solution was added to 192 g of  $^6\text{Li-LS}$  on December 15, 2016. With a half-life of  $21.772 \pm 0.003$  yrs [82], the activity of the  $^{227}\text{Ac}$  solution before adding to the LiLS was 36788 Bq, yielding a final activity of 94.2 Bq/10 g.

This is the stock solution from which all LS was taken for the material studies and later on for spiking the detector.

Material	Detector Use	Sample Size
UVT Acrylic	Front window of PMT housing	$1.0 \times 1.15 \times 0.1 \text{ cm}^3$
FEP	Film on optical separators	$1.5 \times 1.5 \text{ cm}^2$ , 3 mm thick
PLA	3D printed pinwheels	10 disks; 0.5 cm diameter, 0.1 cm thick
PEEK	Seal plugs through which the high voltage and signal cables were threaded. Screws used to bolt together segment supports. Spacers at the base of the acrylic tank.	1 Nut; ID 0.5 cm, small OD 1cm, large OD 1.1cm, thickness 0.5 cm
RG188 Cable	High voltage and signal cables	4.5" long
Viton O-ring	Seal back plugs of PMT housings and seal acrylic tank	10 O-rings; OD 6mm, ID 3mm, thickness 1.5mm

**Table 5.2:** Samples used to test if  $^{227}\text{Ac}$  or its daughters would adsorb onto detector materials.

Material	Date Filled	Weight of LiLS Added (g)
Reference	12/15/2016	10.030
UVT Acrylic		9.98
FEP		9.98
PLA		9.999
PEEK	02/24/2017	9.99
RG188 Cable		9.981
Viton O-ring		10.011

**Table 5.3:** The weight of  $^{227}\text{Ac}$  spiked LiLS that was added to each sample vial.

Prior to filling all sample vials the threads of each vial were wrapped with teflon tape in an effort to obtain a secure seal. The reference vial was filled on December 15, 2016 with 10.030 g of  $^{227}\text{Ac}$  spiked LiLS from the stock solution, yielding an expected activity of 94.5 Bq. All material vials were filled on February 24, 2017 with the amount of stock solution added to each listed in Table 5.3. At the time of filling the

rate in each vial was expected to be  $\sim 93$  Bq. For a photograph of all filled material sample vials see Figure 5.3.

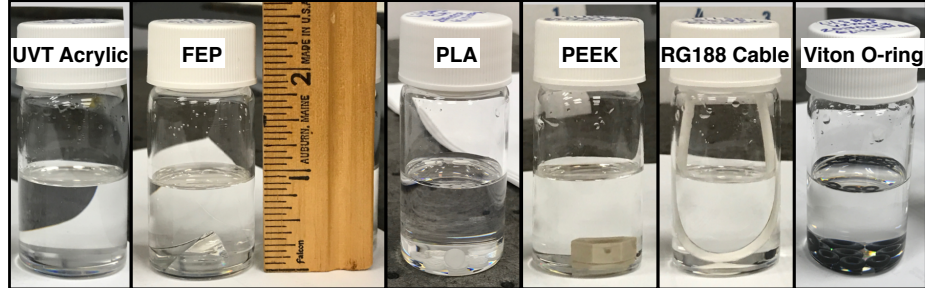


**Figure 5.3:** Photos of all material sample vials filled with  $^{227}\text{Ac}$  spiked LiLS, with ruler for scale.

### 5.2.2 Detector

The detector consisted of a 2" photomultiplier tube coupled using optical grease to a solid cylinder of UVT acrylic painted white with an insert cut out to hold the sample vials, as shown in Figure 5.4. Placed in a dark box the PMT is cabled to a CAEN DT55xx Desktop HV Power Supply and a CAEN DT5730 8 Channel 14-bit 500 MS/s Digitizer [84]. A modified version of Wavedump 3.7.2 [85] was used to start and stop the data runs and save the waveforms of the signals.

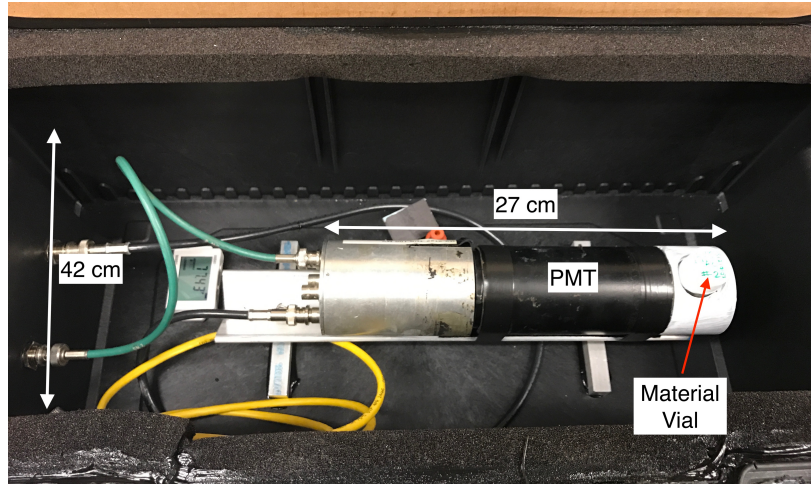


**Figure 5.4:** Detector used for material studies, consisting of a 2" PMT coupled to an acrylic cylinder holding the sample vials, all contained in a dark box. The PMT is cabled to a power supply and digitizer that exist outside of the box.

### 5.2.3 Data Analysis

The raw waveforms are analyzed to calculate the energy and PSD of each signal. Each collected waveform consists of 250 2 ns samples. The energy is measured by taking the integral of the waveform using the trapezoidal rule in ADC units. The total energy is converted to nC using

$$E[nC] = E[ADC] \times \frac{1 \times 10^9}{R \times \text{sample-rate} \times n[ADC/V]} \quad (5.1)$$

where  $R$ , the resistance, is  $50 \Omega$ , the sample-rate is  $5 \times 10^8$  Hz, and  $n = (2^{14} - 1)/2 = 8191.50$  ADC/V. The tail and total fractions used to calculate the PSD are both measured from the leading half-maximum point. The total is measured as the integral from 10 samples before the half-max to 140 samples after. The tail is measured as the integral from 19 samples after the half-max to 140 samples after.

The  $^{227}\text{Ac}$  coincident alpha events, labeled RnPo events for the remainder of this document, are found by applying a set of timing, energy, and PSD cuts along with an accidental background subtraction. Po events are found first by applying the energy and PSD cuts listed in Tabel 5.4. Rn coincidental events are found by looking in a 12.85 ms time window before a given Po event and applying the same energy and PSD cuts. This time window is 5 times the lifetime of Po, 2.57 ms, allowing the collection of all possible coincident events. Accidental events are found by looking in the same length time window, using the same energy and PSD cuts, but offset 10 Po lifetimes before a given Po event. RnPo events are then found by subtracting the accidental events from the coincident events. See Figure 5.5 for an example of typical energy and PSD distributions.

Energy	$0.01 < E < 0.055 \text{ nC}$
PSD	$0.31 < \text{PSD} < 1.0$
$\Delta t = t_{\text{delay}} - t_{\text{prompt}}$	$\Delta t < 5\tau_{\text{Po}}$

**Table 5.4:** Energy, PSD, and time cuts used to find RnPo events where  $\tau_{\text{Po}} = 2.57$  ms. Energy and PSD cuts are applied to both prompt and delay events.

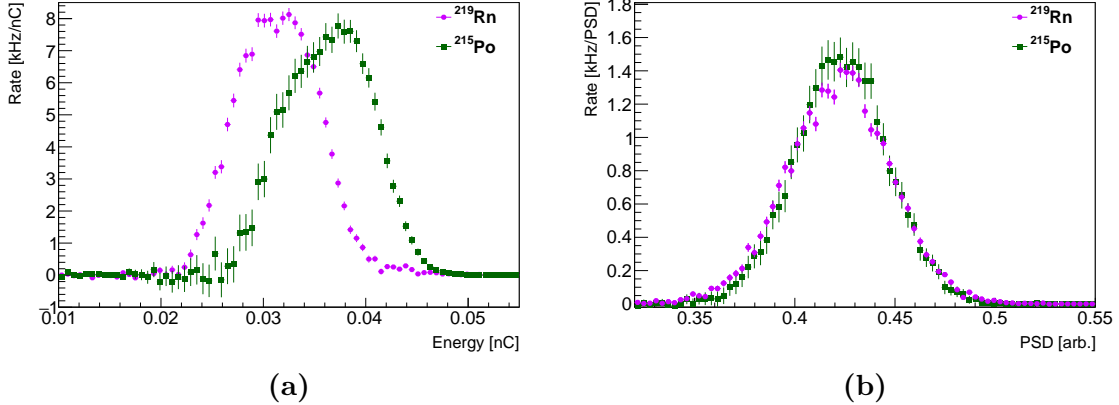


**Figure 5.5:** Typical energy (a) and PSD (b) distributions for RnPo events in the reference sample after accidental background subtraction.

The rate of RnPo events is measured by fitting the RnPo  $\Delta t$  distribution with

$$f(t) = N_0 e^{-t/\tau} \quad (5.2)$$

where  $N_0$  and  $\tau$ , the lifetime of  $^{215}\text{Po}$ , are allowed to vary. Using the fit results, the rate is then defined as

$$R = \frac{N_0 \tau}{\text{bin-width} \times \text{livetime}} \quad (5.3)$$

$$\sigma_R = R \times \sqrt{\left(\frac{\sigma_{N_0}}{N_0}\right)^2 + \left(\frac{\sigma_\tau}{\tau}\right)^2 + \frac{2\sigma_{N_0}\tau}{N_0\tau}} \quad (5.4)$$

where the livetime is measured, for each run, as the time from the beginning of the run to the last Po event. An example of a typical RnPo  $\Delta t$  distribution can be seen in Figure 5.6. It should be noted here that the energy and PSD cuts were made wide enough so that no efficiency correction needed to be applied.

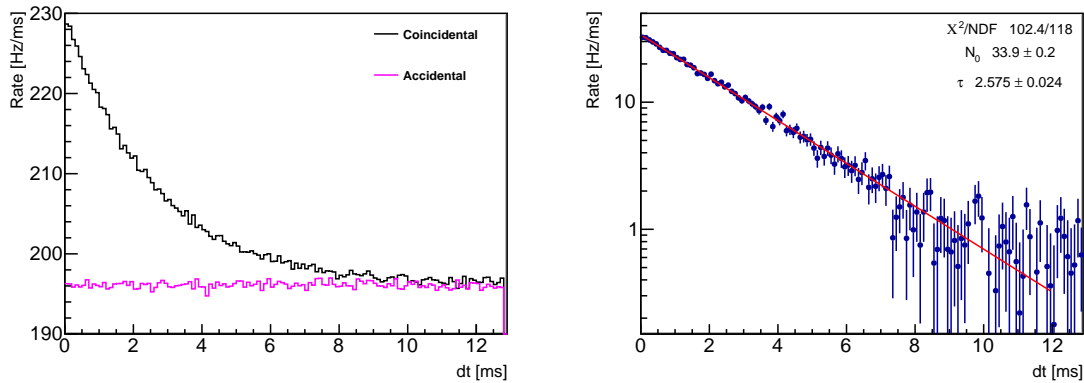


**Figure 5.6:** A typical example of the RnPo  $\Delta t$  distributions for the reference sample. Left: coincidental and accidental distributions found using the defined energy and PSD cuts. Right: the  $\Delta t$  distribution after subtraction of the accidental distribution, fit with Equation 5.2.

## 5.2.4 Results

The RnPo rate was calculated for each material sample and the reference sample over a period of about six months. These results can be seen in Figure 5.7. Though statistical errors vary from around 0.6-1%, overall rates vary at a rate of around 12%, indicating systematic variations.

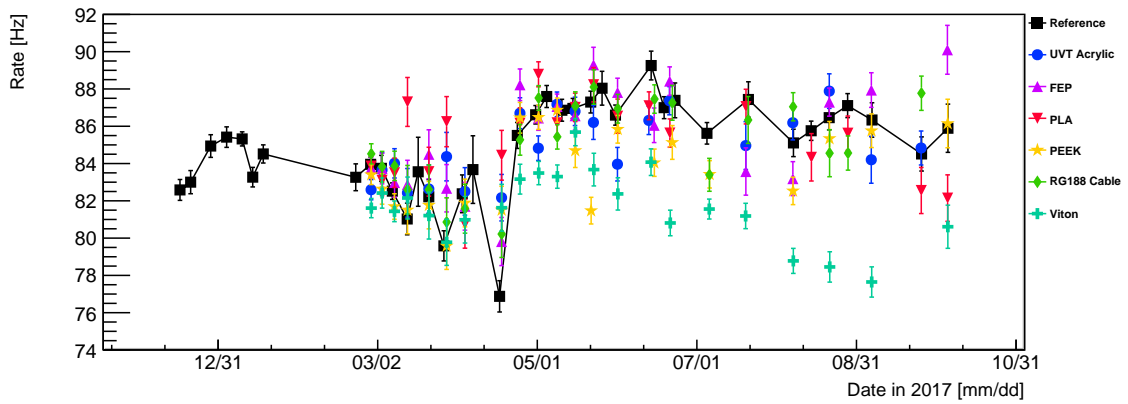


**Figure 5.7:**  $^{227}\text{Ac}$  rate for each material sample. Errors are statistical.

Systematic variations can be better understood by looking at the behavior of the  $^{215}\text{Po}$  energy distribution through time. This was done by fitting this distribution for the reference sample with a sum of two Gaussians to account for the non-Gaussian

nature of the peak as demonstrated in Figure 5.8. The mean and  $1\sigma$  width of each of these Gaussians versus time is show in Figures 5.9 and 5.10. It can be seen that the  $^{215}\text{Po}$  energy mean varies about 5% and the width around 15%.

The amount of variation seen in measured rates and the  $^{215}\text{Po}$  energy distribution indicate that the system is not repeatable and, as such, introduces significant systematic errors. Though the PMT and acrylic holder were glued in place, the sample vials were repeatedly removed and replaced, possibly shifting the placement of the acrylic holder and the optical grease. If the experiment were to be repeated a more robust detector system would be needed to eliminate these systematic errors.

To account for these variations all material sample rates,  $R_M$ , were compared to the reference sample rate,  $R_{ref}$ . The ratio of the rates was calculated for each time bin as

$$ratio = \frac{R_M}{R_{ref.}} \quad (5.5)$$

$$\sigma_{ratio} = ratio \times \sqrt{\left(\frac{\sigma_M}{R_M}\right)^2 + \left(\frac{\sigma_{ref.}}{R_{ref.}}\right)^2} \quad (5.6)$$

and the results are shown in Figure 5.11. The ratio of rates versus time, for each material, were fit with a constant and a straight line, the results of which are tabulated in Tables 5.5 and 5.6 respectively.

Except for the case of viton (discussed in the next section) there is no clear decrease

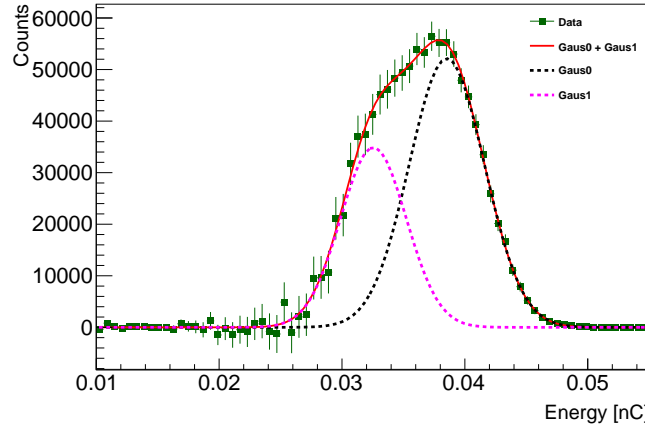


**Figure 5.8:**  $^{215}\text{Po}$  energy distribution for the reference sample, fit with a sum of two Gaussians. The total fit is seen in red, while the two Gaussians are drawn as the pink and black dashed lines.

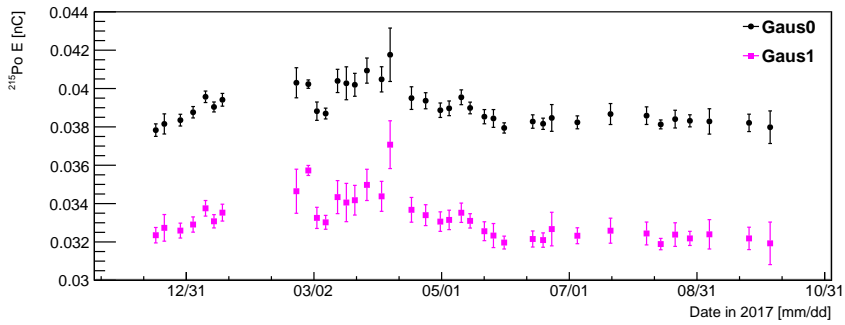


**Figure 5.9:** The mean of the two Gaussians fit to the  $^{215}\text{Po}$  distribution for the reference sample.

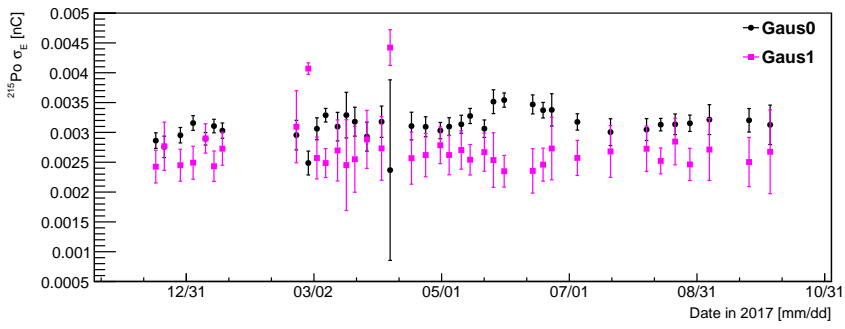


**Figure 5.10:** The  $1\sigma$  width of the two Gaussians fit to the  $^{215}\text{Po}$  distributions for the reference sample.

in rate observed over the six month period for any material. Though the chi-squared results for the constant fits are not ideal, the fits to a straight line result in slopes with 50% error to greater than 100% error, indicating that a decrease in rate is not a good model. Since no obvious and significant decrease was observed it was concluded that  $^{227}\text{Ac}$  was not adsorbing onto materials and next steps were taken to include the source in the final detector.

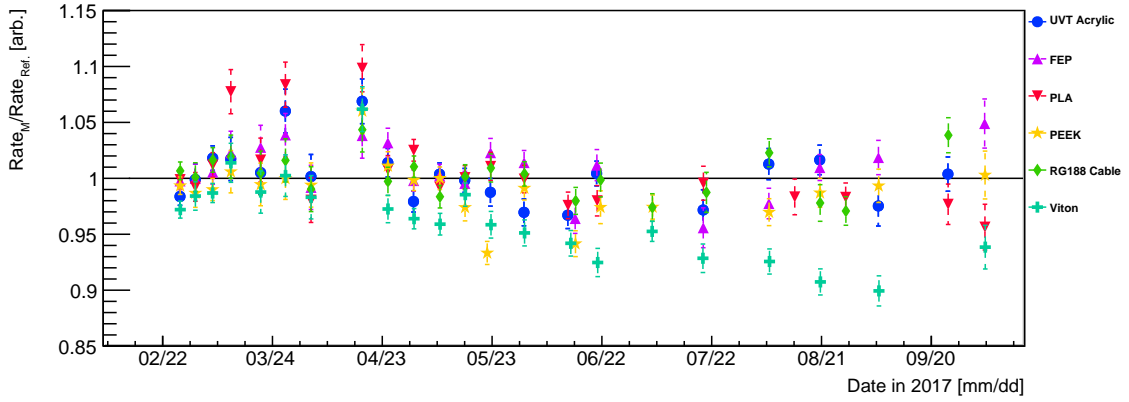


**Figure 5.11:**  $^{227}\text{Ac}$  rate for each material sample,  $M$ , relative to the reference sample.

Material	Constant	$\chi^2/\text{NDF}$
UVT Acrylic	$0.997 \pm 0.003$	$56.5/20 = 2.82$
FEP	$1.005 \pm 0.003$	$44.1/20 = 2.21$
PLA	$1.003 \pm 0.003$	$80.6/20 = 4.03$
PEEK	$0.985 \pm 0.003$	$70.9/20 = 3.55$
RG188 Cable	$1.001 \pm 0.003$	$38.3/21 = 1.82$
Viton	$0.960 \pm 0.002$	$136.3/21 = 6.49$

**Table 5.5:** The results of fitting the relative rate for each material sample with a constant.

Material	Constant	Slope [ratio/yr]	$\chi^2/\text{NDF}$
UVT Acrylic	$1.5 \pm 0.8$	$-0.01 \pm 0.02$	$56.2/19 = 2.96$
FEP	$1.3 \pm 0.8$	$-0.005 \pm 0.018$	$44.0/19 = 2.32$
PLA	$4.4 \pm 0.8$	$-0.07 \pm 0.02$	$64.3/19 = 3.38$
PEEK	$2.9 \pm 0.8$	$-0.04 \pm 0.02$	$65.2/19 = 3.43$
RG188 Cable	$2.3 \pm 0.8$	$-0.03 \pm 0.02$	$35.7/20 = 1.79$
Viton	$7.7 \pm 0.7$	$-0.14 \pm 0.02$	$48.9/20 = 2.45$

**Table 5.6:** The results of fitting the relative rate for each material with a straight line.

#### 5.2.4.1 Viton

Observation of the rate of  $^{227}\text{Ac}$  in the viton o-ring material sample vial initially indicates a decrease in rate over time, about 10% compared to the reference vial over a six month period. Upon further inspection, though, it becomes clear that the energy spectrum, of the Rn events in particular, shift toward the system threshold as time goes on. This causes a loss of events, not due to adsorbance, but rather due to threshold effects.

Figure 5.12 shows the  $^{219}\text{Rn}$  and  $^{215}\text{Po}$  energy distributions in the first and last time bins for both viton and PEEK. It can be seen that at the last time bin the viton distributions sit against the threshold, compared to the PEEK distributions which approach but do not get close to the threshold. To quantify this the  $^{219}\text{Rn}$  spectrum was fit with a sum of two Gaussians and the widths versus time are shown in Figure 5.13. It can be seen that the lower energy Gaussian becomes narrower as time goes on, indicating a loss of events due to threshold effects. Therefore, it was concluded that the decrease in  $^{227}\text{Ac}$  rate observed in the viton o-ring sample was due to threshold effects rather than adsorption.

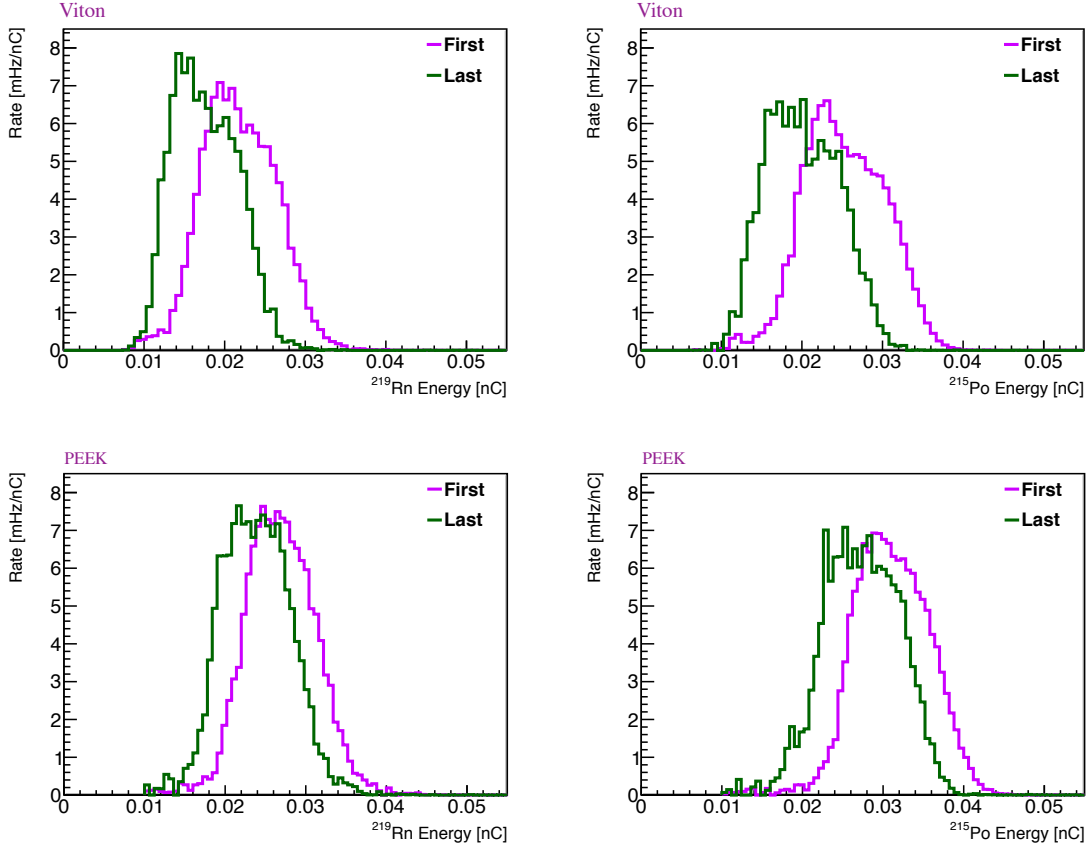


**Figure 5.12:**  $^{219}\text{Rn}$  and  $^{215}\text{Po}$  energy spectra for both the viton o-ring (top) and PEEK (bottom) material samples during the first and last time bins.

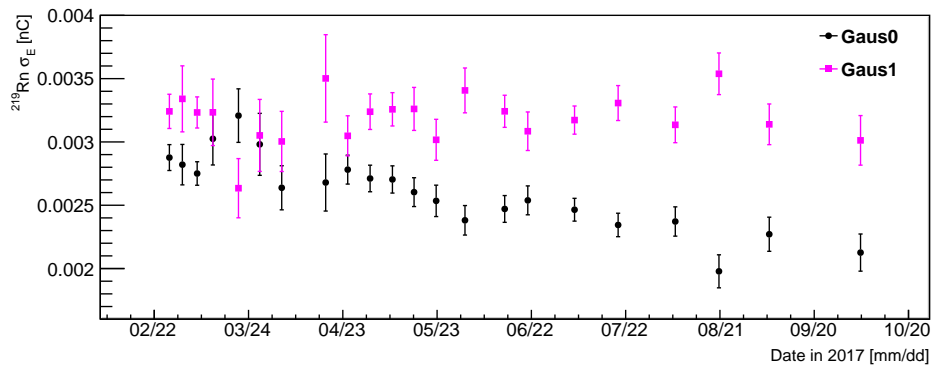


**Figure 5.13:** The  $1\sigma$  width of two Gaussians fit to the  $^{219}\text{Rn}$  energy spectrum versus time for the viton o-ring material sample. Black (circle): higher energy Gaussian, Magenta (square): lower energy Gaussian.

## 5.3 $^{227}\text{Ac}$ in the PROSPECT AD

Material compatibility testing determined that  $^{227}\text{Ac}$  did not adsorb onto detector materials, confirming that it could be used as a uniformly distributed source. It will be noted here that  $^{227}\text{Ac}$  spiked LiLS was added to a prototype detector that consisted of two stacked segments. This was done to determine that the  $^{227}\text{Ac}$  did not degrade the performance of the liquid scintillator and that it did not introduce significant background. Initial results from the prototype concluded that it did neither and provided the last step of evidence needed before addition to the full-scale detector.

### 5.3.1 Spiking the LiLS

After concluding that  $^{227}\text{Ac}$  would be added to the AD, the goal was to obtain a final activity of 0.01 Bq/segment. Assuming a total LiLS mass of 4600 kg and an active mass of 3939 kg implies a total  $^{227}\text{Ac}$  activity of 1.8 Bq. The stock solution from which the LiLS would be spiked was the same stock that was used for the material studies, which had an activity of  $\sim 9.13$  Bq/g on December 13, 2017, the day the spiking procedure was performed. This means that  $\sim 200$  mg of the stock was needed to spike the LiLS.

In order to add  $^{227}\text{Ac}$  to the total detector, a vial of spiked LiLS was added to a 55-gallon drum of LiLS prepared previously for detector filling. Before the detector was filled all drums were added to an ISO-tank and bubbled with nitrogen to ensure thorough mixing of the LiLS from all drums and the  $^{227}\text{Ac}$ .

Spiking of the drum was done by adding the stock solution to an intermediate vial of production LiLS before spiking the vial that is added to the drum. This was done to offset the estimated 10 mg uncertainty of the balance used to weigh the vials and allows an assessment of the activity of the remaining vial. The procedure was also repeated in a second set of vials so that both vials could be measured.

The spiking procedure was performed using four vials, V0, V1, V2, and V3. The steps were:

- (i) Fill all four vials with production LiLS
- (ii) Fill V1 and V2 with the  $^{227}\text{Ac}$  spiked LiLS stock solution
- (iii) Fill V0 with solution from V1 until desired activity is reached

- (iv) Fill V3 with solution from V2 until desired activity is reached
- (v) Empty V0 into drum of production LiLS

See Figure 5.14 for a graphic of these steps along with Table 5.7 for a list of the weights of all solutions added and removed from the vials. Filling of all vials was performed using pipettes, therefore, some drops inevitably remained in the pipette at every step. Vials V1 and V2 were gently swirled after the addition of the  $^{227}\text{Ac}$  spiked LiLS in an attempt to mix the solution.

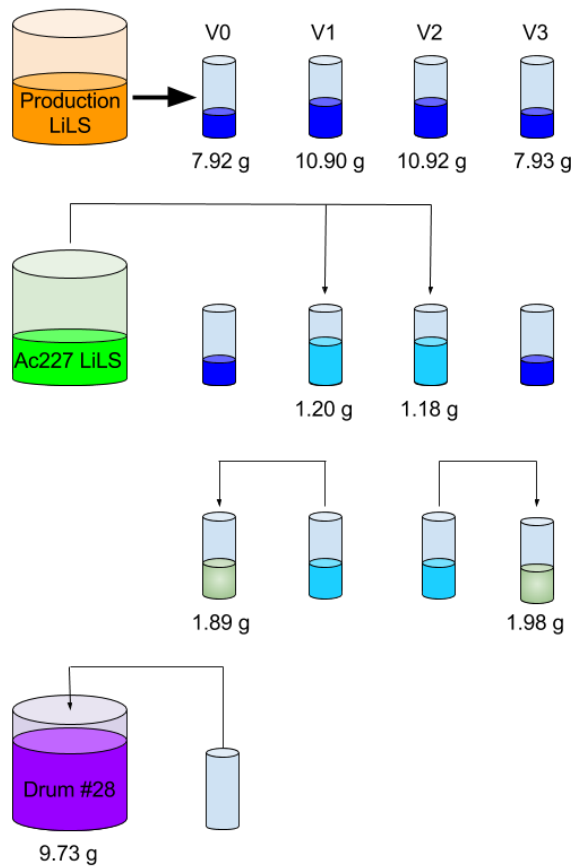


**Figure 5.14:** A graphic of the procedure used to spike the drum of LiLS with  $^{227}\text{Ac}$  for filling of the AD.

The expected  $^{227}\text{Ac}$  rate,  $A$ , in vials V0(V3) can be calculated as

$$A = C m_2 \frac{m_4}{m_1 + m_2} \quad (5.7)$$

where  $C$  is the activity of the  $^{227}\text{Ac}$  spiked stock solution, 9.13 Bq/g,  $m_1$  is the amount

	<b>V0</b>	<b>V1</b>	<b>V2</b>	<b>V3</b>
<b>Production LiLS added, <math>m_1</math> (g)</b>	7.92	10.90	10.92	7.925
<b><math>^{227}\text{Ac}</math> spiked solution added, <math>m_2</math> (g)</b>		1.20	1.18	
<b>Solution removed, <math>m_3</math> (g)</b>		2.047	2.09	
<b>Solution added, <math>m_4</math> (g)</b>	1.885			1.98

**Table 5.7:** The weight of all solutions added and removed from the four vials for spiking of the LiLS with  $^{227}\text{Ac}$  for filling of the AD.

<b>Vial</b>	<b>Expected Activity [Bq]</b>	<b>Measured Rate [Hz]</b>
V0	1.71	
V1	9.10	$9.48 \pm 0.04$
V2	8.91	$9.38 \pm 0.06$
V3	1.76	$0.696 \pm 0.001$

**Table 5.8:** Expected and measured  $^{227}\text{Ac}$  activity in vials prepared for spiking the LiLS.

of production LiLS added to V1(V2),  $m_2$  is the amount of the stock solution added to V1(V2), and  $m_4$  is the amount of solution from V1(V2) that was added to V0(V3). The expected rate in vials V1(V2) is calculated as

$$A = C m_2 \left( 1 - \frac{m_3}{m_1 + m_2} \right) \quad (5.8)$$

where  $m_3$  is the amount of solution removed from V1(V2). The expected  $^{227}\text{Ac}$  activity for each vial is listed in Table 5.8.

The  $^{227}\text{Ac}$  rate in vials V1, V2, and V3 were measured after adding V0 to the drum of LiLS. The rate of  $^{227}\text{Ac}$  in V3 should be similar to the rate in AD, recalling that the goal was 1.8 Bq. A plot of the measured rates for each vial is shown in Figure 5.15. Each of these rates was fit with a constant, with the results of these fits listed in Table 5.8. It can be seen that the measured rates in V1 and V2 are about 4% higher than expectation, and the rate in V3 is about 50% lower. A possible explanation for this discrepancy is that the solution was not sufficiently mixed before transferring between the stock solution and the vials and between the vials themselves. If this experiment was to be repeated a more thorough testing of transfer procedures would need to be performed. In conclusion, the measured rate in V3 indicates that the  $^{227}\text{Ac}$  rate in the PROSPECT AD should be around 0.7 Hz, less than half of the initial goal.

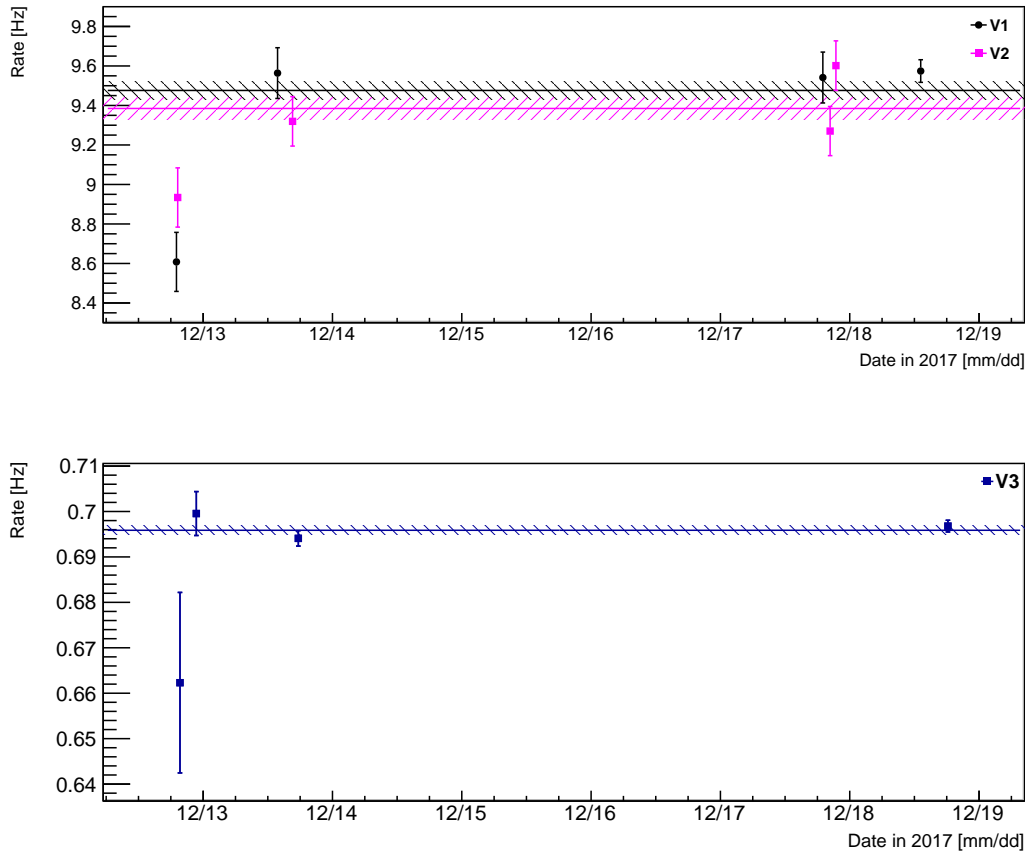


**Figure 5.15:** Measured  $^{227}\text{Ac}$  rates of vials used in the procedure performed to add  $^{227}\text{Ac}$  to the LiLS of the PROSPECT AD. Top: intermediate vials V1 and V2. Bottom: V3, filled in the same method as the vial that was added to the drum of LiLS. All rates were fit with a constant, the results drawn as solid lines with hashed lines representing the error.

### 5.3.2 Data Set

PROSPECT began taking data in March 2018. The data set used for the  $^{227}\text{Ac}$  analysis runs from March 5, 2018 - October 6, 2018, with a break from March 31, 2018 - April 17, 2018 when the detector was off for maintenance. The total runtime is 4048.9 hrs, with 4011.7 hrs of livetime data. 2293.7 hrs of the runtime is reactor on data, and 1755.2 hrs of reactor off.

During the data collection period used for this analysis, several PMTs exhibited abnormal behavior, including current instabilities, and are no longer in operation.

Preliminary theories for the cause of this are that LiLS leaked into the PMT housings and damaged the voltage dividers, but this has yet to be confirmed. To account for this all segments that ‘turned off’ during the data period are excluded in this analysis. The result is 90 active segments, as shown in Figure 5.16.

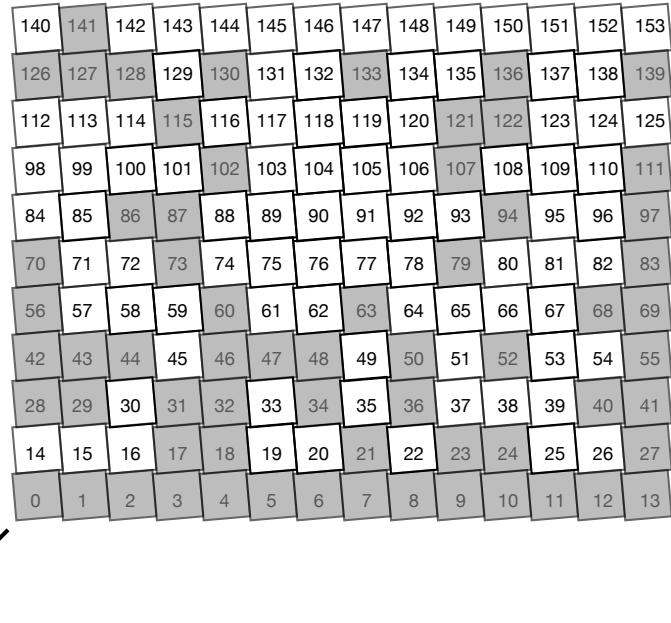


**Figure 5.16:** Graphic of 154 segments of the PROSPECT AD. Grayed out segments are those that ‘turned off’ during the data period and are excluded in this analysis.

### 5.3.3 Event Selection

RnPo events in the PROSPECT detector were found by looking at event clusters. A cluster is defined as a collection of events that occur within 20 ns of each other. Time coincident events were found by first looking for delay (Po) events. It was required that these events existed in a single multiplicity cluster and passed broad energy and PSD cuts outlined in Table 5.9.

Coincident prompt events were found by looking in a  $5\tau$  time window before the delay event, where  $\tau$  is the lifetime of  $^{215}\text{Po}$ , 2.57 ms. It was required that the highest energy event in a given cluster in that time window occurred in the same segment as the delay event and passed the energy and PSD cuts in Table 5.9. The distance between the prompt and delay event was also required to be less than 250 mm. Accidental prompt events were found by looking in a  $5\tau$  time window offset  $10\tau$

Prompt Energy	$0.48 < E < 1.18 \text{ MeVee}$
Delay Energy	$0.61 < E < 1.18 \text{ MeVee}$
PSD	$0.16 < \text{PSD} < 0.36$
$\Delta z =  z_{\text{delay}} - z_{\text{prompt}} $	$\Delta z < 250 \text{ mm}$
$\Delta t = t_{\text{delay}} - t_{\text{prompt}}$	$\Delta t < 5\tau \text{ ms}$

**Table 5.9:** Broad cuts used to find RnPo events, where  $\tau$  is the lifetime of  $^{215}\text{Po}$ , 2.57 ms.

before the delay event. The same cuts applied to coincidental prompt events were applied to accidental prompt events.

In addition to energy, PSD, and position cuts a pileup veto was applied to all events. At the time of a trigger event all boards are signaled to begin a 592 ns acquisition window. Events arriving at the end of this window do not re-trigger the data acquisition system, thus causing truncated waveforms. In order to avoid using these truncated events, any cluster preceded by another cluster in a 800 ns window is vetoed.

The broad energy and PSD cuts listed in Table 5.9 are applied on a first pass analysis of the PROSPECT data. Changes in detector performance over time, including decreasing energy resolution and PSD, required a second pass of the data, in which the lower bounds of the energy and PSD cuts were changed to be  $4\sigma$  lower than the mean of the distributions for a given time bin or segment. The PSD versus energy and  $^{215}\text{Po}$  energy versus  $^{219}\text{Rn}$  energy distributions, after accidental subtraction, can be seen in Figure 5.17.

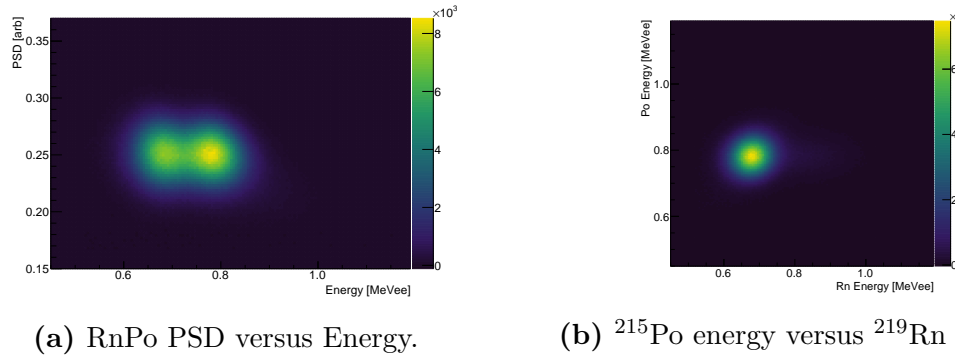


**Figure 5.17:** RnPo distributions for all cells integrated over all time.

### 5.3.4 Rate Calculation

The  $^{227}\text{Ac}$  rate per segment, or for a given time period, is found by fitting the background subtracted  $\Delta t$  distribution, where  $\Delta t = t_{\text{delay}} - t_{\text{prompt}}$ , with

$$f(t) = N e^{-t/\tau} \quad (5.9)$$

where  $N$  and  $\tau$ , the lifetime of  $^{215}\text{Po}$ , are allowed to vary. For an example of these distributions and fit for a typical segment see Figure 5.18. The rate is then calculated as

$$R = \frac{N \tau}{\Delta t\text{-bin-width} \times \text{livetime} \times \text{efficiency}} \quad (5.10)$$

$$\sigma_R = R \times \sqrt{\left(\frac{\sigma_N}{N}\right)^2 + \left(\frac{\sigma_\tau}{\tau}\right)^2 + \frac{2\sigma_{N\tau}}{N\tau} + \left(\frac{\sigma_{\text{eff.}}}{\text{eff.}}\right)^2} \quad (5.11)$$

where  $N$  and  $\tau$  are results of the  $\Delta t$  fit. The robustness of this fit can be tracked by observing the resulting values for  $\tau$  per individual segment and versus time for all segments and comparing the averages to the currently accepted value for the lifetime of  $^{215}\text{Po}$ ,  $2.569 \pm 0.007$  ms. These results are shown in Figure 5.19. The average lifetime per individual segment is  $2.564 \pm 0.002$  ms, and versus time for all segments in  $2.565 \pm 0.002$  ms, in great agreement with the accepted lifetime.

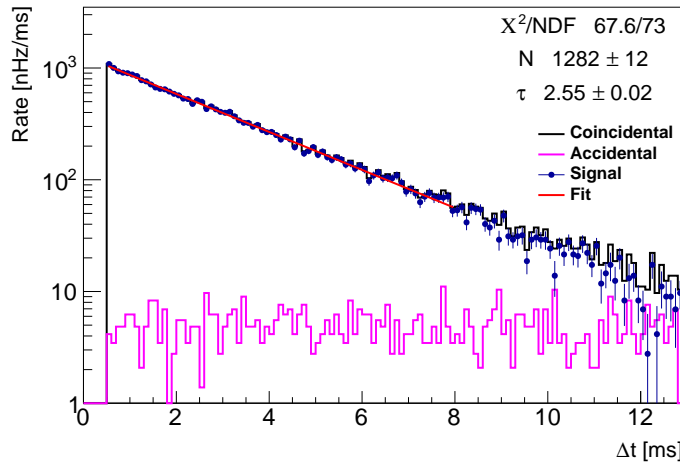


**Figure 5.18:** Coincidental (black), accidental (magenta), and background subtracted (blue)  $\Delta t$  distributions for a typical segment integrated over all time. A fit of Equation 5.9 to the background subtraction distribution is shown in red along with its results.

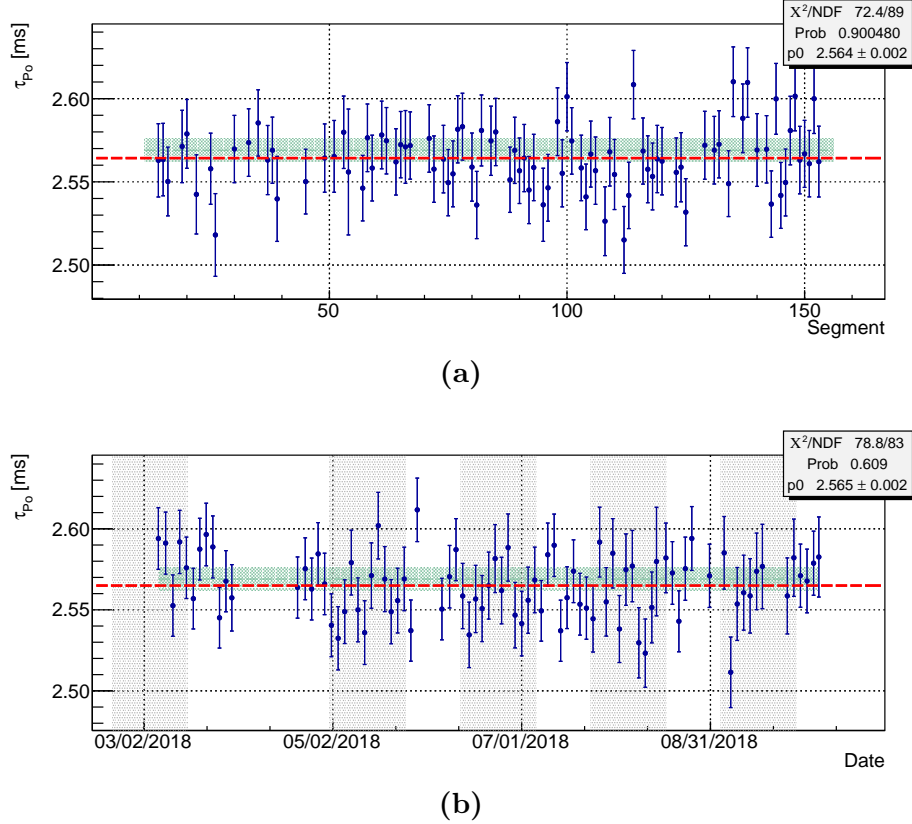


**Figure 5.19:** The value of  $\tau$  obtained from the exponential fit to the  $\Delta t$  distribution for each individual segment integrated over all time (a) and for all segments versus time (b). The currently accepted value for  $\tau$ ,  $2.569 \pm 0.007$  ms, is marked by the shaded green area. A constant fit to the data is shown as the dashed red line.

The uncorrected livetime is calculated, for each data run, as the time from the beginning of the run to the time of the last delay candidate event. This is summed for all analyzed runs. This livetime is corrected for the dead time introduced by the pileup veto. This correction is calculated as the number of clusters,  $N_{Clusts}$ , times the pileup veto time, 800 ns. Figure 5.20 shows the dead time, as a fraction of livetime, versus time. Because the veto is applied to both prompt and delay candidates the livetime is corrected with  $2 \times$  the dead time as

$$\text{livetime} = \sum (t_{\text{finalPo}} - t_0) - 2.0 \times N_{Clusts} \times 800\text{ns} \quad (5.12)$$

When measuring the rate per segment the same livetime is applied to all segments. The efficiency is calculated for energy and PSD cuts on both prompt and delay

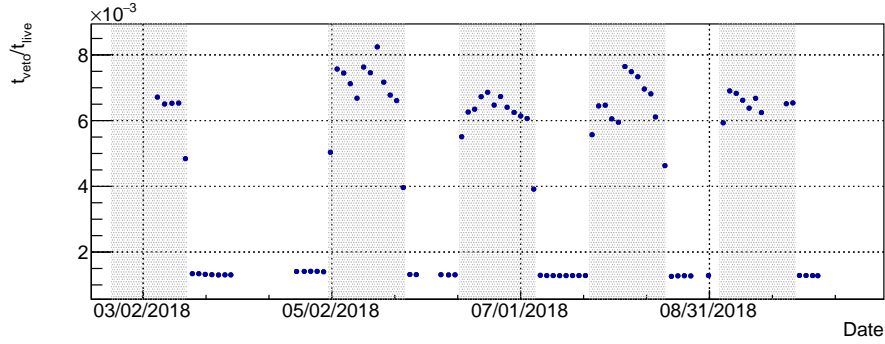


**Figure 5.20:** The dead time, as a fraction of livetime, due to the pileup veto versus time. Shaded areas are reactor on periods.

events, and for the  $\Delta z$  cut. This is done by fitting each distribution with a Gaussian  $\pm 2\sigma$  from the mean, with the exception of the prompt energy which is fit from  $-1.3\sigma$  to  $+0.6\sigma$ . The efficiency is then calculated as the ratio of the integral of the Gaussian between the cuts for that distribution to the integral between  $\pm\infty$ , as defined in Equation 5.13. The error on the efficiency is treated as a binomial error. For an example of the distributions and fits for a typical segment see Figure 5.21.

$$\text{Eff} = \frac{\int_{\text{low-cut}}^{\text{high-cut}} g(u)du}{\int_{-\infty}^{\infty} g(u)du} \quad \sigma_{\text{Eff}} = \sqrt{\frac{\text{Eff}(1 - \text{Eff})}{N}} \quad (5.13)$$

It should be noted here that although the  $^{219}\text{Rn}$  energy distribution has a high energy tail, due to the accompanying gammas, the efficiency is calculated using a single Gaussian fit around the peak. This is valid as long as the high energy cut is always wide enough to include the whole high energy tail, which is true for this analysis.

In general the total efficiency is 99.9% or higher, for RnPo rates calculated in individual segments or versus time. Figures 5.22 and 5.23 show the efficiency calculated for all distributions for all individual segments and versus time, respectively.

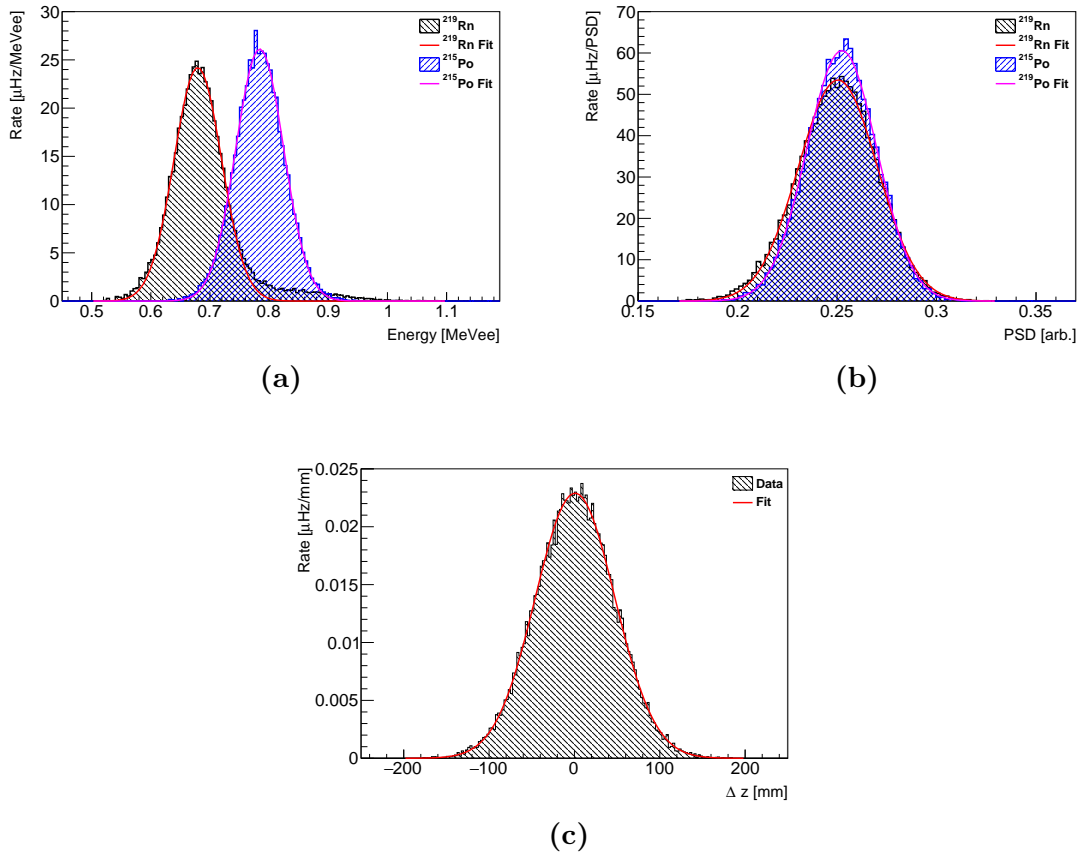


**Figure 5.21:** Energy (a), PSD (b), and  $\Delta z$  (c) distributions for RnPo events in a typical segment integrated over all time. Also shown are the results of fitting each distribution with a Gaussian for the purpose of calculating the cut efficiencies.

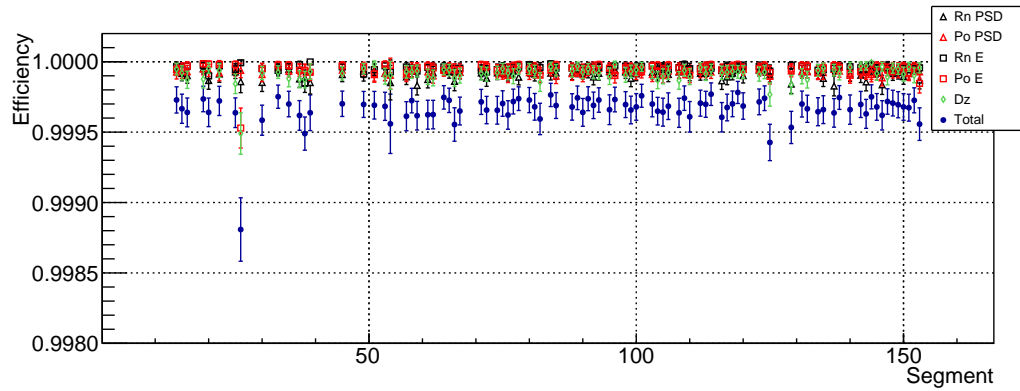


**Figure 5.22:** Cut efficiencies calculated for RnPo events in individual segments integrated over all time.

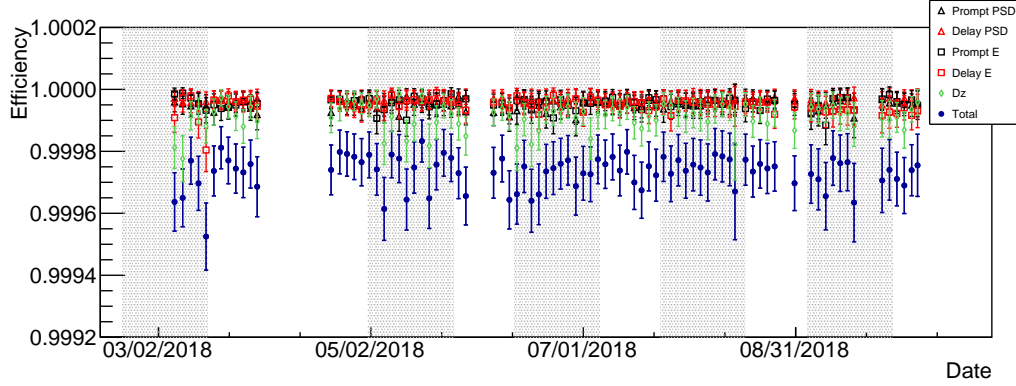


**Figure 5.23:** Cut efficiencies calculated for RnPo events versus time integrated over all segments. Shaded areas are reactor on periods.

### 5.3.5 Detector Performance as Tracked with $^{227}\text{Ac}$

Though  $^{227}\text{Ac}$  was added to the detector to track the product of efficiency  $\times$  volume for all segments, the mono-energetic  $^{215}\text{Po}$   $\alpha$  is also useful for tracking the performance of the detector and the applied calibrations. Figure 5.24 shows the mean and  $1\sigma$  width of the  $^{215}\text{Po}$  energy distribution versus time, integrated over all segments. It can be seen that the resolution is not stable over time, but rather decreases by  $\sim 20\%$  over a period of 7 months. This is due to an overall decrease in light collection over time, implying some factor of scintillator degradation, whose cause is not yet understood.

To correct for this in the IBD analysis a variable called  $E_{smear}$  was introduced, in which all energy distributions are artificially smeared to match the worst resolution in a given data taking period. The results of this are also shown in Figure 5.24, and it can be seen that the new  $E_{smear}$  resolution values are time-stable within  $\pm 3\%$  and the mean values within  $\pm 0.4\%$ . Note that the sharp variations in the energy mean values correspond to changes in calibration constants.

Though introducing the  $E_{smear}$  variable corrects for changing detector characteristics, the  $^{227}\text{Ac}$  analysis uses  $E$ . The decreasing resolution is accounted for by applying  $\sigma$ -based cuts to the energy.

The mean and width of the  $^{215}\text{Po}$  PSD distribution versus time are shown in Figure 5.25. Similar behavior as was seen in the energy distribution also occurs to the PSD. Over the 7 month period the PSD distribution increases in width by  $\sim 11\%$  as the mean decreases by  $\sim 9\%$ . This is accounted for the  $^{227}\text{Ac}$  analysis by the use of  $\sigma$ -based cuts on the PSD distributions.

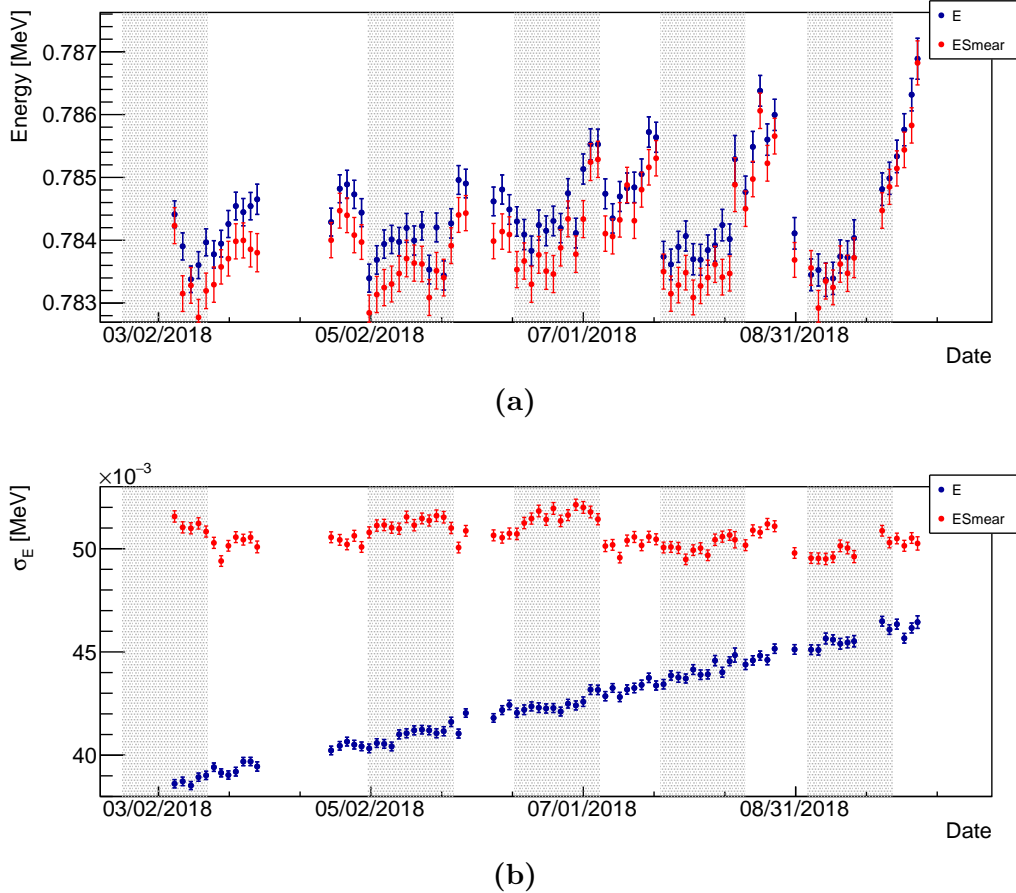


**Figure 5.24:** Mean (a) and  $1\sigma$  width (b) of the  $^{215}\text{Po}$  energy distribution versus time integrated over all segments. Both before applied a correction (E) and after correction (ESmear) are shown. Shaded areas are reactor on periods.

The  $z$  resolution of  $\alpha$  events, which are highly localized, can be seen by looking at the width of the distribution of the distance between  $^{219}\text{Rn}$  and  $^{215}\text{Po}$  signals. This is plotted versus time, integrated over all segments, in Figure 5.26. It can be seen that the width increases by 7% over the 7 month period, about 3.5 mm. This variation is accounted for in the  $^{227}\text{Ac}$  analysis in the same way as was done for energy and PSD, by using  $\sigma$ -based cuts.

Features of the  $^{215}\text{Po}$  distribution are also useful to compare stability between segments. Figure 5.27 shows the distributions of the  $^{215}\text{Po}$  energy, energy resolution, position, and position resolution in all individual segments. For Hamamatsu segments the energy scale and resolution are identical between segments to within  $\sim \pm 0.25\%$

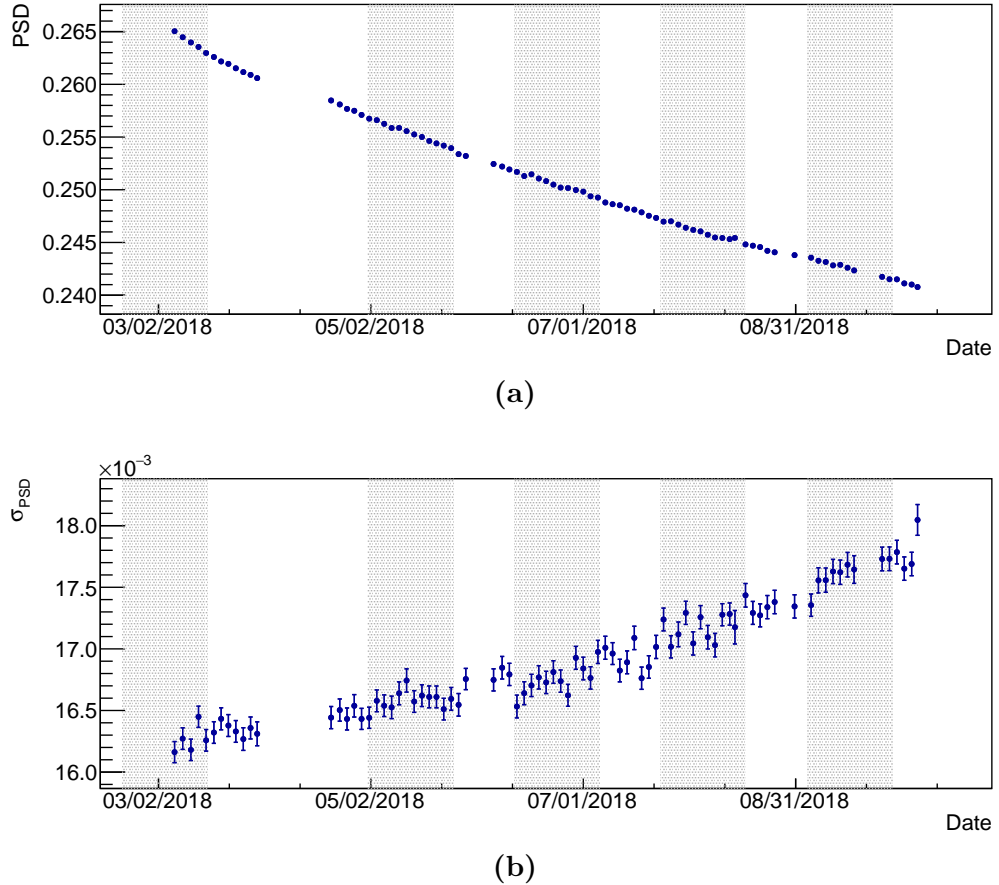


**Figure 5.25:** Mean (a) and  $1\sigma$  width (b) of the  $^{215}\text{Po}$  PSD distribution versus time integrated over all segments. Shaded areas are reactor on periods.

and  $\sim \pm 6.5\%$  respectively. The ET segments vary more than the Hamamatsu segments, but for the case of the IBD analysis these segments are considered outside of the fiducial volume.

The alignment of  $z$  between all segments can be observed by looking at the distribution of the mean of the position distribution for all segments. It can be seen that, for Hamamatsu segments, all position reconstructions are aligned within  $\pm 7$  mm. The width of the  $\Delta z$  distributions in Hamamatsu segments have a segment-to-segment variation of  $\sim \pm 4$  mm.

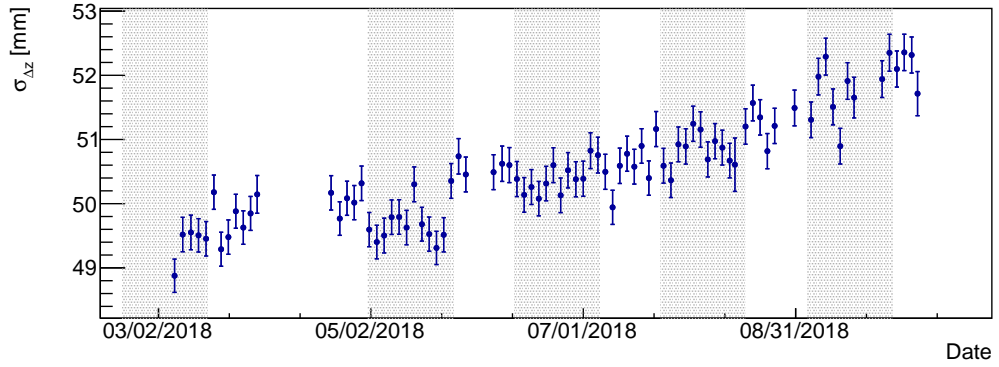


**Figure 5.26:**  $1\sigma$  width of the  $\Delta z$  distribution versus time. Shaded areas are reactor on periods.

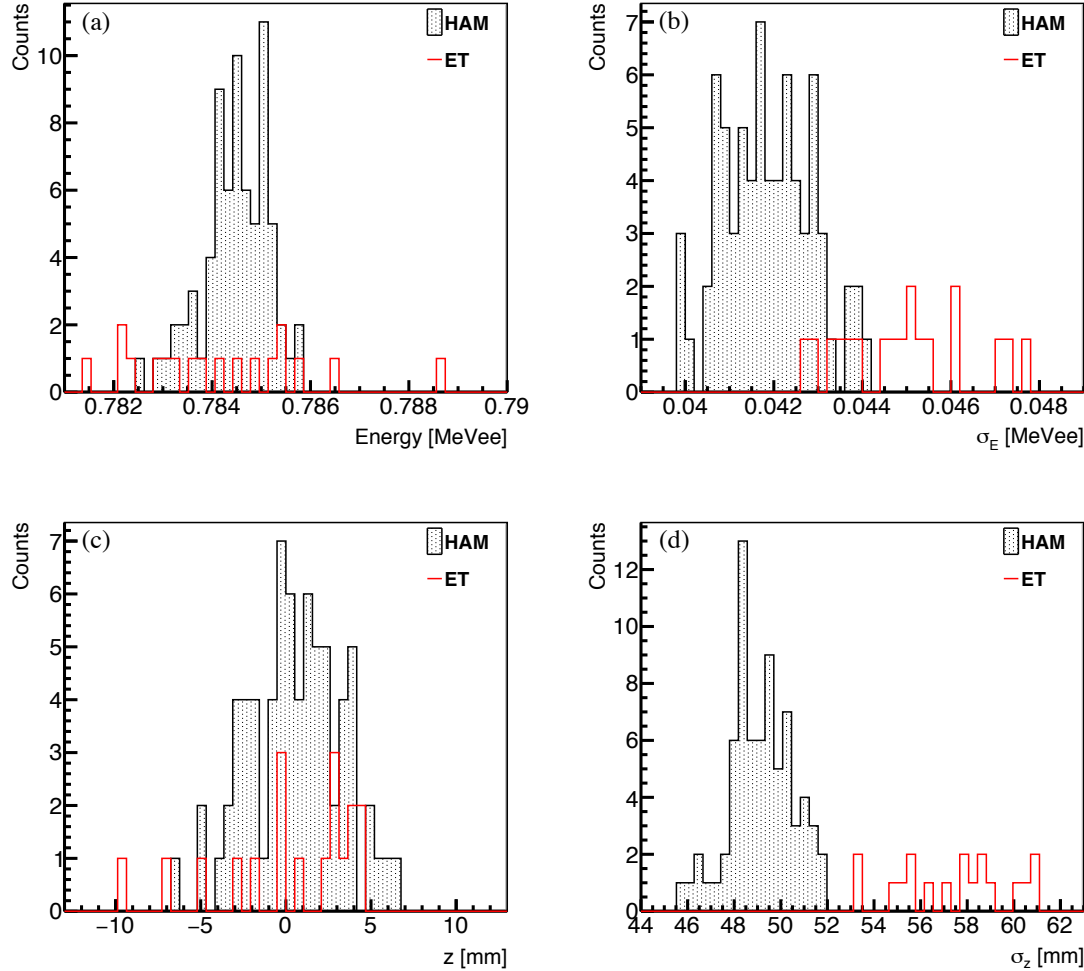


**Figure 5.27:** Segment-to-segment stability of the  $^{215}\text{Po}$  energy (a), energy resolution (b), position reconstruction (c), and position resolution (d). Distributions are shown separately for Hamamatsu and ET segments.

$^{227}\text{Ac}$  has proven to be useful in tracking energy, energy resolution, position, and position resolution over time and between segments. Though IBD events are characteristically very different from RnPo  $\alpha$  events, in energy and spatial event topologies, these distributions help to provide limits on systematic errors applied to the IBD analysis due to changing resolution effects and position reconstruction. They also provide useful cross-checks for the behavior of new variables, such as  $E_{smear}$ , and tracking calibration performance over time.

### 5.3.6 $^{227}\text{Ac}$ Rate versus Time

Observing the rate of  $^{227}\text{Ac}$  in the AD over time provides a cross-check of the analysis while giving insight into the behavior of the detector. Figure 5.28 shows the  $^{227}\text{Ac}$  rate measured versus time, integrated over all segments. This is fit twice with an exponential of the form

$$f(t) = R_0 e^{\frac{-(t-t_0) \ln(2)}{t_{1/2}}} \quad (5.14)$$

where  $R_0$  is allowed to vary both times and  $t_{1/2}$ , the half-life of  $^{227}\text{Ac}$  ( $21.772 \pm 0.003$  yrs), is fixed for one fit and allowed to vary in the other.

When the half-life is allowed to vary, the fit returns a half-life of  $11.73 \pm 0.69$  yrs, suggesting that the measured rate of  $^{227}\text{Ac}$  in the AD is falling  $1.56 \pm 0.21$  % faster than expectation over a period of 7 months. The reason for this discrepancy is

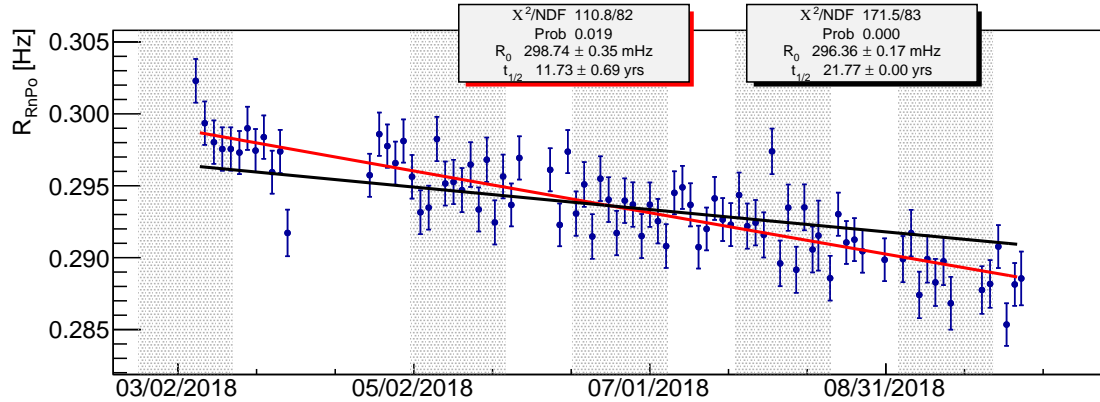


**Figure 5.28:**  $^{227}\text{Ac}$  rate as measured versus time integrated over all segments. Fit with two exponentials, one in which the half-life of  $^{227}\text{Ac}$  is allowed to vary (red) and one in which it is fixed (black). Errors are statistical. Shaded areas are reactor on periods.

unclear. Measurements of the  $^{215}\text{Po}$  lifetime versus time, Figure 5.19b, are consistent with its accepted lifetime, suggesting that the analysis is correctly accepting and measuring RnPo events. The use of  $\sigma$ -based cuts for energy, PSD, and  $\Delta z$  result in efficiencies that are always 99.9% or higher, ruling out loss of events due to changing resolution as a solution.

One hypothesis is that  $^{227}\text{Ac}$  is falling out of the LiLS solution. The process by which this would occur is unclear, but, in an attempt to gain more insight the detector was split into five sections of two rows each, as shown in Figure 5.29. The  $^{227}\text{Ac}$  rate in each of these sections was measured and fit with the exponential in Equation 5.14, allowing the half-life to vary. See Figure 5.30 for the rates and fits, and Figure 5.31 for the half-lives from the fit results versus row.

Though these results are statistics limited, a gradient from top to bottom can be seen in which the half-life gets shorter as one moves to the top of the detector. This could be a sign of  $^{227}\text{Ac}$  falling out of solution and sinking to the bottom of the detector. The process by which this would happen, though, is unclear. It is also not understood if it would sink in each individual segment, in which case a gradient might not be measured, or if it would all sink to the bottom.

In any case, the fact that the measured  $^{227}\text{Ac}$  rate deviates from expectation indicates that it is not a clear proxy for a relative segment-by-segment volume  $\times$  efficiency measurement. To account for this a 1% systematic error will be applied to the segment-by-segment measured  $^{227}\text{Ac}$  rates.

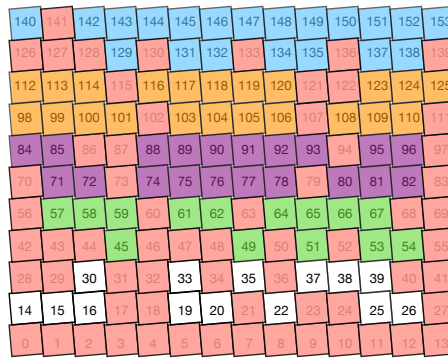


**Figure 5.29:** The PROSPECT detector divided into five sections of two rows each. Segments shaded in red are excluded from this analysis.

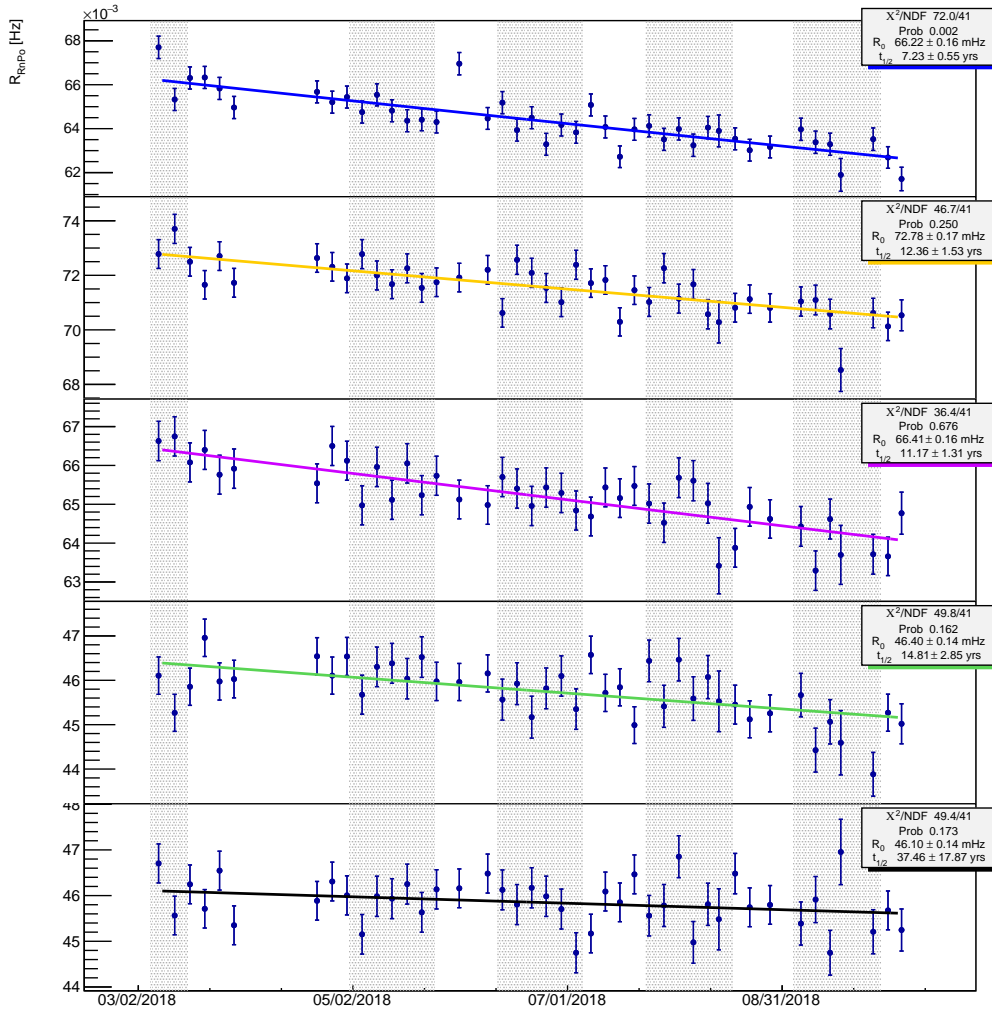


**Figure 5.30:** The measured  $^{227}\text{Ac}$  rate versus time for each section of two rows, fit with an exponential in which the half-life is allowed to vary.

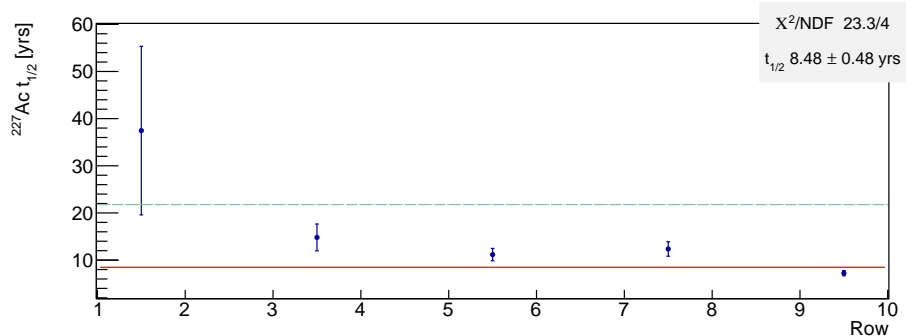


**Figure 5.31:** The half-life results from fitting the  $^{227}\text{Ac}$  rate versus time for five sections of two rows.

### 5.3.7 $^{227}\text{Ac}$ Rate in Individual Segments

The measured  $^{227}\text{Ac}$  rate in each segment can be seen in Figure 5.32. Statistical errors for each segment are around 0.6%. The average rate, including Hamamatsu and ET segments, is  $3.262 \pm 0.002$  mHz, 67% lower than the original spiking goal of 0.01 Bq/segment. The majority of segments vary  $\pm 1\%$  from the average.

The most glaring outliers are the top row, which are  $\sim 1.5\%$  below average. A possible explanation for this is that the top row is not completely filled with scintillator, but the reason for these lower rates is unclear.

If the focus is shifted to only Hamamatsu segments, the fiducial segments, the average is found to be  $3.270 \pm 0.002$  mHz, see Figure 5.33. The measured  $^{227}\text{Ac}$  rates in all fiducial segments agree to within  $\pm 2\%$ . A histogram of the individual segment rates is shown in Figure 5.34. The standard deviation of only the Hamamatsu segments is 0.026 mHz.

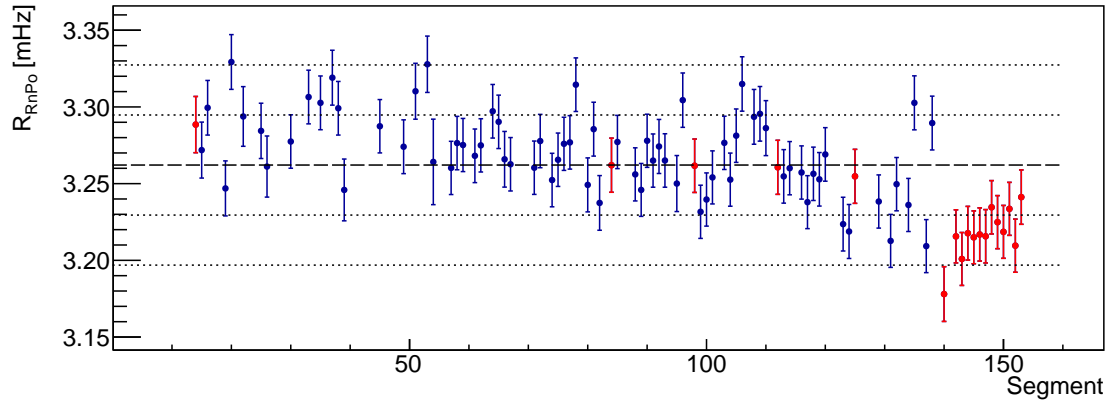


**Figure 5.32:** The  $^{227}\text{Ac}$  per individual segment integrated over all time. Dashed line represents the average over all segments. Dotted lines are  $\pm 1\%$  and  $\pm 2\%$  from the average. Blue: Hamamatsu segments, red: ET segments. Errors are statistical.

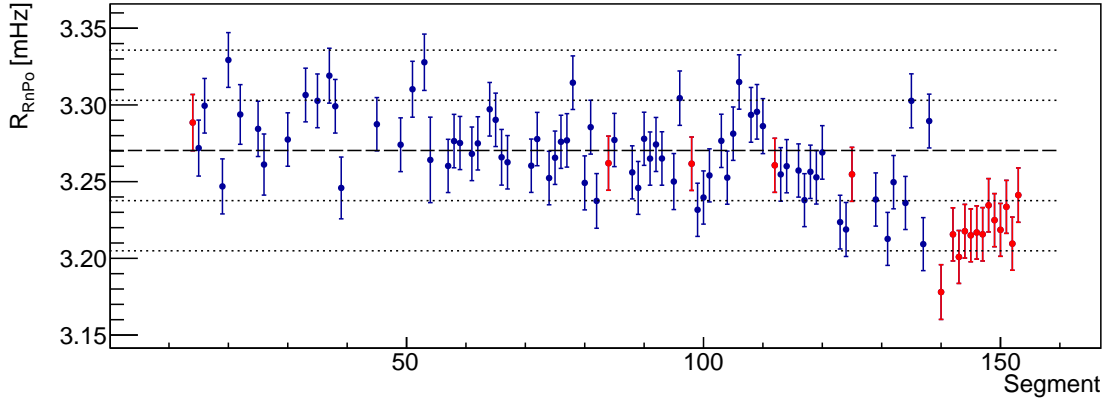


**Figure 5.33:** The  $^{227}\text{Ac}$  per individual segment integrated over all time. Dashed line represents the average over only Hamamatsu segments. Dotted lines are  $\pm 1\%$  and  $\pm 2\%$  from the average. Blue: Hamamatsu segments, red: ET segments. Errors are statistical. [remove ETs from plot]

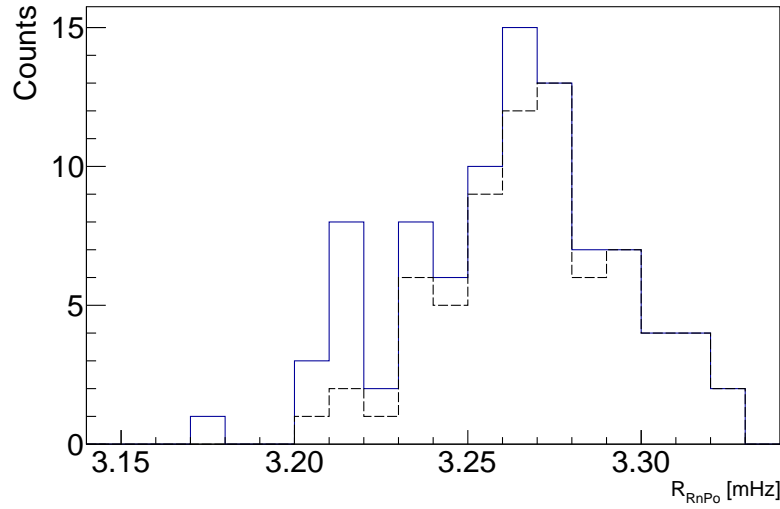


**Figure 5.34:** Histogram of the individual segment  $^{227}\text{Ac}$  rates. Blue (solid): Hamamatsu and ET segments, StdDev = 0.031 mHz. Black (dashed): only Hamamatsu segments, StdDev = 0.026 mHz.

### 5.3.8 Systematic Errors

Systematic uncertainties in this analysis come from three sources: (i) the  $^{227}\text{Ac}$  rate is falling faster than expectation (for this a 1% systematic is applied), (ii) the energy, PSD, and  $\Delta z$  cut efficiencies are calculated by assuming that all distributions are true

Gaussians (for this a 0.15% error is assigned), and (iii) the presence of other coincident alpha decays in the background that could contaminate the RnPo selection (for this a 0.22% error is assigned).

### 5.3.8.1 Energy, PSD, and $\Delta z$ Cuts

In an effort to determine what level of systematic error to apply to the measured  $^{227}\text{Ac}$  rates per segment a study was performed on the energy, PSD, and  $\Delta z$  cuts. For each cut (prompt and delay energy and PSD, and  $\Delta z$ ) the width of the cut was changed from  $2.5\sigma$  about the mean to  $4.0\sigma$  in steps of  $0.5\sigma$  with the exception of an added step at  $3.8\sigma$ . The rate per segment was calculated for each of these instances and compared to the rate per segment when all cuts were at  $4.0\sigma$ . An example of the calculated rate per segment when the delayed energy cut is changed in this way can be seen in Figure 5.35.

For each segment and each cut, the quantity

$$\frac{R_{4\sigma} - R_{i\sigma}}{R_{4\sigma}} \quad (5.15)$$

is calculated, where  $R_{4\sigma}$  is the rate when a  $4\sigma$  cut is used and  $R_{i\sigma}$  is the rate when a  $i\sigma$  cut is used where ( $i$ : 2.5, 3.0, 3.5, 3.8). This process was completed for the total data set and for a simulation set. The simulation was done as an  $^{227}\text{Ac}$  source dissolved in the scintillator in the AD with no reactor or ambient background. The distributions of these results for data can be seen in Figure 5.36.

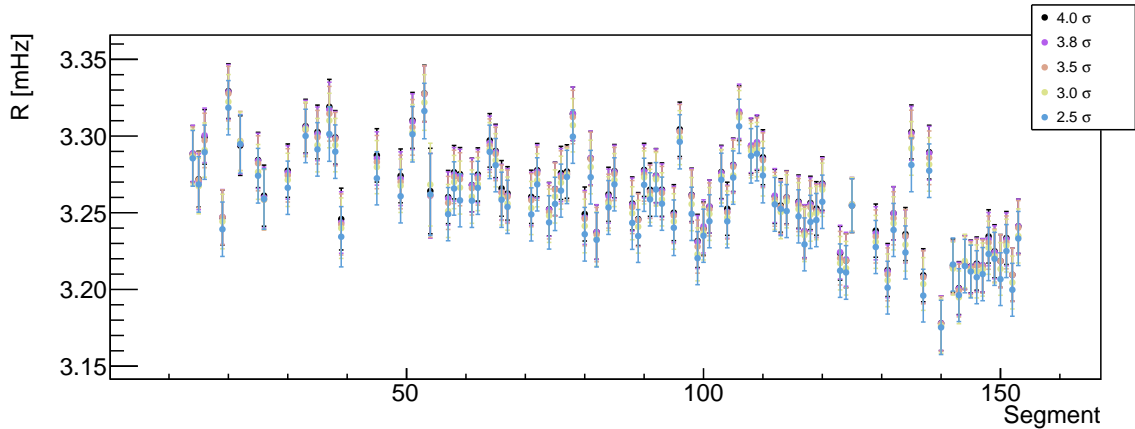


**Figure 5.35:**  $^{227}\text{Ac}$  rate per segment for different  $\sigma$ -based cuts on the delayed energy.

The mean of each of these distributions is found and plotted according to the  $\sigma$  cut used in Figure 5.37. The simulation results are shown in the same figure. It can be seen that the mean of all distributions converge to zero at  $4\sigma$  with the maximum change in rate being  $\sim 0.6\%$  at  $2.5\sigma$ .

If the method used to calculate efficiency was perfect (implying that all distributions are true Gaussians), then the rate would not depend on the  $\sigma$  cut that is applied. The results of this study show that this is not true and, therefore, a systematic error of 0.15% will be applied to all measured  $^{227}\text{Ac}$  rates per segment.

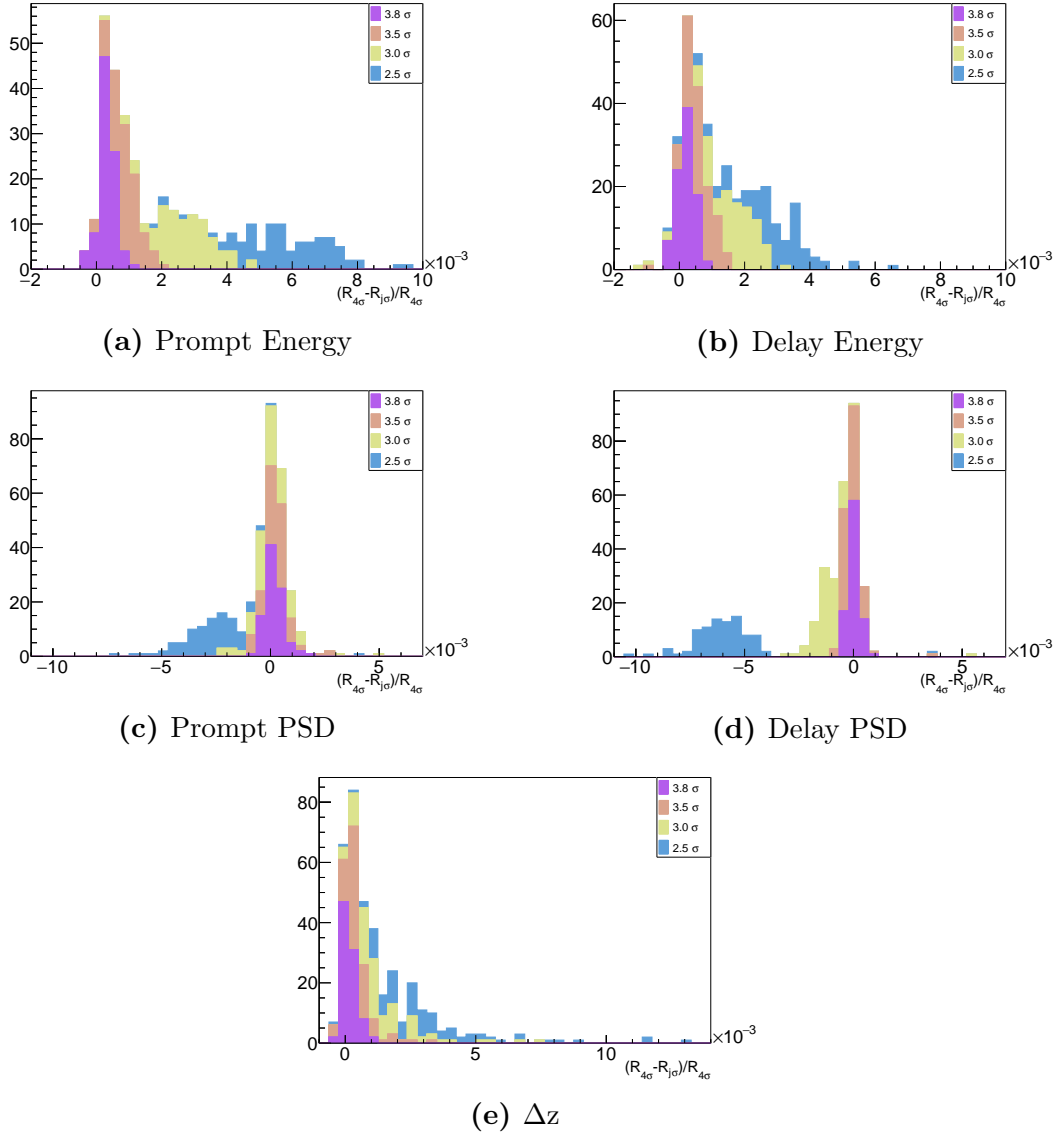


**Figure 5.36:** Pictured here are distributions created by calculating for each cell the difference between the rate using a given  $\sigma$  cut and the rate using a  $4\sigma$  cut normalized by the rate using a  $4\sigma$  cut for data.

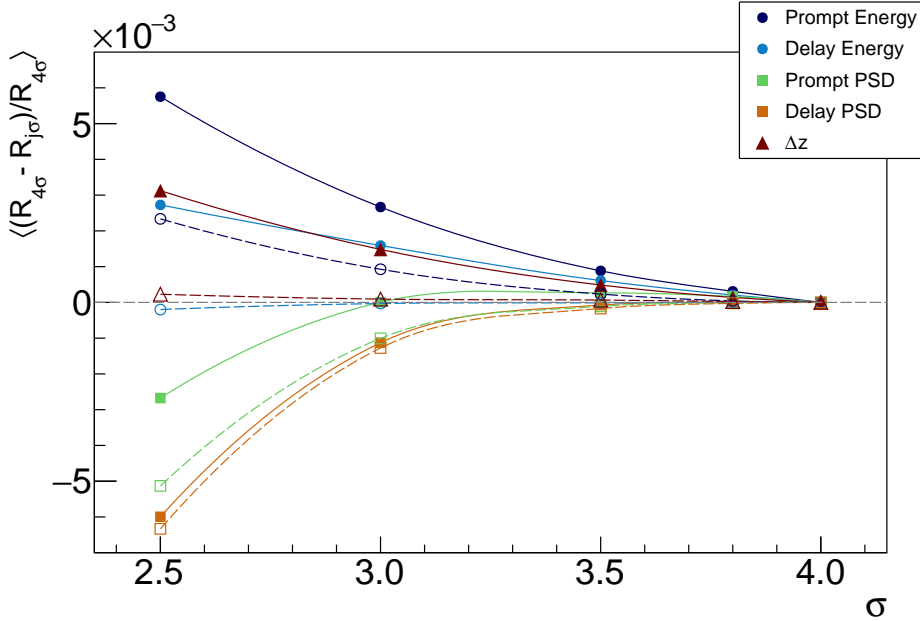


**Figure 5.37:** The mean of the distributions shown in Figure 5.36. Solid lines: data. Dashed lines: simulation. Connecting lines are not fits; only meant to help guide the eye of the reader.

### 5.3.8.2 Other Coincident Alphas

There are two known event types with coincident alphas that occur in the PROSPECT AD that could contaminate the RnPo selection group. The first is an  $\alpha$ - $\alpha$  coincidence in the  $^{232}\text{Th}$  chain (the chain responsible for  $^{212}\text{Bi} \rightarrow ^{212}\text{Po}$  (BiPo) events):  $^{220}\text{Rn} \rightarrow ^{216}\text{Po} \rightarrow ^{212}\text{Pb}$ . As listed in Table 5.10, the energy of these alphas fall in the selection range of the  $^{227}\text{Ac}$  RnPo's (0.48/0.61-1.18 MeV) making it possible for them to be selected and not correctly background subtracted.

The other possible event is the triple alpha decay in the  $^{227}\text{Ac}$  chain:  $^{223}\text{Ra} \rightarrow ^{219}\text{Rn} \rightarrow ^{215}\text{Po} \rightarrow ^{211}\text{Pb}$ . Choosing a background subtraction window that occurs before a given selected delay event (Po) helps to get rid of most of this contamination, but the rate of remaining events can be calculated.

Using the information found in Table 5.10 and the time windows chosen for the  $^{227}\text{Ac}$  RnPo selection it is possible to calculate the amount of contamination that is expected from the other alpha coincidences. Starting with the  $^{232}\text{Th}$  RnPo's, the fraction of  $^{220}\text{Rn} \rightarrow ^{216}\text{Po}$  alphas that are selected as ‘true’  $^{227}\text{Ac}$  events, based on energy and time cuts, is  $\sim 0.0061$ . If the rate of these events is approximated to

Isotope	$t_{1/2}$ [ms]	E [MeV]	QE [MeVee]	$1\sigma$ width [MeVee] (5% res.)
$^{220}\text{Rn}$	55600	6.2881	0.5942	0.0412
$^{216}\text{Po}$	145	6.7783	0.6776	0.0412
$^{223}\text{Ra}$	$9.88 \times 10^8$	5.7162	0.5031	0.0355
$^{219}\text{Rn}$	3860	6.8191	0.6847	0.0414
$^{215}\text{Po}$	1.781	7.3861	0.7876	0.0444

**Table 5.10:** Dominant  $\alpha$  energies for coincident  $\alpha$  event chains that could contaminate the  $^{227}\text{Ac}$  RnPo signal. Also given are the quenched energies (QE) and  $1\sigma$  widths based on a 5% energy resolution.

be 0.085 Hz (based on a BiPo rate of 0.0547 Hz [86]) then the rate of selection is  $\sim 0.00052$  Hz. If we approximate a total  $^{227}\text{Ac}$  rate of 0.29 Hz, and therefore a rate of 0.24 Hz in the 0.5 - 12.845 ms time window used for selection, then the  $^{232}\text{Th}$  RnPo's will make up  $\sim 0.22\%$  of the  $^{227}\text{Ac}$  RnPo signal selection in the selection time window. Therefore, a systematic error of 0.22% will be applied.

The triple alpha in the  $^{227}\text{Ac}$  chain contributes much less to the RnPo signal selection. Due to the nature of the background subtraction the probability that  $^{223}\text{Ra} \rightarrow ^{219}\text{Rn}$  coincident events pass both the energy cuts and the subtraction is 0.00083%. No systematic error will be applied for these event types.

See Table 5.11 for a summary of the energy and time cut efficiencies for both coincident alpha event types.

Prompt	Delay	$t_{1/2}$ [ms]	Energy Cut Eff.	Time Cut Eff.	Rate [mHz]
$^{220}\text{Rn}$	$^{216}\text{Po}$	145	0.925	0.0066	0.52
$^{223}\text{Ra}$	$^{219}\text{Rn}$	3860	0.815	0.000010	0.0021

**Table 5.11:** Energy and time cut efficiencies and resulting rates (assuming an  $^{227}\text{Ac}$  rate of 240 mHz) for both coincident  $\alpha$  event chains that could contribute to contamination of the  $^{227}\text{Ac}$  RnPo signal selection.

### 5.3.9 $^{227}\text{Ac}$ Rates per Baseline

The original goal of adding  $^{227}\text{Ac}$  to the PROSPECT detector was to measure relative volume differences and apply these corrections to the oscillation analysis. The oscillation analysis is carried out by dividing the detector into baselines, or distances from the reactor core, and comparing the measured spectra between baselines. A

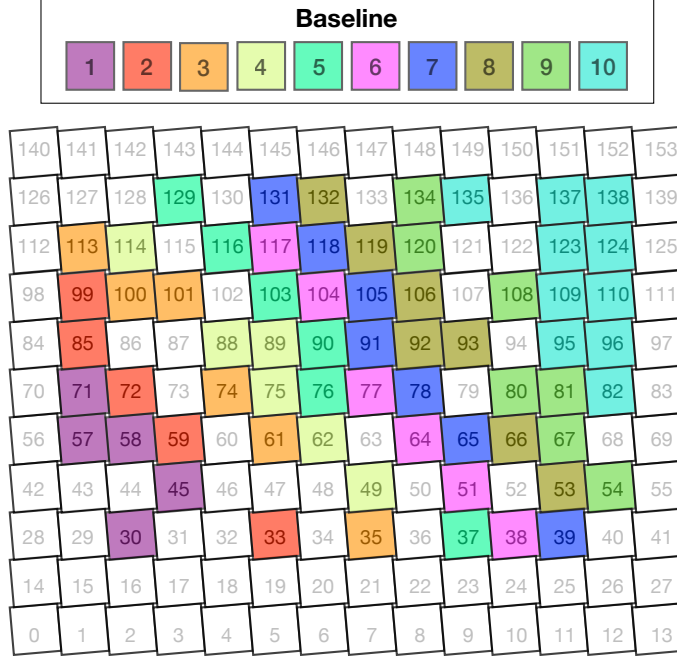


**Figure 5.38:** The PROSPECT AD divided into 10 baselines, where baseline 1 is closest to the reactor. Segments in white are either fiducial segments or were turned off.

similar process can be done for the  $^{227}\text{Ac}$  rates, and then corrections can be applied to the number of IBD counts versus baseline based on the  $^{227}\text{Ac}$  results.

The detector was divided into 10 individual baselines, where baseline 1 is closest to the reactor core. Figure 5.38 shows the configuration of baselines that was chosen for this data set. The  $^{227}\text{Ac}$  rate measured for each segment was then averaged over each baseline (error-weighted) and then plotted relative to the average rate in the first baseline. The results of this can be seen in Figure 5.39. Note that the rates used in this part of the analysis were measured using an additional  $z$ -fiducial cut of  $-448 < z < 448$  mm, in order to use the same fiducial volume as the oscillation analysis.

It can be seen that the average rates vary less than  $\sim 0.5\%$  over all baselines. As the oscillation analysis for this data set is not yet completed, these results cannot currently be applied as corrections to the IBD rate versus baseline. Instead, the same analysis described in this chapter was applied to the data set used for the published oscillation results and corrections were applied accordingly and are described in the next chapter.

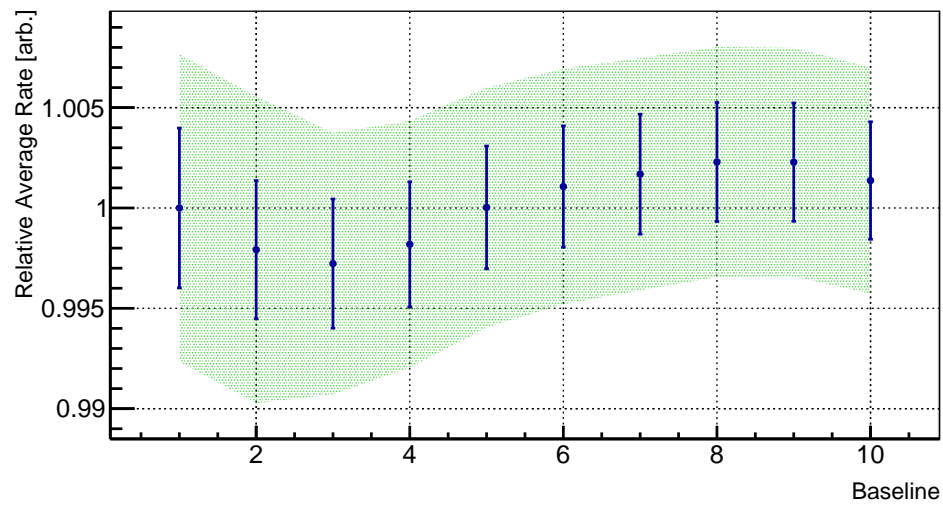


**Figure 5.39:** The  $^{227}\text{Ac}$  rate for fiducial  $z$  volume averaged over each of the 10 defined baselines and relative to the first baseline. Error bars are statistical, systematic errors are shown as the shaded region.

# CHAPTER 6

## NEUTRINO OSCILLATION IN THE PROSPECT AD

### 6.1 Detecting Antineutrinos

PROSPECT detects  $\bar{\nu}_e$ 's via the inverse beta decay reaction (IBD):



A reactor  $\bar{\nu}_e$  will interact with a proton in the  ${}^6\text{Li}$ -LS, producing a positron and a neutron. The positron will quickly lose energy and annihilate with an electron, producing two 511 keV  $\gamma$ -rays. This is the prompt signal.

Concurrently, the neutron will thermalize by scattering off of protons in the scintillator until it captures on  ${}^6\text{Li}$  ( $\sim 80\%$  of the time) or H ( $\sim 20\%$  of the time). The neutron capture on  ${}^6\text{Li}$  (nLi) produces a tritium and an alpha with energies 2.05 MeV and 2.75 MeV respectively. These two products will immediately scintillate, and produce a quenched signal of  $\sim 0.55$  MeVee. This is the delayed signal. Figure 6.1 illustrates this process in the PROSPECT LiLS.

The neutron capture on  ${}^6\text{Li}$  takes  $\sim 40\mu\text{s}$ , providing a time separation between the prompt and delayed signals. Making use of the time coincident, PSD, and energy cuts, PROSPECT can identify  $\bar{\nu}_e$  events above background.

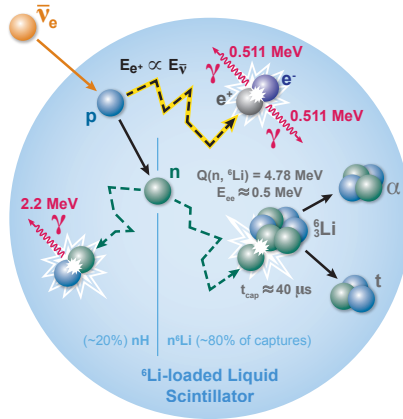


**Figure 6.1:** Schematic of the IBD interaction in the PROSPECT AD.

## 6.2 IBD Event Selection

### 6.2.1 Cuts

A selection of energy, PSD, and time cuts, along with specified event vetos are utilized to identify IBD signals and reduce background. These are:

- Prompt Cluster Size:  $\geq 1$
- Prompt PSD: All pulses must have PSD that is  $< 3\sigma$  from the gamma-like PSD band mean
- Prompt Energy: No cut, but only clusters with a total energy of  $0.8 < E_{\text{rec}} < 7.2 \text{ MeV}$  are used in the oscillation analysis
- Delayed Cluster Size: Single pulse
- Delayed PSD: All pulses must have PSD that is  $> 3.6\sigma$  from the gamma-like PSD band mean
- Delayed Energy:  $0.46 < E_{\text{rec}} < 0.60 \text{ MeV}$
- Time Correlation:  $\Delta t = (1, 120) \mu\text{s}$
- Prompt-Delayed Distance:  $\Delta z < 18 \text{ cm}$  for coincidences in the same segment;  $\Delta z < 14 \text{ cm}$  for coincidences in horizontally/vertically adjacent segments

- Pileup Veto: Applied to both prompt and delayed clusters, if the candidate cluster is preceded by another cluster in a window of  $< 800$  ns, the candidate cluster is vetoed
- Shower Veto: Veto delayed clusters that exist in a  $(0,100)$   $\mu\text{s}$  window around cosmic muon clusters ( $E_{\text{rec}} > 15$  MeV); Veto delayed clusters that exist within  $(-200,+200)$   $\mu\text{s}$  of events with  $\text{PSD} > 3\sigma$  from the gamma-like PSD band mean and  $E > 0.25$  MeV
- Fiducialization: Reject events in which a prompt or delayed event occurs in the outer ring of segments; reject events that occur outside of  $z = (-448, 448)$  mm

For an example of how the PSD and energy cuts look in PSD versus energy space for prompt events correlated with a delayed neutron capture see Figure 6.2.

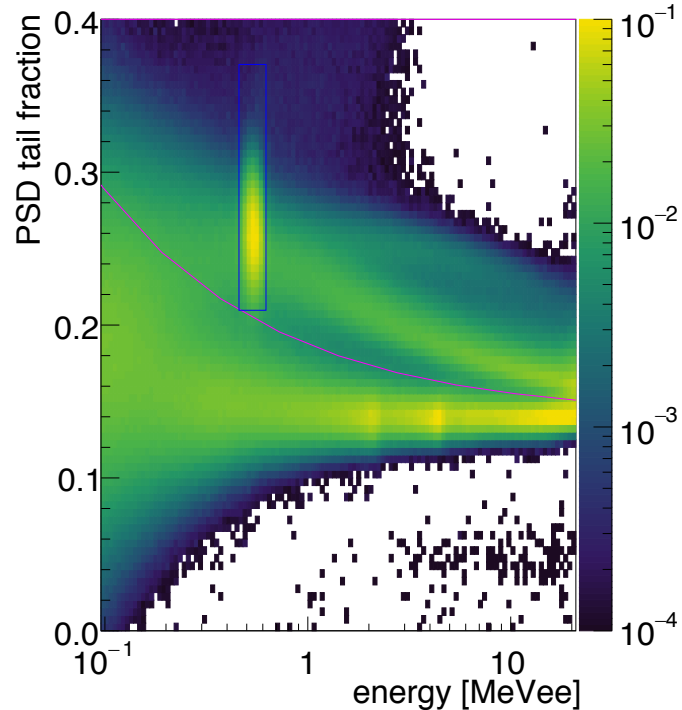


**Figure 6.2:** PSD versus energy distribution for prompt events correlated with a delayed neutron capture on  ${}^6\text{Li}$ . The cuts used for identifying  $n\text{Li}$  events is represented by the blue rectangle. The upper limit of the cut used for identifying electron-like signals is shown as the pink curve.

## 6.2.2 Backgrounds

The two primary backgrounds to the IBD signal are time-correlated cosmogenic neutron events and accidental coincidences of ambient  $\gamma$ -rays and  $nLi$  captures. Cosmic muons moving through the lead shielding can create multiple neutrons that may be selected as delayed events. The shower veto helps to reduce this background, introducing a dead-time that varies between 5.5% and 6.9% for reactor off and on times respectively. Along with this veto, the IBD selection is applied to reactor off data and the resulting distributions are subtracted from the reactor on results.

Accidental coincidences are handled by selecting prompt-delay pairs with  $\Delta t = (-12, -2)$  ms. This provides a high statistics sample of events that are scaled to match the correlated time window and then subtracted from the correlated events. This is done for both reactor on and off data sets.

Figure 6.3 shows the prompt energy spectra for 24 hours both of reactor on and off data after applying all cuts and accidental background subtraction. Prominent peaks at 2.2 MeV and 4.4 MeV exist in both reactor on and off data. Cosmogenic muons can create several neutrons. One of these will capture on hydrogen ( $nH$ ), producing a 2.2 MeV  $\gamma$ , which will be followed by another neutron capturing on  ${}^6Li$ . These time-coincident events are reduced by the shower veto, but not completely removed.

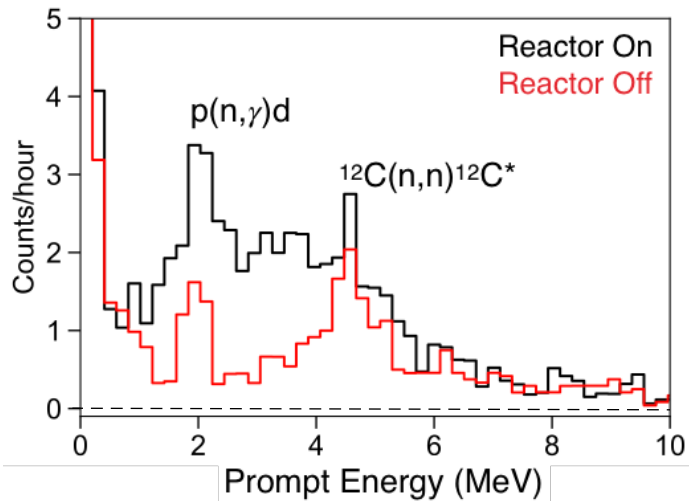


**Figure 6.3:** The prompt energy spectra, after background subtraction, of IBD events for 24 hours of both reactor on and off data. Prominent peaks at 2.2 MeV and 4.4 MeV are due to neutron captures on Hydrogen and inelastic neutron scatters on  ${}^{12}C$  respectively.

Fast neutrons will also inelastically scatter off of  $^{12}\text{C}$  in the scintillator causing the reaction:



As  $^{12}\text{C}^*$  de-excites it will release a 4.4 MeV photon, while the scattered neutron thermalizes and captures on  $^6\text{Li}$ , mimicking the IBD signal.

### 6.2.3 Atmospheric Correction

Cosmogenic rates vary according to changes in pressure, therefore, a scaling factor for this effect needs to be introduced in order to perform accurate background subtraction. To determine the size of this correction fast neutron events with a prompt proton recoil and a delayed nLi capture (FN+nLi) were studied. The prompt event was required to have  $\text{PSD} > 3\sigma$  from the gamma-like PSD band mean, otherwise all other cuts used were the same as the ones used for IBD selection.

Figure 6.4 shows the rate of these coincident events and pressure versus time, along with rate versus pressure. It can be seen that the event rate and pressure are inversely correlated. The rate of FN+nLi events as a function of pressure was fit with a linear function and the results of the fit were used to define the atmospheric correction,  $k_p$ , according to

$$k_p = \frac{m \cdot \bar{p}_{on} + c}{m \cdot \bar{p}_{off} + c} \quad (6.3)$$

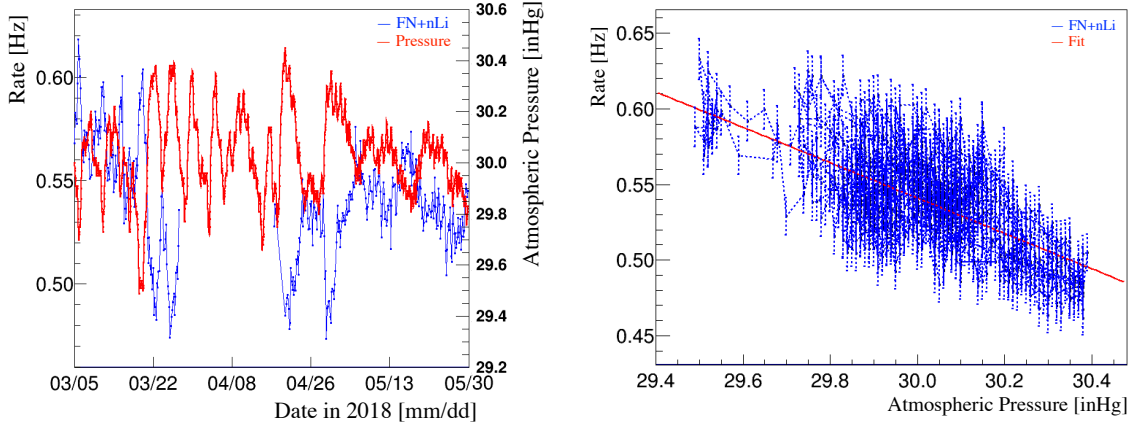


**Figure 6.4:** (Left) The rate of fast neutron and nLi capture coincidences (blue) and pressure (red) versus time. (Right) FN+nLi rates as a function of pressure with a linear fit. [87]

where  $m$  and  $c$  are the slope and y-intercept of the fit and  $\bar{p}_{on(off)}$  is the average pressure during reactor on (off). For this analysis the atmospheric correction was found to be  $< 1\%$ .

### 6.2.4 Background Subtraction

To obtain the final measured IBD events the correlated and accidental events are subtracted for both reactor on and off time periods. Due to differences in reactor on and off exposure time, as well as differences between accidental and coincidental acceptance time windows, accidental and reactor off events have to be correctly scaled. Therefore, the number of IBD candidates,  $N_{IBD}$ , is measured as:

$$\begin{aligned} N_{IBD} &= N_{corr-acc,on} - k_p \cdot N_{corr-acc,off} \\ &= N_{corr,on} - \frac{\Delta t_{corr}}{\Delta t_{acc}} N_{acc,on} - k_p \frac{t_{on}}{t_{off}} \left( N_{corr,off} - \frac{\Delta t_{corr}}{\Delta t_{acc}} N_{acc,off} \right) \end{aligned} \quad (6.4)$$

## 6.3 Data Set

The dataset used in this analysis consists of 30.26 (33) reactor on and 26.19 (28) reactor off effective (calendar) days. The rate of correlated and accidental rates for each of these periods are listed in Table 6.1. A total of 25461 IBD events were detected (771/day), with a signal-to-background ratio of 2.20 and 1.32 for accidental and correlated background, respectively. The correlated and accidental rates per day as a function of time for events in the prompt energy region (0.8, 7.2) MeV can be seen in Figure 6.5.

Due to current instabilities observed in some PMT's during the data-taking period 31 segments were excluded in this analysis: (0, 1, 2, 3, 4, 5, 6, 9, 10, 11, 12, 13, 18, 21, 23, 24, 27, 32, 34, 40, 44, 52, 68, 79, 86, 102, 115, 122, 127, 130, 139). Two segments not in the outer shell were also added to the non-fiducial volume due to high background rates: (25, 26). These two segments exist in a corner of the detector that does not sit on the monolith and therefore they see many  $\gamma$ -rays from beam lines under the floor.

Reactor	Event Type	Time [days]	Counts
On	Correlated + Accidental	30.26	$56378 \pm 1708$
	Accidental (scaled)		$11580 \pm 12$
	Correlated		$44797 \pm 238$
Off	Correlated + Accidental (scaled)	26.19	$20262 \pm 153$
	Accidental (scaled)		$925 \pm 4$
	Correlated (scaled)		$19337 \pm 153$
	Signal		$25461 \pm 238$ (771/day)

**Table 6.1:** The total number of correlated and accidental events in the prompt energy region (0.8, 7.2) MeV for reactor on and off periods. Time refers to exposure time.

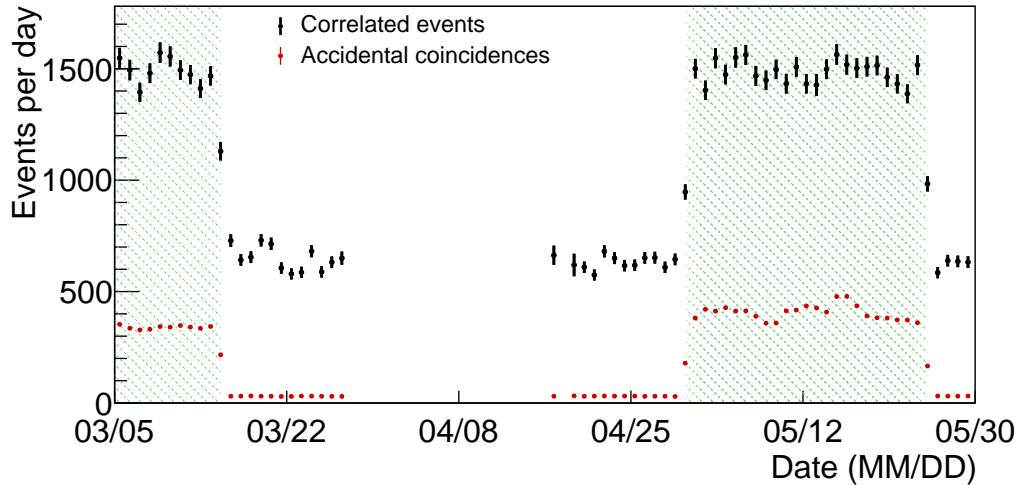


**Figure 6.5:** Accidentals-subtracted IBD candidate event rate per day (black) and measured accidental rate (red) as a function of time. IBD candidate rates are corrected for dead time and exposure time. The shaded regions (green) are reactor on periods. Errors are statistical. The gap in data corresponds to a detector maintenance period.

## 6.4 IBD Rates versus Baseline

IBD rates as a function of distance from the reactor,  $r$ , are expected to fall as  $1/r^2$ . The fiducial volume of the reactor was divided into 14 baselines (see Figure 5.29) and the IBD rate at each baseline, scaled by active mass and relative efficiency, is plotted in Figure 6.7. The data shows good agreement with a fit of the form  $C/r^2$ , producing

a  $\chi^2/NDF = 10.89/13$ , confirming the inverse square law behavior. It can be noted that there is  $\sim 40\%$  decrease in flux from the front to the back of the detector.

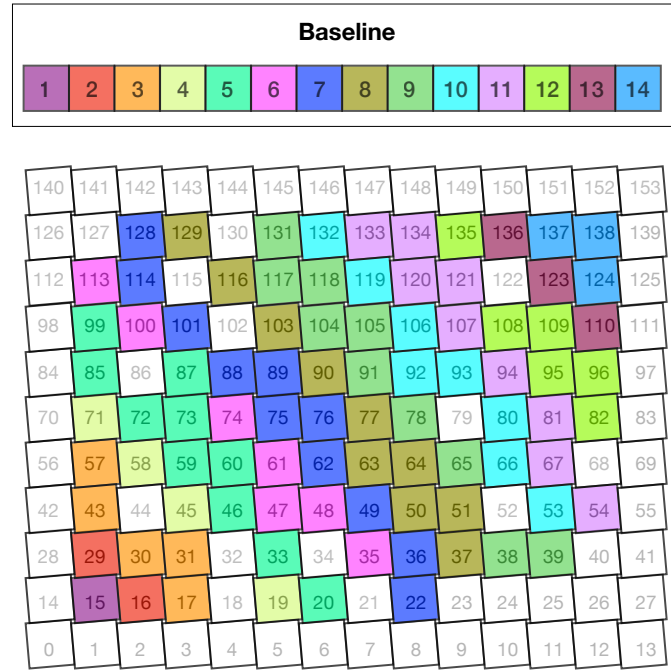


**Figure 6.6:** The PROSPECT AD divided into 14 baselines, where baseline 1 is closest to the reactor. Segments in white are either fiducial segments or were turned off.

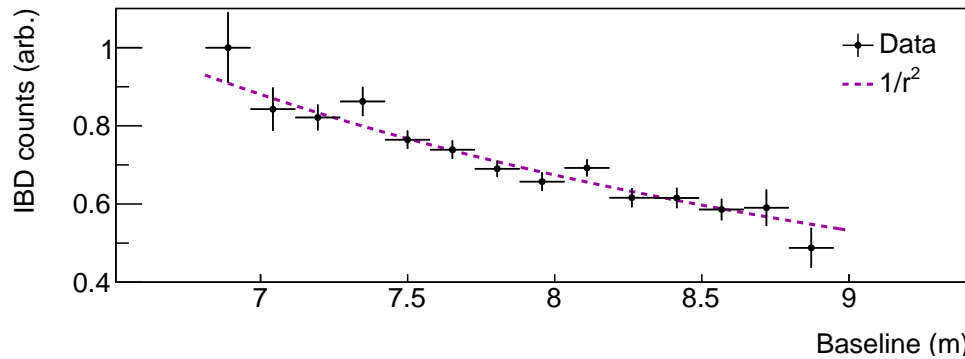


**Figure 6.7:** Background subtracted IBD event rate as a function of distance from the reactor center binned into 14 unique baselines. Data is fit with  $C/r^2$  (dashed, magenta) and produces a  $\chi^2/NDF = 10.89/13$ . Errors are statistical.

As was described in Section 5.3.9, the  $^{227}\text{Ac}$  rate per segment can be used to correct the IBD event rate as a function of baseline for any observed volume variation

effects. The average measured  $^{227}\text{Ac}$  rate per baseline, relative to the first baseline, can be seen in Figure 6.8. Unlike the data set used in the previous chapter, the data for this oscillation analysis is statistics limited, accounting for the much larger error bars than were present in Figure 5.39.

These relative rates were then applied as corrections to the IBD event rate versus baseline, the results of which are shown in Figure 6.9. This distribution was then fit with a  $1/r^2$  function, producing a  $\chi^2/NDF = 8.351/13$ .

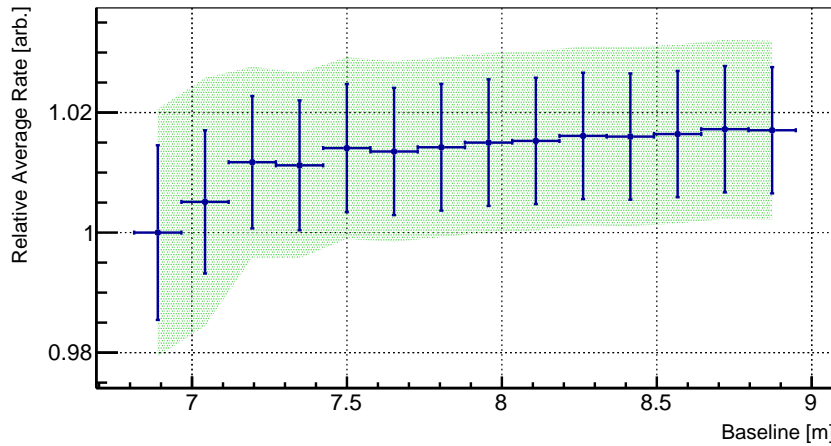


**Figure 6.8:** The  $^{227}\text{Ac}$  rate (for fiducial  $z$ ) averaged over each of the 14 defined baselines, plotted relative to the first baseline. Error bars are statistical, systematic errors are shown as the shaded region.

## 6.5 Oscillation Search

The construction of PROSPECT as a segmented detector allows the comparison of  $\bar{\nu}_e$  spectrum between baselines rather than to a calculated reactor  $\bar{\nu}_e$  spectrum. Therefore, the search for a sterile neutrino was carried out by comparing the measured IBD spectrum as a function of baseline (the L vs E spectrum) to a predicted L vs E spectrum constructed using MC simulations. The MC unoscillated prompt spectrum,  $P_{null}(L, E_p)$ , is described by:

$$P_{null}(L, E_p) = W_{th} \cdot S(E_\nu) / 4\pi L^2 \cdot t \cdot \epsilon_D(L, E_\nu, E_p) \cdot \rho_P V_D \cdot \sigma(E) \quad (6.5)$$

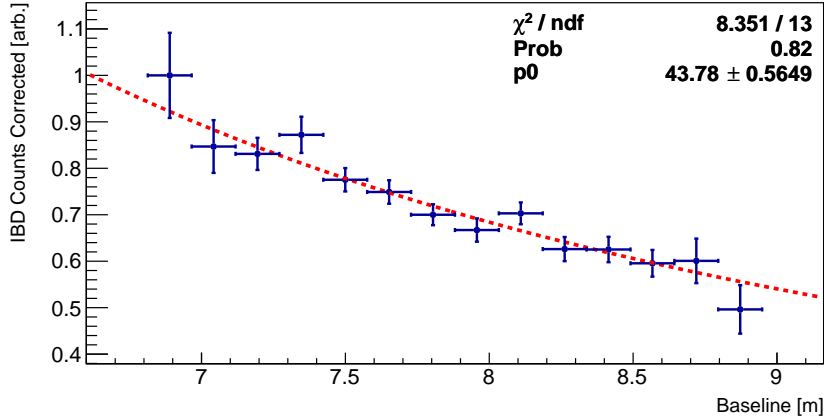


**Figure 6.9:** Background subtracted IBD event rate as a function of distance from the reactor center binned into 14 unique baselines, corrected for the measured  $^{227}\text{Ac}$  rates in Figure 6.8.

where  $W_{th}$  is the thermal power of the reactor,  $S(E_\nu)$  is the  $\bar{\nu}_e$  spectrum at energy E,  $L$  is the given baseline,  $t$  is the exposure time,  $\rho_P$  is the proton density of the LS,  $V_D$  is the active volume of the detector,  $\sigma(E)$  is the IBD cross-section, and  $\epsilon_D(L, E_\nu, E_p)$  is the detection efficiency and encompasses all detector effects. This prompt spectrum is divided into 6 baseline (position) bins and 16 energy bins to create the L vs E spectra.

To compare the spectra at different baselines a covariance-matrix based  $\chi^2$  test-statistic was built according to:

$$\chi^2 = \Delta^T \mathbf{V}_{\text{tot}}^{-1} \Delta \quad (6.6)$$

where  $\mathbf{V}_{\text{tot}}$  is a covariance matrix constructed from the statistical and systematic uncertainties.  $\Delta$  is a 96-element vector representing the relative agreement between the measured ( $M_{l,e}$ ) and predicted ( $P_{l,e}$ ) L vs E spectra in the  $l^{th}$  baseline bin and  $e^{th}$  energy bin:

$$\Delta_{l,e} = M_{l,e} - M_e \frac{P_{l,e}}{P_e}. \quad (6.7)$$

$M_e$  and  $P_e$  are the detector-wide spectrum rates in the  $e^{th}$  energy bin and are defined as

$$M_e = \sum_{l=1}^6 M_{l,e} \text{ and } P_e = \sum_{l=1}^6 P_{l,e}. \quad (6.8)$$

The predicted L vs E spectrum is modeled to include sterile neutrino oscillations as

$$P_{l,e}(\Delta m_{14}^2, \theta_{14}) = P_{l,e}(0, 0) \left( 1 - \sin^2 2\theta_{14} \sin^2 \left( 1.27 \Delta m_{14}^2 \frac{L}{E} \right) \right) \quad (6.9)$$

where  $m_{14}^2$  and  $\theta_{14}$  describe mixing between one active neutrino flavor state and one sterile neutrino state. The search for sterile neutrino oscillations is then carried out by minimizing the  $\chi^2$  in Equation 6.6 by varying the parameters  $m_{14}^2$  and  $\theta_{14}$ .

### 6.5.1 Uncertainties

Statistical and systematic uncertainties are included in the form of covariance matrices  $\mathbf{V}_{\text{stat}}$  and  $\mathbf{V}_{\text{syst}}$ . The statistical uncertainties are directly calculated from data using Poisson statistics, resulting in an uncorrelated, diagonal matrix. Since the predicted L vs E spectra are normalized by the baseline-integrated spectra rates ( $M_e$ ), as shown in Equation 6.7, off-diagonal terms need to be added to take into account the correlation between  $M_{l,e}$  and  $M_e$ . Therefore, the full statistical covariance matrix is included as:

$$V_{\text{stat},l,e} = \sigma_{\text{stat},l,e}^2 \left( 1 - 2 \frac{M_{l,e}}{M_e} \right) + \sigma_{\text{stat},e}^2 \left( \frac{M_{l,e}}{M_e} \right)^2 \quad (6.10)$$

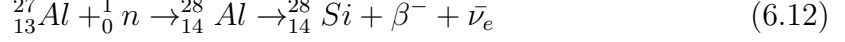
Beyond this, additional off-diagonal terms are included to account for correlations between position bins with the same energy arising from the use of  $M_e$ . These corrections were estimated by studying Monte Carlo toy's and extracting the resulting covariance matrix.

For each systematic uncertainty a normalized covariance matrix is produced using toy MC datasets and varying each systematic by  $1\sigma$ . Assuming that all errors are Gaussian, the total covariance matrix is then calculated as the sum of all statistical and systematic matrices as

$$\mathbf{V}_{\text{tot}} = \mathbf{V}_{\text{stat}} + \sum_i \mathbf{V}_{\text{syst},i}. \quad (6.11)$$

In addition to uncertainties from statistics and detector response, uncertainties about the reactor  $\bar{\nu}_e$  flux have to be taken into account. The MC  $\bar{\nu}_e$  spectrum is generated using the Huber  $^{235}\text{U}$  flux model [49] and the Vogel-Beacom model for IBD cross section [51], not taking into account  $\bar{\nu}_e$ 's that may be generated via processes other than by  $^{235}\text{U}$  fission. The fuel used in the HFIR reactor core is  $\text{U}_3\text{O}_8\text{-Al}$ , allowing

the possibility of  $\bar{\nu}_e$  production through neutron activation of the  $^{27}\text{Al}$ :



$^{28}\text{Al}$  has a half-life of 2.245 minutes with an endpoint energy of 2.86 MeV [82], producing low energy  $\bar{\nu}_e$ 's. This process was modeled [88], and aluminum corrections were estimated to contribute  $\sim 0.85\%$  over the full dataset, all with energies below 3 MeV as seen in Figure 6.10 [89].

Furthermore, a correction is needed for  $\bar{\nu}_e$ 's produced by long-lived fission isotopes (non-equilibrium isotopes). The ILL beta-spectrum measurements [43, 44, 45], which are used in the Huber spectrum, are based on  $\sim 1$ -day long measurements, compared to an average HFIR reactor cycle, which is about 24 days. As there are a number of long-lived isotopes, their  $\bar{\nu}_e$  contributions were not included in the Huber model but do contribute the spectrum measured by PROSPECT. Extrapolating from predictions made in [48], non-equilibrium corrections were found to be  $\sim 0.5\%$  over the full dataset, with most contributions below 4 MeV as seen in Figure 6.11 [90].

Including both the aluminum and non-equilibrium contributions to the  $\bar{\nu}_e$  spectrum results in a 1.3% increase in the model spectrum, shown in Figure 6.12. For a summary of all systematic uncertainties see Table 6.2.

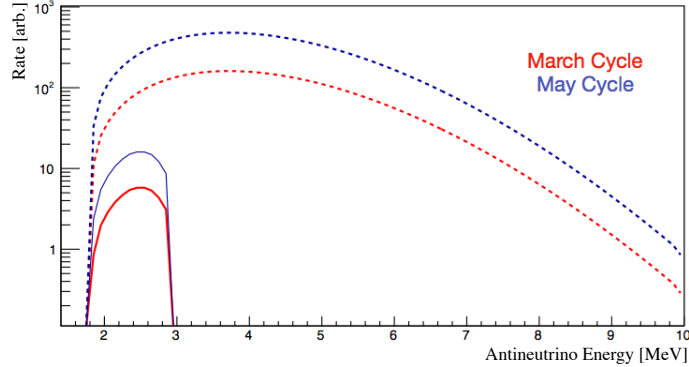


**Figure 6.10:**  $\bar{\nu}_e$  spectrum from  $^{28}\text{Al}$   $\beta$ -decay (solid) and  $^{235}\text{U}$  fission (dashed) for both reactor on cycles used in this analysis [89]

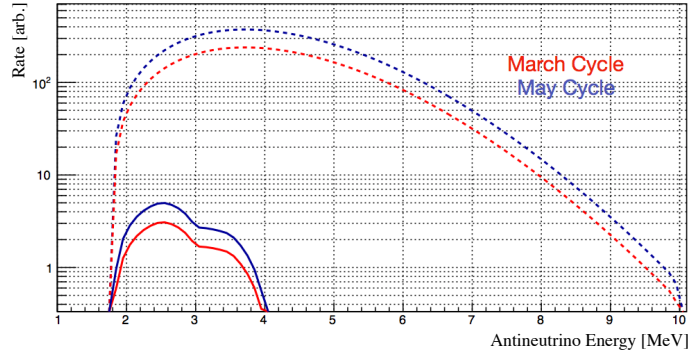


**Figure 6.11:**  $\bar{\nu}_e$  spectrum from non-equilibrium isotopes (solid) and  $^{235}\text{U}$  fission (dashed) for both reactor on cycles uses in this analysis [90].

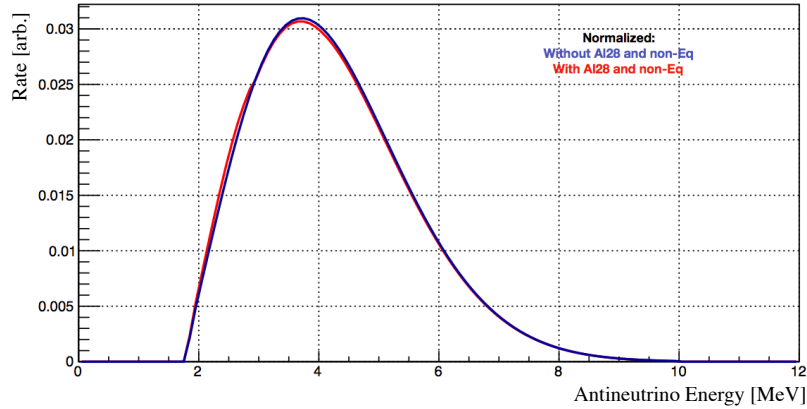


**Figure 6.12:** The normalized  $\bar{\nu}_e$  as predicted by Huber+Vogel-Beacom with and without the aluminum + non-equilibrium corrections (1.3%).

Parameter	Nominal Value	Uncertainty
Background normalization	-	5%
Uncorrelated (n,H) to (n,C*) peak	-	5%
Background scaling	-	0.2%
Birks' nonlinearity ( $k_{B1}$ )	0.100 mm/MeV	0.012 mm/MeV
Cherenkov nonlinearity ( $k_c$ )	51%	4%
Energy scale ( $A$ )	1	0.7%
Energy resolution	4.45%	0.2%
Energy loss	-	30 keV
Uncorrelated IBD efficiency	-	5%
Uncorrelated volume	-	per segment
Uncorrelated energy resolution	4.45%	0.2%
Uncorrelated energy loss	-	30 keV
Baseline uncertainty	793.2 cm	10 cm
$^{28}\text{Al}$ spectrum correction	-	100%
Non-equilibrium spectrum correction	-	100%

**Table 6.2:** Summary of systematic uncertainties that were used to generate the covariance matrices used in the oscillation analysis. Uncertainties are correlated unless otherwise noted.

### 6.5.2 Confidence Interval Assignment

The frequentist approach proposed by Feldman and Cousins [91] was used to assign confidence intervals for the oscillation analysis. This was done by defining a critical  $\Delta\chi^2_C$  value for each point on the  $\sin^2 2\theta_{14} - \Delta m_{14}^2$  grid for a chosen confidence level.

For each point on the  $\sin^2 2\theta_{14} - \Delta m_{14}^2$  grid 1000 oscillated MC toy datasets are generated, fluctuating the statistical and systematic uncertainties. For each of these toys a minimum  $\chi^2_{min}$  is found by applying Equation 6.6. Then, a  $\Delta\chi^2$  is defined as

$$\Delta\chi^2 = \chi^2_{min,true} - \chi^2_{min,best-fit} \quad (6.13)$$

where  $\chi^2_{min,true}$  and  $\chi^2_{min,best-fit}$  are the  $\chi^2_{min}$  for the true oscillation parameters and best-fit parameters for that given toy.

Then, for each point on the grid a  $\Delta\chi^2_C$  was defined for a given confidence level  $\alpha$

such that

$$\frac{\sum_0^{\Delta\chi_C^2} P(\Delta\chi^2)}{\sum_0^{\infty} P(\Delta\chi^2)} = \alpha \quad (6.14)$$

where  $P(\Delta\chi^2)$  is the distribution of  $\Delta\chi^2$  for all toys for the given grid point. See Figure 6.13 for the distribution of  $\Delta\chi_C^2$  values for  $\alpha = 95\%$ . A point on the  $\sin^2 2\theta_{14} - \Delta m_{14}^2$  grid is said to be excluded by data at a  $\alpha$  confidence level if  $\Delta\chi_{data}^2 > \Delta\chi_C^2$  where  $\Delta\chi_{data}^2$  is the difference between the data and best-fit minimized  $\chi^2$ .

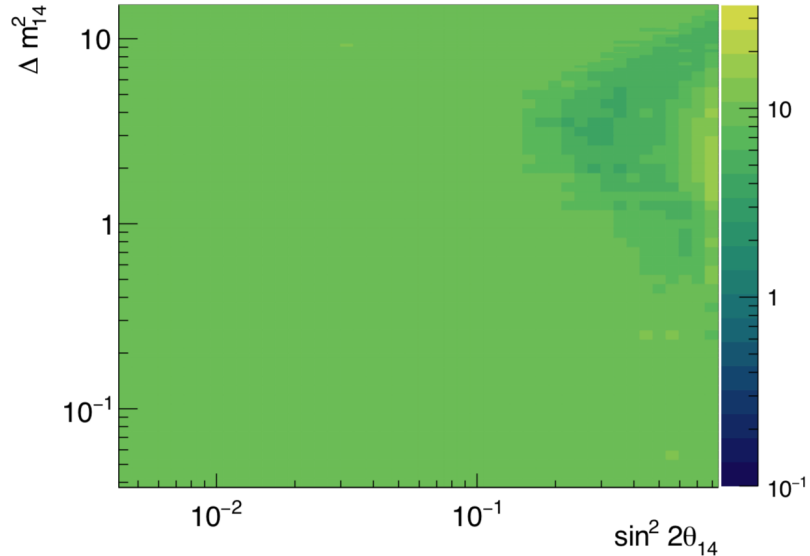


**Figure 6.13:** Critical  $\Delta\chi_C^2$  values for a 95% confidence level [92].

### 6.5.3 Results

For each baseline bin the ratio between the measured IBD prompt spectrum ( $M_{l,e}$ ) to the total spectrum, normalized by the no-oscillation prediction (null hypothesis), ( $M_e \frac{P_{l,e}}{P_e}$ ) for data, no-oscillation prediction, and the best-fit Reactor Antineutrino Anomaly oscillation parameters is shown in Figure 6.14. No significant deviations from the no-oscillation prediction are observed throughout the energy spectra at all chosen baselines.

The level of agreement between data and the null hypothesis can be quantified using the  $\chi^2$  in Equation 6.6. At  $\theta_{14} = 0$ , the  $\chi^2/NDF = 61.9/80$ , indicating good agreement between the data and null hypothesis. Allowing oscillations, a global minimum is found at  $\Delta m_{41}^2 = 0.5\text{eV}^2$  and  $\sin^2 2\theta_{14} = 0.35$ , with  $\chi^2/NDF = 57.9/78$ .

A  $p$  value for these results is generated by comparing the data  $\Delta\chi^2$  values to the  $\Delta\chi_C^2$  distributions. Comparison of the null and sterile neutrino hypotheses results in a  $p$ -value of 0.58, demonstrating that the PROSPECT data is compatible with the standard 3-flavor neutrino mixing framework.

Figure 6.15 shows the 95% confidence level exclusion contour and expected sensitivity from the 33 days of reactor-on PROSPECT data. The data-set used in this analysis excludes large portions of the Reactor Antineutrino Anomaly (RAA) allowed region and disfavors the RAA best-fit point at  $2\sigma$  confidence level with a  $p$ -value of 0.013.

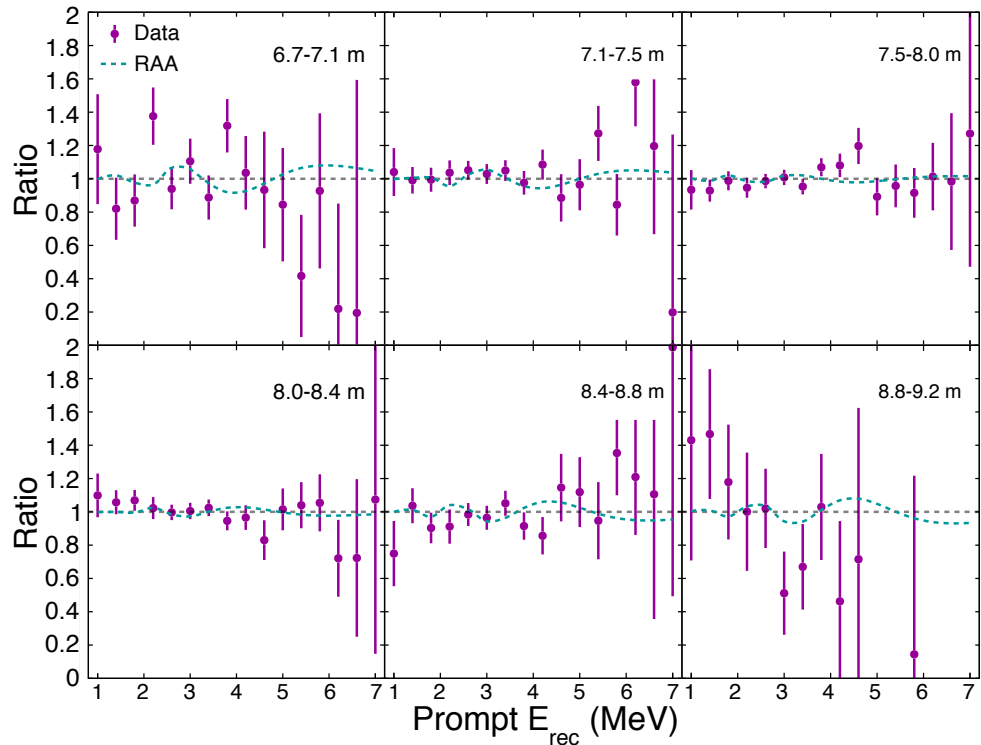


**Figure 6.14:** Ratio of the measured IBD prompt energy spectra to the predicted baseline-integrated spectrum, for 6 baseline bins. Error bars include statistical and systematic uncertainties. Also shown are the no-oscillation expectation (gray, dashed) and an oscillated expectation based on the best fit Reactor Antineutrino Anomaly parameters (teal, dashed). [1]

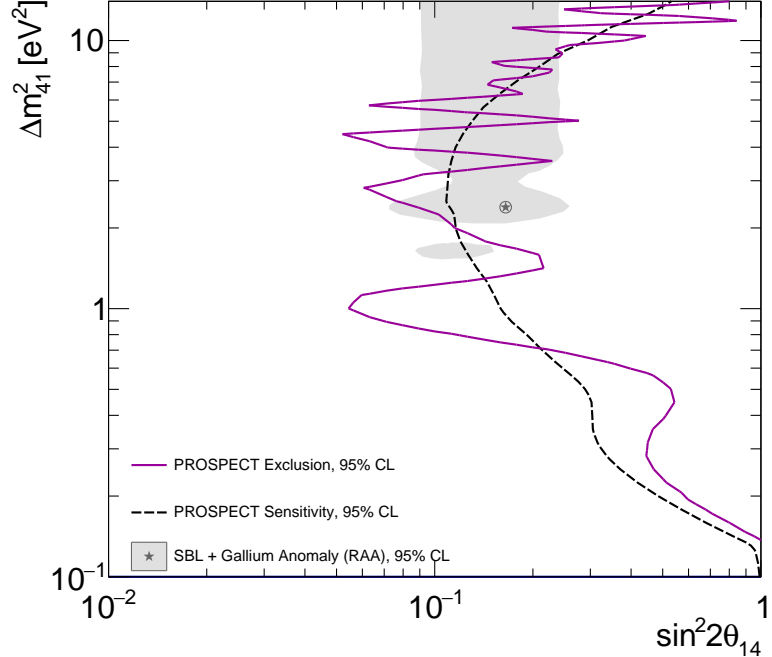


**Figure 6.15:** Sensitivity and 95% confidence level sterile neutrino oscillation exclusion contour from the 33 day reactor-on PROSPECT data set. The best fit parameters of the Reactor Antineutrino Anomaly (star) is disfavored at  $2.2\sigma$  confidence level. [1]

## 6.6 Measured Antineutrino Spectrum

Selection criteria for IBD events used in the measurement the antineutrino spectrum were the same as those used in the oscillation analysis, with the exception of the shower veto. The veto window around a cosmic muon cluster was increased to (0,200)  $\mu\text{s}$ , and around a fast neutron to (-250,+250)  $\mu\text{s}$ . The analysis method for determining the prompt spectrum was also the same used for the oscillation analysis, a subtraction of accidental events from correlated events in both reactor on and off data sets. An atmospheric correction factor of  $k_p = 0.991 \pm 0.004$  was applied. The resulting prompt energy spectrum of IBD events can be seen in Figure 6.16.

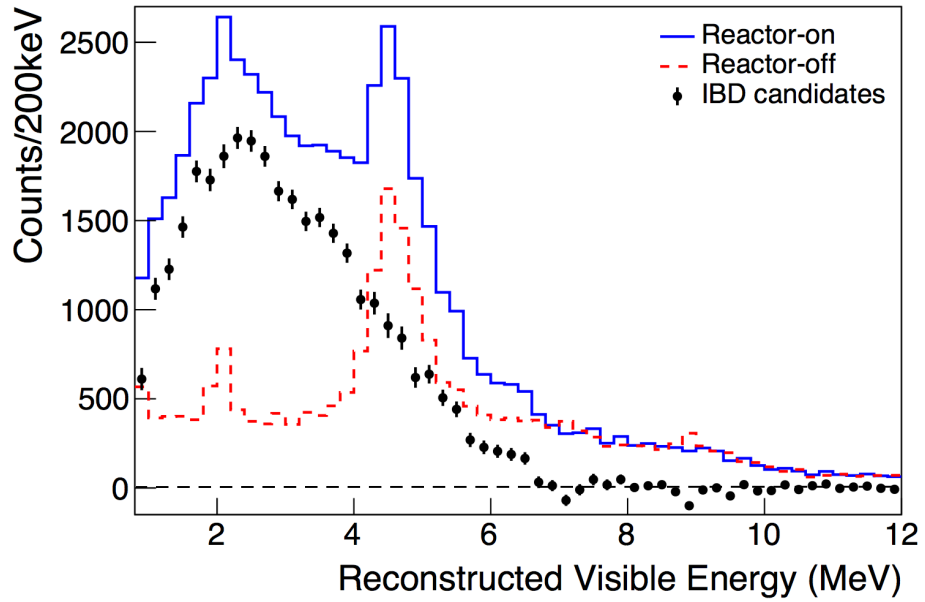


**Figure 6.16:** Reconstructed visible prompt energy of IBD events (black), along with correlated IBD candidates in reactor on (blue, solid) and reactor off (red, dashed) periods. Errors are statistical. The reactor off spectrum has been scaled by the relative exposure time between on and off. [2]

# **CHAPTER 7**

# **CONCLUSIONS**

# BIBLIOGRAPHY

- [1] J. Ashenfelter et al. First Search for Short-Baseline Neutrino Oscillations at HFIR with PROSPECT. *Phys. Rev. Lett.*, 121:251802, Dec 2018.
- [2] J. Ashenfelter et al. Measurement of the Antineutrino Spectrum from  $^{235}\text{U}$  Fission at HFIR with PROSPECT. *Phys. Rev. Lett.*, 122(25):251801, 2019.
- [3] L. Meitner O. von Baeyer, O. Hahn. Über die  $\beta$ -Strahlen des aktiven Niederschlags des Thoriums. *Zeitschrift fur Physik*, 12:273–279, 1911.
- [4] J. Chadwick. The intensity distribution in the magnetic spectrum of beta particles from radium (B + C). *Verh. Phys. Gesell.*, 16:383–391, 1914.
- [5] C. D. Ellis and W. A. Wooster. The average energy of disintegration of radium E. *Proceedings of the Royal Society of London Series A*, 117:109–123, 1927.
- [6] E. Fermi. An attempt of a theory of beta radiation. 1. *Z. Phys.*, 88:161–177, 1934.
- [7] C. L. Cowan, F. Reines, F. B. Harrison, H. W. Kruse, and A. D. McGuire. Detection of the free neutrino: a confirmation. *Science*, 124(3212):103–104, 1956.
- [8] G. Danby, J-M. Gaillard, K. Goulianos, L. M. Lederman, N. Mistry, M. Schwartz, and J. Steinberger. Observation of high-energy neutrino reactions and the existence of two kinds of neutrinos. *Phys. Rev. Lett.*, 9:36–44, Jul 1962.
- [9] K. Kodama et al. Observation of tau neutrino interactions. *Phys. Lett.*, B504:218–224, 2001.
- [10] K. Kodama et al. Final tau-neutrino results from the donut experiment. *Phys. Rev. D*, 78:052002, Sep 2008.

- [11] M. Goldhaber, L. Grodzins, and A. W. Sunyar. Helicity of neutrinos. *Phys. Rev.*, 109:1015–1017, Feb 1958.
- [12] M. Tanabashi et al. Review of particle physics. *Phys. Rev. D*, 98:030001, Aug 2018.
- [13] Aldo Serenelli. Alive and well: a short review about standard solar models. *Eur. Phys. J.*, A52(4):78, 2016.
- [14] IAEA. Live Chart of Nuclides, 2013.
- [15] Raymond Davis, Don S. Harmer, and Kenneth C. Hoffman. Search for neutrinos from the sun. *Phys. Rev. Lett.*, 20:1205–1209, May 1968.
- [16] B. Pontecorvo. Neutrino Experiments and the Problem of Conservation of Leptonic Charge. *Sov. Phys. JETP*, 26:984–988, 1968. [Zh. Eksp. Teor. Fiz.53,1717(1967)].
- [17] S M Bilen’ki and Bruno Pontecorvo. Lepton mixing and neutrino oscillations. *Soviet Physics Uspekhi*, 20(10):776, 1977.
- [18] J. N. Abdurashitov et al. Results from SAGE. *Phys. Lett.*, B328:234–248, 1994.
- [19] W. Hampel et al. GALLEX solar neutrino observations: Results for GALLEX IV. *Phys. Lett.*, B447:127–133, 1999.
- [20] M. Altmann et al. GNO solar neutrino observations: Results for GNO I. *Phys. Lett.*, B490:16–26, 2000.
- [21] E. Bellotti. First results from GNO. *Nucl. Phys. Proc. Suppl.*, 91:44–49, 2001. [,44(2001)].
- [22] Y. Fukuda et al. Evidence for oscillation of atmospheric neutrinos. *Phys. Rev. Lett.*, 81:1562–1567, Aug 1998.
- [23] Q. R. Ahmad et al. Measurement of the rate of  $\nu_e + d \rightarrow p + p + e^-$  interactions produced by  $^8b$  solar neutrinos at the sudbury neutrino observatory. *Phys. Rev. Lett.*, 87:071301, Jul 2001.

- [24] Q. R. Ahmad et al. Direct evidence for neutrino flavor transformation from neutral-current interactions in the sudbury neutrino observatory. *Phys. Rev. Lett.*, 89:011301, Jun 2002.
- [25] John N. Bahcall, M. H. Pinsonneault, and Sarbani Basu. Solar models: Current epoch and time dependences, neutrinos, and helioseismological properties. *Astrophys. J.*, 555:990–1012, 2001.
- [26] Raymond Davis. Nobel lecture: A half-century with solar neutrinos. *Rev. Mod. Phys.*, 75:985–994, Aug 2003.
- [27] A. Aguilar-Arevalo et al. Evidence for neutrino oscillations from the observation of anti-neutrino(electron) appearance in a anti-neutrino(muon) beam. *Phys. Rev.*, D64:112007, 2001.
- [28] A. A. Aguilar-Arevalo et al. Unexplained Excess of Electron-Like Events From a 1-GeV Neutrino Beam. *Phys. Rev. Lett.*, 102:101802, 2009.
- [29] A. A. Aguilar-Arevalo et al. Event Excess in the MiniBooNE Search for  $\bar{\nu}_\mu \rightarrow \bar{\nu}_e$  Oscillations. *Phys. Rev. Lett.*, 105:181801, 2010.
- [30] A. A. Aguilar-Arevalo et al. Improved search for  $\bar{\nu}_\mu \rightarrow \bar{\nu}_e$  oscillations in the miniboone experiment. *Phys. Rev. Lett.*, 110:161801, Apr 2013.
- [31] W Hampel et al. Final results of the 51cr neutrino source experiments in gallex. *Physics Letters B*, 420(1):114 – 126, 1998.
- [32] F. Kaether, W. Hampel, G. Heusser, J. Kiko, and T. Kirsten. Reanalysis of the gallex solar neutrino flux and source experiments. *Physics Letters B*, 685(1):47 – 54, 2010.
- [33] J. N. Abdurashitov et al. Measurement of the response of a gallium metal solar neutrino experiment to neutrinos from a  $^{51}\text{Cr}$  source. *Phys. Rev. C*, 59:2246–2263, Apr 1999.
- [34] J. N. Abdurashitov, V. N. Gavrin, S. V. Girin, V. V. Gorbachev, P. P. Gurkina, T. V. Ibragimova, A. V. Kalikhov, N. G. Khairnasov, T. V. Knodel, V. A. Matveev, I. N. Mirmov, A. A. Shikhin, E. P. Veretenkin, V. M. Vermul, V. E.

- Yants, G. T. Zatsepин, T. J. Bowles, S. R. Elliott, W. A. Teasdale, B. T. Cleveland, W. C. Haxton, J. F. Wilkerson, J. S. Nico, A. Suzuki, K. Lande, Yu. S. Khomyakov, V. M. Poplavsky, V. V. Popov, O. V. Mishin, A. N. Petrov, B. A. Vasiliev, S. A. Voronov, A. I. Karpenko, V. V. Maltsev, N. N. Oshkanov, A. M. Tuchkov, V. I. Barsanov, A. A. Janelidze, A. V. Korenkova, N. A. Kotelnikov, S. Yu. Markov, V. V. Selin, Z. N. Shakirov, A. A. Zamyatina, and S. B. Zlokazov. Measurement of the response of a ga solar neutrino experiment to neutrinos from a  $^{37}\text{Ar}$  source. *Phys. Rev. C*, 73:045805, Apr 2006.
- [35] J. N. Abdurashitov, V. N. Gavrin, V. V. Gorbachev, P. P. Gurkina, T. V. Ibragimova, A. V. Kalikhov, N. G. Khairnasov, T. V. Knodel, I. N. Mirmov, A. A. Shikhin, E. P. Veretenkin, V. E. Yants, G. T. Zatsepин, T. J. Bowles, S. R. Elliott, W. A. Teasdale, J. S. Nico, B. T. Cleveland, and J. F. Wilkerson. Measurement of the solar neutrino capture rate with gallium metal. iii. results for the 2002–2007 data-taking period. *Phys. Rev. C*, 80:015807, Jul 2009.
- [36] Carlo Giunti and Marco Laveder. Statistical significance of the gallium anomaly. *Phys. Rev. C*, 83:065504, Jun 2011.
- [37] Carlo Giunti and Marco Laveder. Short-baseline electron neutrino disappearance, tritium beta decay, and neutrinoless double-beta decay. *Phys. Rev. D*, 82:053005, Sep 2010.
- [38] K. N. Abazajian et al. Light Sterile Neutrinos: A White Paper. 2012.
- [39] A. C. Hayes and Petr Vogel. Reactor Neutrino Spectra. *Ann. Rev. Nucl. Part. Sci.*, 66:219–244, 2016.
- [40] NNDC. Chart of Nuclides.
- [41] International Atomic Energy Agency. Evaluated Nuclear Data File. Evaluated Nuclear Data File.
- [42] Nuclear Energy Agency.
- [43] F. Von Feilitzsch, A. A. Hahn, and K. Schreckenbach. EXPERIMENTAL BETA SPECTRA FROM PU-239 AND U-235 THERMAL NEUTRON FISSION PRODUCTS AND THEIR CORRELATED ANTI-NEUTRINOS SPECTRA. *Phys. Lett.*, 118B:162–166, 1982.

- [44] K. Schreckenbach, G. Colvin, W. Gelletly, and F. Von Feilitzsch. DETERMINATION OF THE ANTI-NEUTRINO SPECTRUM FROM U-235 THERMAL NEUTRON FISSION PRODUCTS UP TO 9.5-MEV. *Phys. Lett.*, 160B:325–330, 1985.
- [45] A. A. Hahn, K. Schreckenbach, G. Colvin, B. Krusche, W. Gelletly, and F. Von Feilitzsch. Anti-neutrino Spectra From  $^{241}\text{Pu}$  and  $^{239}\text{Pu}$  Thermal Neutron Fission Products. *Phys. Lett.*, B218:365–368, 1989.
- [46] N. Haag, A. Gtlein, M. Hofmann, L. Oberauer, W. Potzel, K. Schreckenbach, and F. M. Wagner. Experimental Determination of the Antineutrino Spectrum of the Fission Products of  $^{238}\text{U}$ . *Phys. Rev. Lett.*, 112(12):122501, 2014.
- [47] P. Vogel, G. K. Schenter, F. M. Mann, and R. E. Schenter. Reactor antineutrino spectra and their application to antineutrino-induced reactions. ii. *Phys. Rev. C*, 24:1543–1553, Oct 1981.
- [48] Th. A. Mueller et al. Improved Predictions of Reactor Antineutrino Spectra. *Phys. Rev.*, C83:054615, 2011.
- [49] Patrick Huber. On the determination of anti-neutrino spectra from nuclear reactors. *Phys. Rev.*, C84:024617, 2011. [Erratum: Phys. Rev.C85,029901(2012)].
- [50] Xin Qian and Jen-Chieh Peng. Physics with Reactor Neutrinos. *Rept. Prog. Phys.*, 82(3):036201, 2019.
- [51] P. Vogel and John F. Beacom. Angular distribution of neutron inverse beta decay, anti-neutrino( $e^-$ ) +  $p \rightarrow e^+ + n$ . *Phys. Rev.*, D60:053003, 1999.
- [52] M. Apollonio et al. Limits on neutrino oscillations from the CHOOZ experiment. *Phys. Lett.*, B466:415–430, 1999.
- [53] M. Apollonio et al. Search for neutrino oscillations on a long baseline at the CHOOZ nuclear power station. *Eur. Phys. J.*, C27:331–374, 2003.
- [54] F. Boehm et al. Final results from the Palo Verde neutrino oscillation experiment. *Phys. Rev.*, D64:112001, 2001.
- [55] K. Eguchi et al. First results from KamLAND: Evidence for reactor anti-neutrino disappearance. *Phys. Rev. Lett.*, 90:021802, 2003.

- [56] T. Araki et al. Measurement of neutrino oscillation with KamLAND: Evidence of spectral distortion. *Phys. Rev. Lett.*, 94:081801, 2005.
- [57] F. P. An et al. The Detector System of The Daya Bay Reactor Neutrino Experiment. *Nucl. Instrum. Meth.*, A811:133–161, 2016.
- [58] Feng Peng An et al. Measurement of the Reactor Antineutrino Flux and Spectrum at Daya Bay. *Phys. Rev. Lett.*, 116(6):061801, 2016. [Erratum: Phys. Rev. Lett.118,no.9,099902(2017)].
- [59] D. Adey et al. Improved Measurement of the Reactor Antineutrino Flux at Daya Bay. 2018. arXiv:1808.10836 [hep-ex].
- [60] A. A. Aguilar-Arevalo et al. Improved Search for  $\bar{\nu}_\mu \rightarrow \bar{\nu}_e$  Oscillations in the MiniBooNE Experiment. *Phys. Rev. Lett.*, 110:161801, 2013.
- [61] Carlo Giunti and Marco Laveder. Statistical Significance of the Gallium Anomaly. *Phys. Rev.*, C83:065504, 2011.
- [62] G. Mention, M. Fechner, Th. Lasserre, Th. A. Mueller, D. Lhuillier, M. Cribier, and A. Letourneau. The Reactor Antineutrino Anomaly. *Phys. Rev.*, D83:073006, 2011.
- [63] S. H. Seo et al. Spectral Measurement of the Electron Antineutrino Oscillation Amplitude and Frequency using 500 Live Days of RENO Data. *Phys. Rev.*, D98(1):012002, 2018.
- [64] H. De Kerret et al. First Double Chooz  $\theta_{13}$  Measurement via Total Neutron Capture Detection. 2019. arXiv:1901.09445 [hep-ex].
- [65] F. P. An et al. Evolution of the Reactor Antineutrino Flux and Spectrum at Daya Bay. *Phys. Rev. Lett.*, 118(25):251801, 2017.
- [66] G. Bak, J. H. Choi, H. I. Jang, J. S. Jang, S. H. Jeon, K. K. Joo, K. Ju, D. E. Jung, J. G. Kim, J. H. Kim, J. Y. Kim, S. B. Kim, S. Y. Kim, W. Kim, E. Kwon, D. H. Lee, H. G. Lee, Y. C. Lee, I. T. Lim, D. H. Moon, M. Y. Pac, Y. S. Park, C. Rott, H. Seo, J. W. Seo, S. H. Seo, C. D. Shin, J. Y. Yang, J. Yoo, and I. Yu. Fuel-composition dependent reactor antineutrino yield at reno. *Phys. Rev. Lett.*, 122:232501, Jun 2019.

- [67] J. Ashenfelter et al. The PROSPECT Reactor Antineutrino Experiment. *Nucl. Instrum. Meth.*, A922:287–309, 2019.
- [68] Germina Ilas, David Chandler, Brian Ade, Eva Sunny, Ben Betzler, and Dan Pinkston. Modeling and simulations for the high flux isotope reactor cycle 400. Technical report, Oak Ridge National Laboratory, 3 2015. <https://info.ornl.gov/sites/publications/Files/Pub54181.pdf>.
- [69] J. Ashenfelter et al. Background Radiation Measurements at High Power Research Reactors. *Nucl. Instrum. Meth.*, A806:401–419, 2016.
- [70] Blaine Alexander Heffron. Characterization of Reactor Background Radiation at HFIR for the PROSPECT Experiment. [https://trace.tennessee.edu/utk\\_gradthes/4747/](https://trace.tennessee.edu/utk_gradthes/4747/).
- [71] Brennan Hackett. DANG and the Background Characterisation of HFIR for PROSPECT. [https://prospect.yale.edu/sites/default/files/hackett\\_brennan\\_-university\\_of\\_surrey.pdf](https://prospect.yale.edu/sites/default/files/hackett_brennan_-university_of_surrey.pdf).
- [72] J. Ashenfelter et al. A Low Mass Optical Grid for the PROSPECT Reactor Antineutrino Detector. *JINST*, 14(04):P04014, 2019.
- [73] J. Ashenfelter et al. The Radioactive Source Calibration System of the PROSPECT Reactor Antineutrino Detector. *Nucl. Instrum. Meth.*, A944:2019, 2019.
- [74] J. Ashenfelter et al. Lithium-loaded Liquid Scintillator Production for the PROSPECT experiment. *JINST*, 14(03):P03026, 2019.
- [75] M. Mendenhall. PRD Figure 3a: average pulse shapes. PROSPECT DocDB 2773-v1, May 2019.
- [76] M. Mendenhall. PRD Figure 4: pulse analysis. PROSPECT DocDB 2764-v4, May 2019.
- [77] M. Mendenhall. PRD Figure 7: PSD vs Signal. PROSPECT DocDB 2731-v1, May 2019.
- [78] M. Mendenhall. AD1 Calibrations tech note. PROSPECT DocDB 2314-v2, May 2018.

- [79] J.B. BIRKS. Chapter 8 - organic liquid scintillators. In J.B. BIRKS, editor, *The Theory and Practice of Scintillation Counting*, International Series of Monographs in Electronics and Instrumentation, pages 269 – 320. Pergamon, 1964.
- [80] Xianyi Zhang. E Scale Tech Note for PRD Analysis. PROSPECT DocDB 2815-v1, July 2019.
- [81] Pranava Surukuchi. Sensitivity public talks. PROSPECT DocDB 1534-v9, August 2017.
- [82] National Nuclear Data Center. ENSDF Database.
- [83] H. W. Kirby and L. R. Morss. Actinium. In L. R. Morss, N. M. Edelstein, and J. Fuger, editors, *The Chemistry of the Actinide and Transactinide Elements*, chapter 2, pages 18–51. Springer, 2011.
- [84] CAEN. CAEN Digitizer DT5730. <https://www.caen.it/products/dt5730/>.
- [85] CAEN. CAEN WaveDump. <https://www.caen.it/products/caen-wavedump/>.
- [86] D. Jones. Docdb 2800:BiPo Technote for PRD. PROSPECT DocDB 2800-v1,
- [87] Olga Kzylova. IBD-like rate and FN+nLi plots. PROSPECT DocDB 2370-v8,
- [88] Andrew Conant. ANTINEUTRINO SPECTRUM CHARACTERIZATION OF THE HIGH FLUX ISOTOPE REACTOR USING NEUTRONIC SIMULATIONS.
- [89] Pranava Surukuchi. Al28 contribution. PROSPECT DocDB 2338-v2, May 2018.
- [90] Pranava Surukuchi. Non-equilibrium isotope correction. PROSPECT DocDB 2346-v2, May 2018.
- [91] Gary J. Feldman and Robert D. Cousins. Unified approach to the classical statistical analysis of small signals. *Phys. Rev. D*, 57:3873–3889, Apr 1998.
- [92] Pranava Surukuchi. Search for Sterile Neutrino Oscillations with the PROSPECT Experiment.